ABSTRACT

Thermal Boundary Layer Measurements using Planar Laser Induced Fluorescence

Sara T. Seitz, Ph.D.

Mentor: Lesley M. Wright, Ph.D.

An experimental arrangement of toluene-based Planar Laser Induced Fluorescence (PLIF) has been developed and applied to the study of free and impinging jets formed with air. In the toluene-based PLIF experiment, the flow is seeded with toluene particles and is illuminated using a laser light sheet. The high-temperature dependency of the toluene fluorescence signal and the temperature induced redshift of the toluene fluorescence spectrum, nominate it for quantitative thermometry applications. The toluene molecules are excited by absorbing a resonant photon from the laser and as a result fluoresce spontaneously. The fluorescence provides useful information such as the concentration and temperature of toluene particles and their surrounding environment. Two-color thermometry, with a single excitation wavelength (266nm) and camera image detection, is established for quantitative thermal characterization in this study. Simple free jets have been investigated to lead to refined data collection and data reduction. Time averaged, temperature profiles for the turbulent, free jets are obtained for jet Reynolds numbers of 5000, 10000, and 15000. To further validate the experimental technique, the jet temperature was varied from 300 K to 375 K. With the proposed data reduction methods,

the PLIF technique was applied to a single impinging jet to assess both thermal flow field over a surface and convective transport from the surface. The PLIF method was validated against locally averaged Nusselt numbers using a traditional heat transfer calculation. PLIF results prove that PLIF can be applied to turbulent, near wall flows, where traditional methods are not able to non-intrusively measure the temperature gradient.

Thermal Boundary Layer Measurements Using Planar Laser Induced Fluorescence

by

Sara Toudeshki Seitz, B.S., M.S.

A Dissertation

Approved by the Department of Mechanical Engineering

____

Kenneth W. Van Treuren, D.Phil.

Submitted to the Graduate Faculty of
Baylor University in Partial Fulfillment of the
Requirements for the Degree
of

Doctor of Philosophy

Approved by the Dissertation Committee

____

Lesley M. Wright, Ph.D., Chairperson

____

Kenneth W. Van Treuren, D.Phil.

____

Jill Klentzman, Ph.D.

____

Stephen McClain, Ph.D.

____

Larry Lehr, Ph.D.

Accepted by the Graduate School

May 2018

____

J. Larry Lyon, Ph.D., Dean

Page bearing signatures is kept on file in the Graduate School.

TABLE OF CONTENTS

LIST OF FIGURES

LIST OF TABLES

NOMENCLATURE

a	Calibration curve slope
b	Calibration curve intercept
b_T	Transversal length scale
c	Speed of light in vacuum
D	Nozzle diameter
D_0	Diameter of jet at the nozzle exit
E	Laser energy
erf	Error function
f	Focal length
F	Streamfunction similarity profile
$F_i(\lambda)$	Spectral transmission curve
$F_{i-Blue}(\lambda)$	Temperature independent spectral transmission curve
$F_{i-\mathrm{Red}}(\lambda)$	Temperature dependent spectral transmission curve
FQY	Fluorescence quantum yield
h	Heat transfer coefficient
H	Jet-to-target surface spacing
I	Fluorescence intensity
$I_{Back-Blue}$	Temperature independent fluorescence intensity of background images

$I_{Back-\mathrm{Re}d}$	Temperature dependent fluorescence intensity of background images
I_{Blue}	Temperature independent fluorescence intensity of toluene/air images
I_N	Normalized fluorescence intensity of toluene/air images
$\overline{I}_N$	Mean of normalized fluorescence intensity of toluene/air images
$I_{\mathrm{Re}d}$	Temperature dependent fluorescence intensity of toluene/air images
I_{ref}	Florescence intensity at room temperature
k_f	Thermal conductivity of fluid
n_i	Spectral response of optical system
n_{i-Blue}	Temperature independent spectral response of optical system
$n_{i-\mathrm{Re}d}$	Temperature dependent spectral response of optical system
Nu	Nusselt number
$\overline{Nu}$	averaged Nusselt number
Nu_{PLIF}	Nusselt number calculated based on PLIF data
$Nu_{Traditional}$	Nusselt number calculated based on thermocouple data
P	Pressure
Pr_t	Turbulent Prandtl number
q_{loss}	heat flux loss
q_s	Surface heat flux
q_{net}	Net heat flux

q''	Heat flux
r	Radial coordinate
R	Jet-to-stagnation point distance
Re	Reynolds number
S_a	Standard deviation for the slope
S_b	Standard deviation for the intercept
S_f	Fluorescence signal
S_{f-Blue}	Temperature independent fluorescence signal
S_{f-Red}	Temperature dependent fluorescence signal
$S_{I_N I_N}$	Standard deviation interval for normalized intensity
T	Temperature
$\bar{T}$	Time averaged temperature
T_{jet}	Jet temperature
T_{PLIF}	Temperature extracted from PLID data
T_{ref}	Reference (room) temperature
T_s	Surface temperature
T_{TC}	Temperature extracted from thermocouple data
T_{Outlet}	Temperature of jet at nozzle exit
$T(y)$	Vertical temperature distribution
T_0	Central temperature of jet at nozzle exit

T_∞	Mainstream temperature
u	Velocity (in a given distance)
$u(y)$	Vertical velocity distribution
$\bar{u}$	Time averaged velocity in axial direction
$\overline{u_c}$	Time averaged velocity along the stream centerline
u_∞	Mainstream velocity
U_0	Velocity of nozzle fluid
$\bar{v}$	Time averaged velocity in radial direction
x_0	Starting length
x, y, z	Cartesian coordinate
Z	Free jet axial coordinate
α	Thermal diffusivity
γ	Empirical constant
ε_H	Thermal eddy diffusivity
ε_M	Momentum eddy diffusivity
η	Dimensionless impinging jet temperature
$\eta(x,r)$	Similarity variable
η_{tol}	Tracer number density
θ	Dimensionless free jet temperature
λ	Wavelength of excitation laser

μ	Dynamic viscosity
ν	Kinematic viscosity
ρ	Density
σ	Absorption cross section (Equation 2.1)
σ	Empirical constant (Equation 5.17)
σ_X	Standard deviation
ϕ	Fluorescence quantum yield
$\overline{\psi}$	Streamfunction

ACKNOWLEDGMENTS

It is with great pleasure that I have the opportunity to express my gratitude towards those whom have helped me along my journey towards a Ph.D. First, to my husband, Abraham Seitz, who has provided me with the moral and emotional support I needed throughout my studies. This work would not have been possible without the unwavering support from him.

I would like to express my sincere gratitude to my Ph.D. advisor, Dr. Lesley Wright, for her continuous support, patience, and immense knowledge. Her guidance helped me during the time of research and writing of this dissertation. I could not have imagined having a better mentor for my Ph.D. study. Beside my advisor, I would like to thank the rest of my dissertation committee: Dr. Jill Klentzman, Dr. Kenneth Van Treuren, Dr. Stephen T. McClain, and Dr. Larry Lehr for taking the time to read, assess, and improve this work.

My sincere thanks also goes to Dr. Carolyn Skurla and Dr. Douglas Smith for their support, encouragement, and guidance. I also thank Mr. Ashley Orr for his help with the construction, and sometimes, deconstruction of my setup as we developed a novel method. Without his precious support, it would not have been possible to conduct this research.

I thank my fellow labmates: Travis Watson, Kyle Vinton, Austin Reed, and Berkley Bonjonia, for stimulating discussion, for the sleepless nights we were working together before making deadlines, and all the fun we had in the last three years. It was great sharing the laboratory with all of you.

I particularly want to thank Mr. Bruno Aguilar, my manager at Honeywell, for being incredibly supportive and flexible on my current work schedule to allow for completion of my Ph.D. Also, I would like to thank my colleagues, Dr. Alexander MirzaMoghadam, Luis Tapia, and Mary Christaner, for all their support and encouragement throughout writing this dissertation.

Last, but not the least, I would like to thank my parents for supporting me spiritually throughout my academic career and my life in general.

DEDICATION

To my God, who provided me with the will power to continue and never give up, and constantly reminding me that He has not given me anything I cannot overcome.

To my husband, Abraham for his support, encouragement, patience, and understanding throughout this process.

To my daughter, Zavonah for serving as my inspiration to continue my studies and reminding me to not take things so seriously.

To my Dogs, Zeppelin, Zoey, Orion, and Lamington Who were no help in writing, but provided much needed stress relief.

CHAPTER ONE

Introduction

Turbulence

In recent years, turbulent flows have attracted many researchers and opened new areas of studies and applications. Turbulent flow is characterized as a type of flow that experiences irregular velocity and pressure changes. Turbulence is observed in life's daily activities; it can occur in natural phenomena such as fast river currents or within advanced engineering systems such as gas turbine engines. Turbulence can be predicted using a dimensionless quantity known as the Reynolds number, which represents a ratio of inertial forces to the viscous forces through the fluid [1]. However, analyzing a turbulent flow is a complicated task due to the complex physics that occur at the fluid-solid interfaces [2]. To design and improve a turbulent system, it is necessary to understand and estimate the flow's key parameters such as velocity and temperature. Over decades, computational fluid dynamics tools have been using models to predict the flow behavior in turbulent systems [3, 4]. The turbulence models and their ability to predict the flow are evaluated using appropriate experimental techniques [5]. The scope of this dissertation is to develop a novel experimental method to non-intrusively characterize the fluid's thermal field. In this chapter, a turbulent system (cooled turbine airfoil) requiring aggressive, convective heat transfer is briefly introduced. This discussion of gas turbine cooling leads to an explanation of necessary thermal measurement for such turbulent flows.

Cooled Turbine Airfoils

Gas turbines are used for a variety of applications such as power generation and aircraft propulsion. The "turbine" section of the gas turbine engine includes consecutive pairs of rotating and stationary airfoils; these airfoils convert energy contained within the fluid to thrust and power [6]. Modern gas turbine engines are increasing their rotor inlet temperatures to achieve higher power output [7] . Since the development of the jet turbine engine, the inlet temperature of the rotors has risen greatly (Figure1.1) [5]. It is important to keep turbine cooling technology relevant to the technology used to increase the temperature.

The rotor inlet temperature of modern gas turbine engines is much higher than the melting point of metals. The cooling scheme allows the turbine's components to work under thermal conditions above the melting temperature of alloys used for the airfoil construction [8]. The cooling techniques generally used are: internal cooling, external film cooling, or a combination of both internal and external cooling. In each method, relatively cool air is extracted from the gas flow path at the compressor, bypasses the combustion chamber, circulates through the airfoils, and is expelled back into the main gas path at the cooling location [5].

A turbine's airfoils can be internally cooled using jet impingement. An impinging jet is characterized as a relatively cool air stream forced out of a hole or slot that impinges on a hot surface, known as the target surface [9]. In cooling technology, impinging jets have a distinct advantage over other cooling techniques due to their aggressive heat and mass transfer features [10]. Jet impingement involves the use of one or more individual jets blowing onto a designated target surface to increase the efficiency of the cooling.

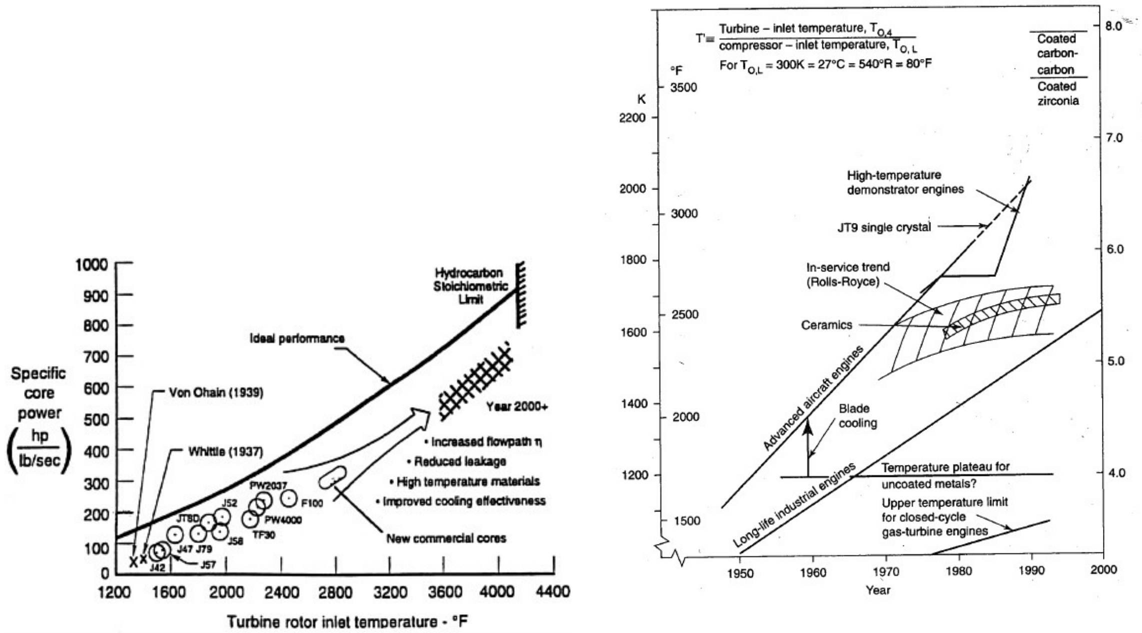

(a) (b)

Figure 1.1: a. The effect of rotor inlet temperature on turbine power output [4], b. Increase of rotor inlet temperature [5]

The use of jet impingement does not come without its own downfalls [11]. When impingement occurs on any surface there is a large pressure drop; therefore, the jet fluid would have much less momentum and energy following impingement. When speaking in respect to gas turbine cooling applications, this drop in pressure can be very detrimental. Sufficient pressure loss must be maintained to prevent ingestion of hot combustion gases into the airfoils to avoid component failure.

Thermal Boundary Layer

To improve the performance of a heat transfer system, it is necessary to fully understand and estimate the flow structure, turbulence, and heat transfer rate within the boundary layer. The bulk of the flow can be divided into two general regions; one region is affected by the fluid viscosity (viscous flow region) and the other region is not affected by the fluid viscosity (inviscid flow region) [12]. Boundary layers, Figure 1.2, are thin layers of the fluid in contact with a surface where the viscosity impacts are significant. Flow can be laminar or turbulent within the boundary layer. Turbulent boundary layers are more complex in comparison with the laminar boundary layers due to the presence of the eddies [13]. The mass, momentum, and energy exchanges are much larger within a turbulent flow than a laminar flow.

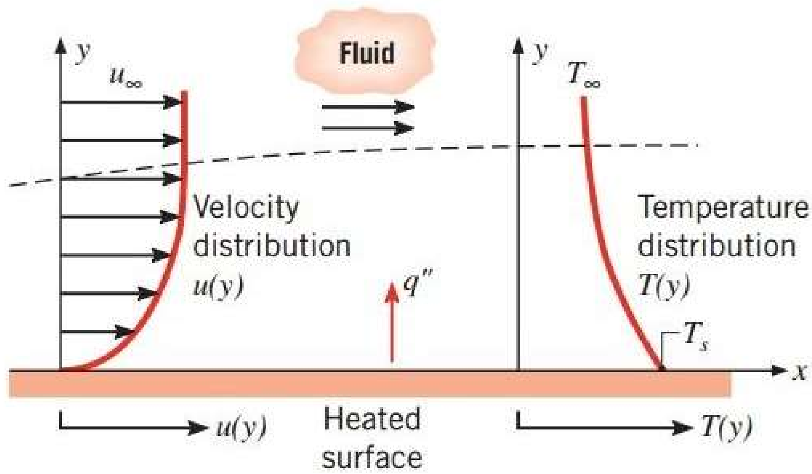

Figure 1.2: Boundary layer [9]

Turbines operate under complicated three-dimensional conditions. As an example, near the hub and tip of a turbine airfoil, there are interactions between the airfoil and endwall boundary layers [14]. These interactions impact the thermal and aerodynamic performance of the turbine. Also, turbulence strongly affects the flow near the airfoil walls due to the presence of the wakes and vortices [11]. Depending on the application and performance, the airfoils and endwalls are cooled using jet impingement or film holes [15]. The cooling schemes add even more complexity to the system. For instance, the flow leaving the cooling holes diffuses into the airfoil boundary layer and disturbs the flow structure.

Estimating the temperature, and its gradient, for cooled airfoils is a difficult task. The challenge is due to the complex physics of the system such as the nature of the turbulence, rotation (in blades), and cooling schemes [16]. Heat transfer analysts have been using numerical methods to solve the energy equation and calculate the temperature. Numerical techniques and computational tools are capable of predicting details that are difficult to achieve by experimental methods. The accurate prediction of heat transfer in turbulent systems is a vital parameter to improve the system performance. To validate the available numerical models, the predictions are compared to experimental data.

Depending on the available experimental equipment and techniques, a variety of information can be obtained for a system. Flow field temperature characterization is more challenging than surface temperature measurements. The difficulty is due to the presence of probes such as thermocouples or hot wires. A thermal measurement probe behaves like an external object and disturbs the flow behavior. Also, this difficulty is more significant within the viscous flow region. Because the boundary layer is very thin, these probes can disturb the near wall flows. Thus, there is a need to develop and apply non-intrusive techniques to characterize the thermal flow field.

Motivations and Objectives of Study

Experimental methods are important for analyzing the heat transfer surfaces and thermal flow fields. Having a better understanding of the temperature distribution within the flow field, and over the surface (through thermal boundary layer), leads to improved system performance. Several experimental methods have been developed to obtain measurements of a surface temperature [17]. Characterizing the boundary layer has always been a challenge. Using a direct method to measure the temperature, such as thermocouples, interrupts the flow structure. Thus, there is a need to develop a non-intrusive method to measure the temperature gradient within the boundary layer.

Surface visualization methods have recently become very popular for surface heat transfer measurements [18, 19]. In addition to surface thermal characterization, it is also crucial to characterize the flow behavior above the surface especially within the thermal boundary layer. Planar Laser Induced Fluorescence (PLIF) could be a solution to this challenge by providing a quantitative relationship between the fluid temperature and fluorescence intensity [20].

PLIF is a two-dimensional, non-intrusive, optical diagnostic method with a potential to measure the flow field parameters such as concentration and temperature. PLIF has been widely used to measure the concentration, particularly in many combustion studies [21, 22]. The purpose of this study is to develop a novel PLIF-based technique and apply it to the study of thermal boundary layer development. Having the capacity to measure the near wall temperature profile provides unparalleled insight into convective heat transfer. This method has the potential to be used in other applications that require the knowledge of fluid temperature gradients. In addition, with the application of this process to highly turbulent flows (as seen in gas turbine cooling applications), the results can also be used to validate state-of-the-art computational fluid dynamics models.

In this dissertation, an experimental arrangement of toluene-based PLIF is developed and applied to measure the temperature gradient within the flow. In order to develop a refined data collection method, a turbulent free jet is initially investigated. Later, the innovative PLIF technique is used to study the turbulent jet impinging at a flat plate. The PLIF technique is validated against regionally averaged heat transfer coefficients measured using a traditional heat transfer experiment. Future study directions are described in three main categories: usage of a higher purity tracer, improvement of diagnostic setup, and new flow field applications such as film cooling.

CHAPTER TWO

PLIF Background and Theory

Laser induced fluorescence (LIF) is an optical diagnostic method used for measuring key flow parameters by counting population densities of atoms in a specific energy state. Planar laser-induced fluorescence (PLIF) is a two dimensional version of LIF, suited for detecting a planar distribution of flow characteristics. A general background behind PLIF and a basic outline of LIF spectroscopy theory, each of which are required to analyze fluorescence signals, are covered in this chapter. In addition, background information on tracer-based LIF and ultraviolet excitation of toluene are discussed.

PLIF History

Laser induced fluorescence (LIF) has made significant contributions towards flow visualization, quantification, particularity, and concentration characterization [23]. Long et al. [24] initially demonstrated planar visualization based on Laser Rayleigh Scattering for concentration measurements within turbulent jets in the late 1970's. A short time later, in 1982, linear and planar imaging using hydroxide-LIF was presented. Kychakoff et al. [25] applied linear LIF for concentration measurement of hydroxide within combustion gases. Additionally, Dyer and Crosley [26] mapped the hydroxide concentration using planar laser induced fluorescence (PLIF). In 1985, PLIF was used for vapor and liquid visualization in fuel spray by Melton and Allen [27]. McDaniel et al. [28] also used PLIF to measure the velocity distribution within a plane of gaseous flow using iodine-PLIF. In the same year, Seitzman [29] proposed nitrogen oxide-PLIF for quantitative temperature visualization in combustion flows.

Technical improvements in optical systems such as cameras, filters, and lenses have assisted in allowing PLIF diagnostics for other parameters, particularly, temperature measurements. In 1999, Thurber [30] studied the fluorescence dependency of acetone aimed to make PLIF more applicable for quantitative temperature measurements. Shortly after that Hanson et al. [30, 31] demonstrated temperature imaging using acetone-PLIF. The imaging of temperatures was derived from single and dual wavelength excitation techniques. In a single wavelength excitation, the flow is excited at a particular wavelength, and the fluorescence intensities are collected within the full spectrum. The collected intensities carry information regarding: temperature, concentration, pressure, and laser energy. For an isobaric experiment with uniform concentration and laser energy, at a particular excitation wavelength, the collected fluorescence intensity can be related to the fluid temperature [31].

Flow pressure and laser energy are two factors that can be controlled during an experiment. It is almost impossible to keep the concentration uniform. To overcome this challenge, Thurber et al. [30, 32, 33] introduced the dual wavelength excitation strategy to remove the concentration dependency of the fluorescence. Ratioing of fluorescence intensities resulting from exciting the tracer at two different wavelengths cancels the concentration impacts. For the wavelength excitation method, intensities are collected at two different wavelengths, simultaneously. This strategy solves the concentration dependency issue. However, providing two different wavelengths would bring more complexity to the experiment.

Kakuho et al. [34] measured the temperature distribution using two types of tracers, 3-pentanone and triethylamine, at a single excitation wavelength. Two tracers fluoresce within two independent spectrum ranges. Fluorescence intensities corresponding to each tracer carry particular information about temperature and concentration dependency of the tracers. Although this method removes the effect of concentration dependency, using two tracers would add some difficulties into the diagnostics. Koban [35] took advantage of the toluene spectroscopic properties and alleviated the challenges related to the concentration dependency effects for temperature applications. Toluene fluorescence consists of two spectrum ranges: temperature dependent and temperature independent. Toluene exhibits a red shift spectrum (Figure 2.1) by increasing the temperature [35]. Particular optical lenses are used to filter the toluene fluorescence and separate each of the mentioned spectra. The fluorescence intensities of both spectra are a function of concentration, but only the red shift spectrum carries information about temperature. Ratioing these spectrum results in removing the effect of concentration.

Energy Transfer in LIF Techniques

A simplified LIF model is discussed here to give an introduction to the LIF concepts, as well as the quantum energy transfer process involved. In the initial stage, photons from a light source, typically a laser, are absorbed by a tracer and then excited to a higher energy state. A laser provides the resonant photons needed for LIF diagnostics. Excited tracer molecules in higher energy states will return to their original state after the excitement. The excited molecules are brought back to their "ground state" to reach equilibrium. While returning to their original state, their extra energy is released as photons known as fluorescence [36]. Figure 2.2 represents a simplified energy transfer procedure in a laser-induced fluorescence experiment.

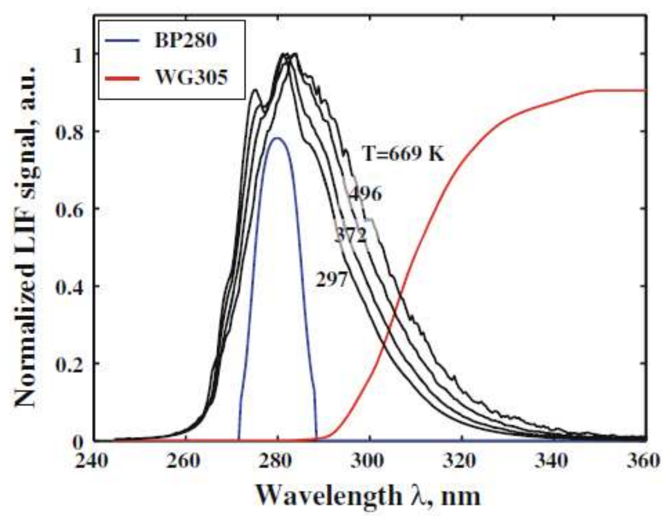

Figure 2.1: Red shift of the toluene emission spectrum with increasing temperature [35]

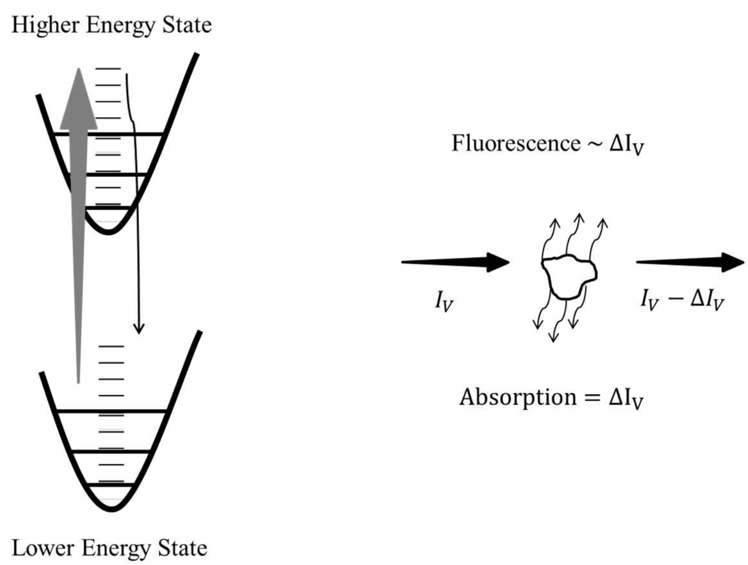

Figure 2.2: LIF light scattering [36]

LIF Equation

The fluorescence signal can be related to specific tracer characteristics such as concentration and temperature [37]. The fluorescence signal S_f (in units of photons) was developed by Thurber [30] as seen in Equation 2.1:

$$S_f = \frac{E}{hc/\lambda} \eta_{tol} \sigma(T) \int F_i(\lambda) \phi(\lambda, T) n_i(\lambda) d\lambda \tag{2.1}$$

Absorption cross section (σ) and fluorescence quantum yield or FQY (ϕ) are two photo-physical features for LIF measurements that describe the probability of a molecule absorbing and emitting photons, respectively [38]. These two parameters are functions of temperature, pressure, and wavelength [39]. These two features play important roles within selecting an appropriate tracer for a PLIF experiment. At a given excitation wavelength and isobaric condition, the fluorescence signal is expressed as Equation 2.2. Hence, the fluorescence signal is only a function of temperature, concentration, and optical system response.

$$S_f \propto \sigma(T) \int F_i(\lambda) \phi(\lambda, T) n_i(\lambda) d\lambda \tag{2.2}$$

PLIF Tracer Selection

Selecting a proper tracer is an important factor when using a LIF technique. Several tracers have been used based on flowfield features and applications [22]. Examples include OH [25], NO [29], acetone [36], 3-pentanone [40], and toluene [35]. Each tracer has to retain the following specifications to be applied in a LIF diagnostic. The tracer has to possess a vigorous non-resonant fluorescence spectrum within a UV excitation wavelength. The absorption spectrum needs to be accessible using a high power light source. Also, it is preferable that the tracer has a high vapor pressure at room temperature to make the seeding process more convenient [38]. Three tracers which meet the needed requirements are listed in Table 2.1. In this table, excitation wavelength range and its resultant emission wavelength, and temperature dependency corresponding to the wavelength range are provided for each tracer. For example, for a 340 nm excitation wavelength, acetone fluorescence intensity decreases 7% with a 100 K increase in temperature. For different applications, additional tracer demands may be required.

Table 2.1: Comparison of candidate tracers for LIF detection in gaseous fluids [41]

Tracer	Boiling Point (K)	Emission Range (nm)	Temperature Dependency (% / 100 K)	
			220 (nm)	340 (nm)
Acetone	329.65	300-550	-25	-7
3-Pentanone	374.65	300-550	-28	-11
Toluene	383.75	270-370	-30	80

Acetone has been used in a variety of applications from flow visualization to concentration measurements within gaseous flows near room temperature and atmospheric pressure [42, 42]. 3-pentanone has been mostly used in combustion systems, especially for fuel mixing applications [43]. Toluene has been recently applied in a variety of fields such as: thermal stratification, concentration measurement, and flow visualization [39]. Due to its spectroscopic and fluorescence characteristics, toluene separates itself as an ideal tracer for quantitative temperature measurement applications [24]. Table 2.1 shows that toluene has the best temperature sensitivity in comparison with the other tracers (80% increase in fluorescence intensity with 100K increase in temperature).

It is important to note that a specific excitation approach is required for each tracer because the excitation wavelength influences the fluorescence emission. There are three standard laser excitation choices: 248nm, 266nm, and 308nm. The corresponding fluorescence features, FQY and absorption cross section, for the three mentioned tracers are listed in Table 2.2. Toluene has higher FQY and absorption cross section in comparison with the other two listed tracers. Therefore, toluene is chosen in this study as the tracer for quantitative temperature field measurements.

Table 2.2. Absolute FQY and absorption cross section values of candidate tracers at different excitation wavelengths [44-46]

Tracer	FQY			Absorption Cross Section $10^{-20}\,cm^2$ / molecule		
	248 (nm)	266 (nm)	308 (nm)	248 (nm)	266 (nm)	308 (nm)
Acetone	0.00034	0.00052	0.00082	2	4.3	1.6
3-Pentanone	0.00083	0.00101	0.00107	1.8	4.5	2
Toluene	0.056	0.19	N / A	31	19	N / A

Two-Color Thermometry Method

As described earlier in this chapter, the fluorescence signal is a function of pressure, temperature, and tracer concentration. It is impossible to keep the tracer concentration constant through the entire fluid domain. As a result, the toluene fluorescence intensity depends on both temperature and tracer concentration. Therefore, a need exists to control the tracer concentration impacts and remove the effect of its concentration for thermometry measurements.

A valuable spectroscopic property of toluene, strong temperature dependency of its fluorescence signal, nominates this tracer for a quantitative thermometry. Toluene fluorescence shows a red shift by increasing the temperature. As shown in Figure 2.1 [35], there are two general regions for wavelength; regions where the spectra peak shows a shift by increasing the temperature and regions where no shift is observed by increasing the temperature. In the other words, near the wavelength of 280nm, the fluorescence spectra are insensitive to temperature (blue spectra) and at wavelengths greater than 305nm, the fluorescence spectra are sensitive to temperature (red spectra).

In order to cancel the effect of concentration, fluorescence intensities at two regions (temperature sensitive and insensitive regions) must to be collected. The ratio of the intensities from these two bands cancels the effect of concentration. Thus, the fluorescence intensity ratio is only a function of temperature. For this purpose, two optical filters are required to pass separate fluorescence wavelengths. The fluorescence signal passing through each filter S_{f-Red} and S_{f-Blue} can be expressed using Equation 2.1. The ratio of these two intensities, Equation 2.3, is only a function of temperature and optical system response. The optical system response comes from variation of the image's brightness and camera uniformity. In order to remove this effect from the integral, the intensity ratios are normalized by the intensity ratio at a known temperature (Equation 2.4).

$$\frac{S_{f-\mathrm{Red}}}{S_{f-Blue}} = \frac{\int F_{i-\mathrm{Red}}(\lambda)\phi(\lambda,T)\,n_{i-\mathrm{Red}}(\lambda)\,d\lambda}{\int F_{i-Blue}(\lambda)\phi(\lambda,T)\,n_{i-Blue}(\lambda)\,d\lambda} \tag{2.3}$$

$$\frac{S_{f-\mathrm{Red}}(T)/S_{f-\mathrm{Red}}(298)}{S_{f-Blue}(T)/S_{f-Blue}(298)}=\frac{\int F_{i-\mathrm{Red}}(\lambda)\phi(\lambda,T)\,d\lambda \Big/ \int F_{i-\mathrm{Red}}(\lambda)\phi(\lambda,298)\,d\lambda}{\int F_{i-Blue}(\lambda)\phi(\lambda,T)\,d\lambda \Big/ \int F_{i-Blue}(\lambda)\phi(\lambda,298)\,d\lambda} \tag{2.4}$$

PLIF, as an optical diagnostic technique, highly relies on the spectroscopy properties of the tracer. The tracer selection plays a crucial role in PLIF experiments. The purpose of this investigation is to develop a non-intrusive method to study the flow field temperature. Therefore, the fluoresce intensity must have a great sensitivity to the flow temperature gradient. Spectroscopic properties of toluene make it a great candidate for this study.

CHAPTER THREE

Experimentation Facility and Procedure

In PLIF imaging, flow is seeded with a fluorescing material known as a tracer (toluene for this investigation). A laser beam spreads into a laser sheet (using optics) and excites a two dimensional region of the flow. The laser wavelength is proportional to the resonant transition of the tracer. Molecules within this region move to a higher energy level resulting from absorption of the laser's energy. The excited molecules then return to an equilibrium level of energy by fluorescing (emitting energy at a longer wavelength). The intensities corresponding to the fluorescence are collected using optical detectors such as CCD cameras and lenses. Two color thermometry, single excitation wavelength (266nm), and single camera image detection are established for quantitative temperature measurements. Development of an experimental arrangement of toluene-based PLIF and the data collection procedure are presented in this chapter.

Facility Overview

All experimentation done for this dissertation was performed in the Convective Heat Transfer Laboratory (CHTL) at Baylor University. The flow line is made of aluminum tubing with a round cross section, 0.0254 m in diameter. An inline heater from Farnam Custom Product is used to generate high temperature flow conditions required for the PLIF method development. The entire line is wrapped in fiberglass insulation to reduce heat loss from the test section. Standard T-type thermocouples are placed at desirable locations to monitor the flow temperature. The thermocouple output is monitored and recorded using

LabVIEW software from National Instruments. The output temperatures are recorded every second and written to a data file.

A laser system was used as a primary excitation source for PLIF diagnostics. The detection system consists of a CCD camera, optical lenses, and data collection computer. The experimental setup was designed and built for the purpose of PLIF diagnostic development and validation at Baylor University. Figure 3.1 shows the schematic of the general PLIF setup used for this study.

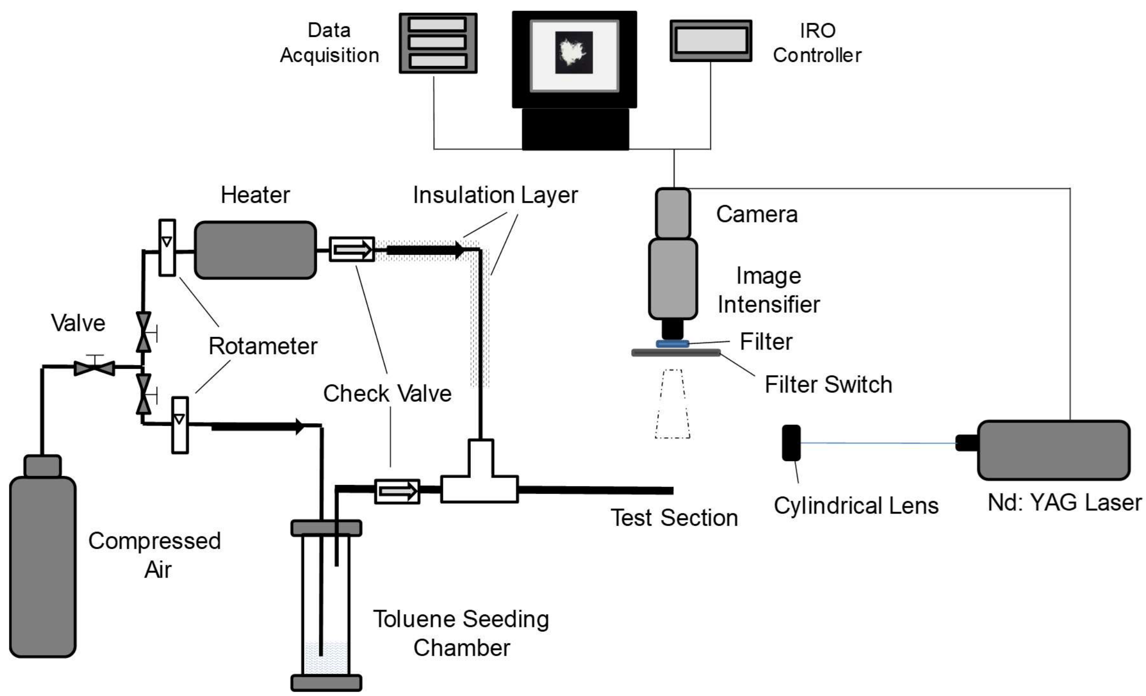

Figure 3.1: Sketch of the general PLIF setup

Laser System

The laser is one of the crucial components for the PLIF method. A Neodymium-doped Yttrium Aluminum Garnet (Nd:YAG) laser from Litron Laser is used for this study. The excitation wavelength selected for this study, due to the fluorescence features of toluene, is 266 nm, and this wavelength is producible using a Nd:YAG laser. This laser produces highly directional and coherent photons that are used to selectively characterize the flow. A laser beam is spread into a thin plane using a cylindrical lens with f = -20 mm. In order to create an instantaneous visualization, a pulse width about 100ns is used for the laser. The laser energy output is in the range of 40 to120 mJ / cm^2 .

Optical Detection System

The fluorescence signals are collected by an optical system that consists of an intensified CCD camera, equipped with an Intensify Relay Optics (IRO) from LaVision. The camera has a 172 × 260 pixel CCD array with 6.45μm pixel size and it is 4 × 4 hardware binned. The camera exposure time is set at 6000μs. The combination of a CCD camera and IRO increases the sensitivity of the system to measure the ultraviolet fluorescence signal range [41]. The optical system is equipped with an IRO controller which allows for the adjustment of the timing of the camera and laser. The camera is gated for 100ns, and the corresponding delay for the laser pulse to occur inside the gate of the camera is 10,225ns. The optical system is placed at a right angle to the laser sheet.

A UV lens from Nikkor-UV is used to focus the images on the camera. The lens is set at its lowest f-number to achieve the highest photon efficiency. Two filters are used for two different wavelength ranges for the toluene emission spectrum (i.e. tracer 1 and tracer 2 in Figure 3.2). The first wavelength range is temperature independent while the second is temperature dependent. The temperature independent filter (blue detector) and the temperature dependent filter (red detector) passes 285nm and 320nm wavelengths, respectively. It is the ratio of these two signals that gives the temperature information without dependence on tracer concentration.

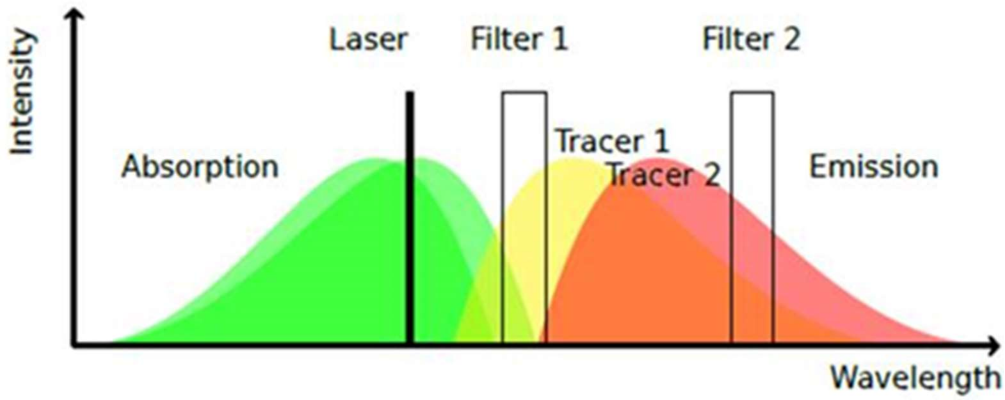

Figure 3.2: Absorption and emission diagram for the tracers and filters [42]

Toluene Seeding System

A toluene seeding system, made out of a 0.0762 m diameter aluminum pipe and sealed with two flanges at each end, disperses the toluene into the flow line. This system works based on the bubbling principle and provides a saturated air and toluene gas mixture. Two rotameters are used to monitor the flow rate of the air through the heater and bubbling system. Air enters the bubbling system through a 0.0127m inlet pipe and provides a saturated air and toluene gas mixture. The mixture leaves the bubbling system through a 0.0127 m outlet pipe and meets the heated air at a T-junction. Two check valves are installed after the outlets of the heater and the bubbling system to avoid a reverse flow

Data Collection Procedure

The PLIF experimental procedure consists of three main image recording steps: background images, reference images, and air/toluene images at different temperatures. For each step two sets of 500-1000 images (depending on the application) are recorded: temperature dependent (using red filter) and temperature independent (using blue filter). Background images are captured while the laser is on and there is only airflow in the system, because it is desired to record the optical noise that is created by the surrounding light. Reference images are taken while the mixture of air and toluene is flowed in the system at room temperature (297 K) and the laser is on. After the system reaches the desirable steady-state condition, the air/toluene images are recorded while the laser in on. Davis 8.3 software from LaVision is used to record the raw images. For each step, flow and ambient temperatures, gauge pressure, and flowrate are monitored and recorded. High resolution images are exported from Davis in the tagged image file (TIF) format then post processed using in-house MATLAB code (Appendix A).

The main components of PLIF experimentation are a laser, optical systems, and a tracer seeder. A general overview of the experimental facility and procedure used in this study was introduced in this chapter. Details about experimental setup and post processing procedures for the calibration and validation tests are provided in the following chapters.

CHAPTER FOUR

PLIF Calibration

PLIF is a non-intrusive method that quantitatively measures the flow field parameters. As previously mentioned, the scope of this investigation is to develop PLIF to study the temperature field within a fluid. The fluorescence intensity of the tracer particles is captured within a PLIF experiment. A calibration must be completed to determine the relation between the fluorescence intensity and the flow temperature.

Calibration Setup

The first step of this study is to develop an empirical relationship between the temperature of the tracer and its florescence intensity. Figure 4.1 shows the schematic of a calibration setup for the PLIF measurement. The general overview of the flow line was described in chapter two. The toluene fluorescence wavelength is within the range of 270 - 370 nm. It requires a specific window to pass the mentioned wavelength range without changing the fluorescence properties. Since this method is highly dependent on the fluorescence intensity, using any glass window to perform the calibration is avoided. The temperature profile is uniform throughout the central region of a steady state jet cross section. Therefore, the calibration experiment is carried out through a cross section of a free jet.

Flow with a Reynolds number of approximately 10,000, based on the inner tube diameter, is used for the calibration. The air supplied from a compressor is divided into two separate streams: 80% of the flow goes to the heater and the rest goes to the seeding system. The flow in each line is controlled by a valve and a rotameter. Standard T-type thermocouples are placed at the inlet and outlet of the heater and within the central region of the jet cross section to record the air temperatures. The thermocouple output is monitored and recorded using LabVIEW software from National Instruments. The output temperatures are recorded every second and written to a data file. The calibration process is performed at a variety of temperatures between room temperature and 400 K with the step size of 25 K. For each measurement, the flow first passes only through the heater to reach the desirable temperature at the central region of the jet cross-section at the exit of the tube. When the system reaches the steady state condition (no changes in temperature), toluene is introduced into the flow line through the seeding system. As was mentioned earlier in chapter three, the seeding system works based on the bubbling principle. A pressure gauge is placed at the inlet of the seeding system to calibrate the flow rate measured with the rotameter. Check valves are placed after the heater and the seeder to avoid any reverse flow. The heated and seeded flow meet at a T-junction. In order to provide a uniform mixture of toluene and air, an insert of twisted aluminum tape is placed in the tube. The flow line is made of aluminum tubing with a round cross section, 0.0254 m in diameter. A 0.0127 m diameter aluminum tube with a length of 0.254 m is used to produce a fully developed flow for calibration purposes. The 0.0127 m diameter tube is connected to the main flow line tubing using a reducer fitting. A 90-degree pipe elbow is used to provide a cross section perpendicular to the optical system. The camera is equipped with a filter switch which can remotely alter the filter that is required for the PLIF experiment.

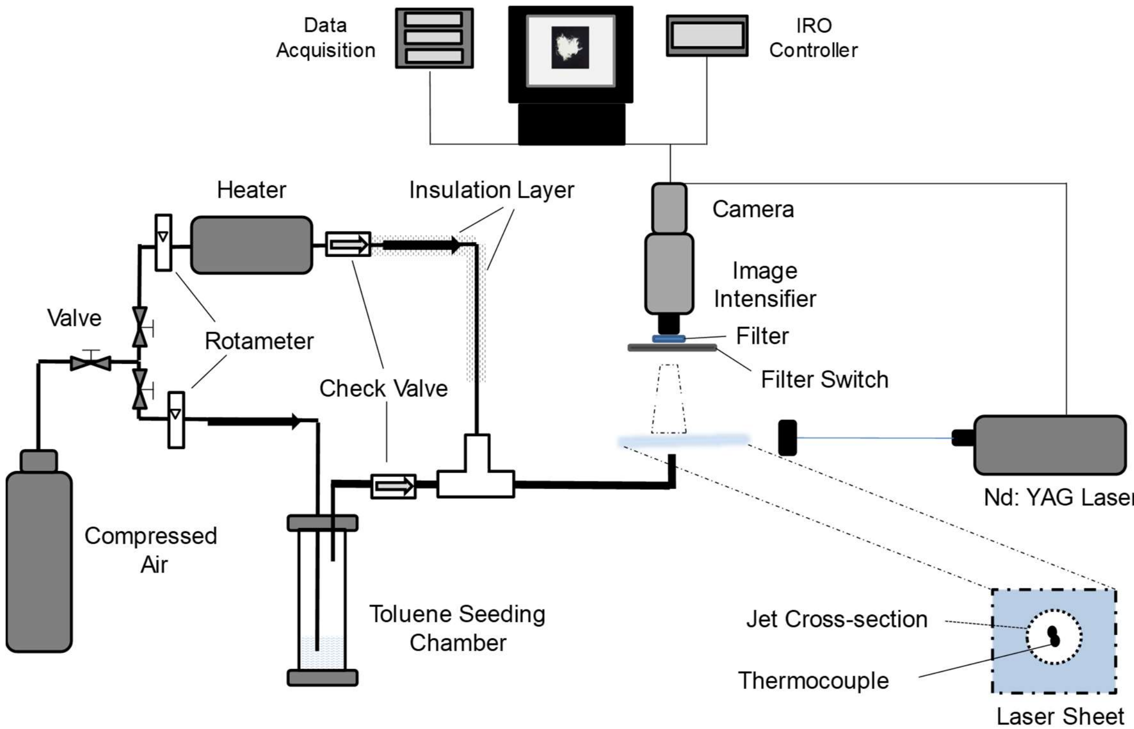

Figure 4.1. PLIF calibration setup

Calibration-Image Processing

As mentioned earlier in chapter two, fluorescence intensity is a function of parameters such as temperature, pressure, tracer concentration, and laser energy. In a general PLIF experiment, it is possible to control some factors such as temperature, pressure, and laser energy. However, it is almost impossible to control the concentration of the tracer. As a result, there is a need to apply the two color thermometry to remove the effect of concentration. The theory behind this method is explained in detail within chapter two. In this chapter, the procedure towards this method is illustrated for the purpose of developing an empirical relation between the temperature and toluene fluorescence intensity.

The PLIF experimental procedure consists of three main image recording stages: background images, air/toluene images at a reference temperature (known as reference images), and air/toluene images at different temperatures. For each stage two sets of 500 images are recorded: temperature dependent (using red filter) and temperature independent (using blue filter). Red and blue filters pass 320 nm and 285 nm wavelength, respectively. Since one camera is used for this study, it is not possible to capture both type of images simultaneously. Temperature dependent data are first taken using the red filter, then the filter is switched to the blue filter using the filter switch. The filter switch is controlled remotely by the same computer that is used for data acquisition.

Images are captured when the system reaches the steady state condition at a desirable temperature. For background images, the laser is illuminating the jet cross section; however, the flow is not seeded (no toluene in the flow). The purpose of capturing the background images is to record the optical noise that is created by the surrounding light. Background images are captured at each temperature. When capturing the background images for both filters is completed, the toluene is spread into the flow line through the seeding system. The seeding system uses the air at ambient temperature; therefore, the temperature at the jet cross section is closely monitored and recorded to assure the system is working under the steady state condition. After the system reaches the uniform desirable temperature, the air/toluene images are recorded while the laser is illuminating the cross section. Reference images are air/toluene images taken while the mixture of air and toluene flows in the system at room temperature (297 K). Figures 4.2.a and 4.2.b present single background images at $T \approx 297$ K (reference temperature) and at $T \approx 305$ K , respectively. Figures 4.3.a and 4.3.b illustrate single air/toluene images at $T \approx 297$ K (reference temperature) and at $T \approx 305$ K , respectively. Davis 8.3 software from LaVision is used to record the raw images. High resolution images are exported from Davis in the tagged image file (TIF) format then post processed using in-house MATLAB code (Appendix A). The procedure is repeated for a variety of temperatures between room temperature and 400 K.

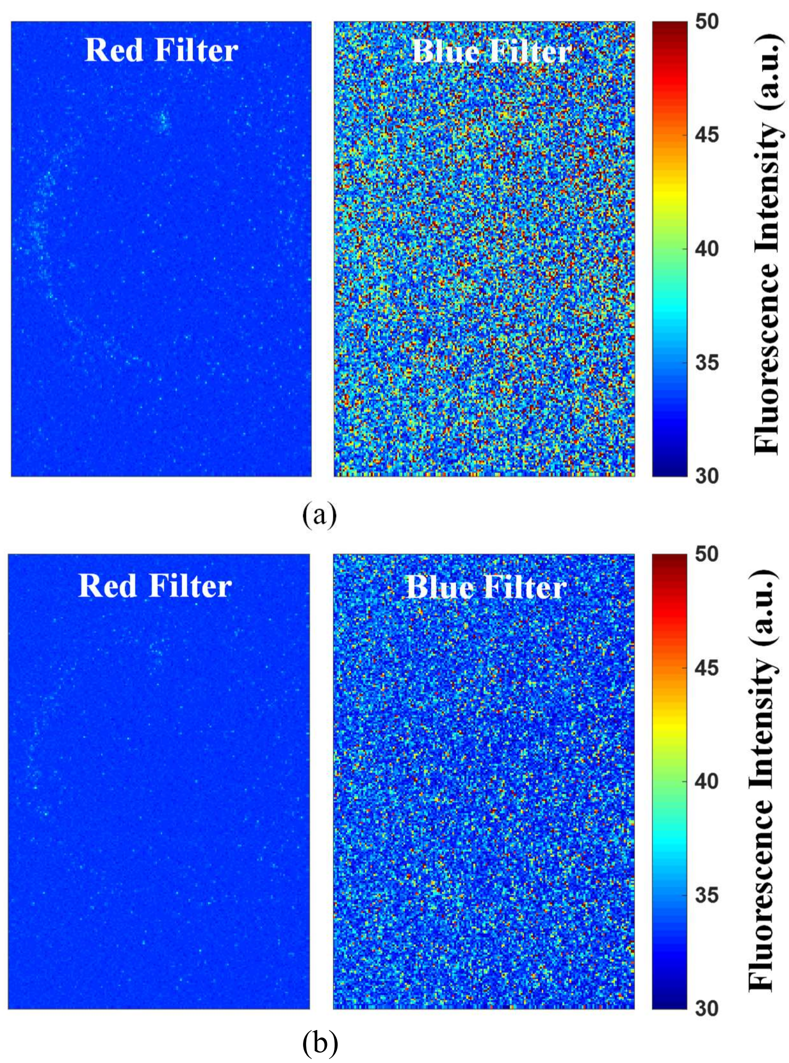

Figure 4.2. Intensity distribution of a single background image, a. T = 297.87 K (reference temperature), b. T = 306.21 K

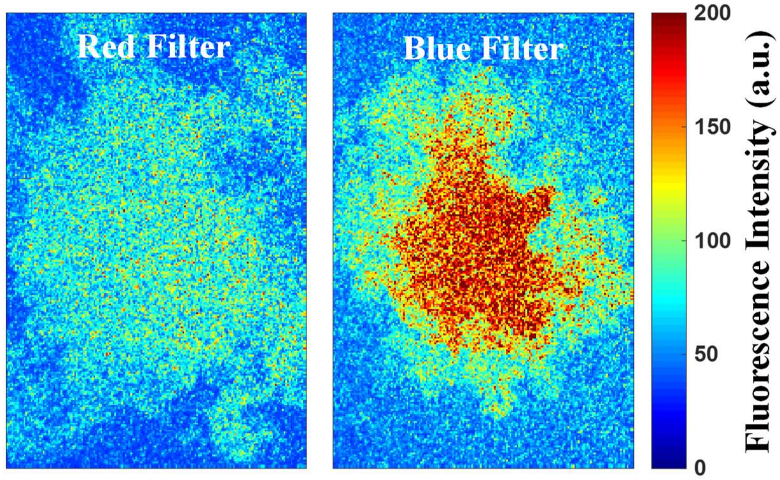

(a)

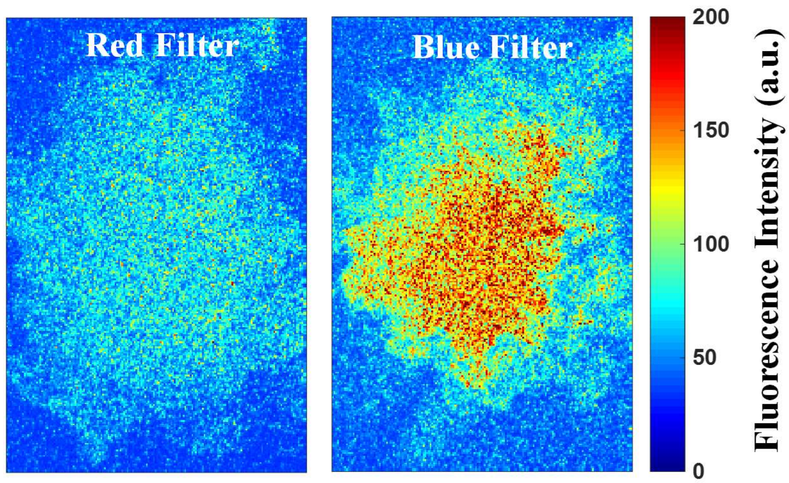

(b)

Figure 4.3. Intensity distribution of a single air / toluene raw image, a. T = 297.87 K (reference temperature), b. T = 306.21 K

The image processing includes the following steps: background subtraction, time averaging, normalizing the fluorescence intensity, and two color thermometry. The offset from camera noises and surrounding light is removed by subtracting the background intensity. For this purpose, 500 background images are averaged and then the averaged background image is subtracted from each single PLIF image. An averaged background image and background subtracted of each single image are shown in Figures 4.4 and 4.5, respectively. At this time, the surrounding noise is eliminated from the PLIF images and they are ready to be time averaged.

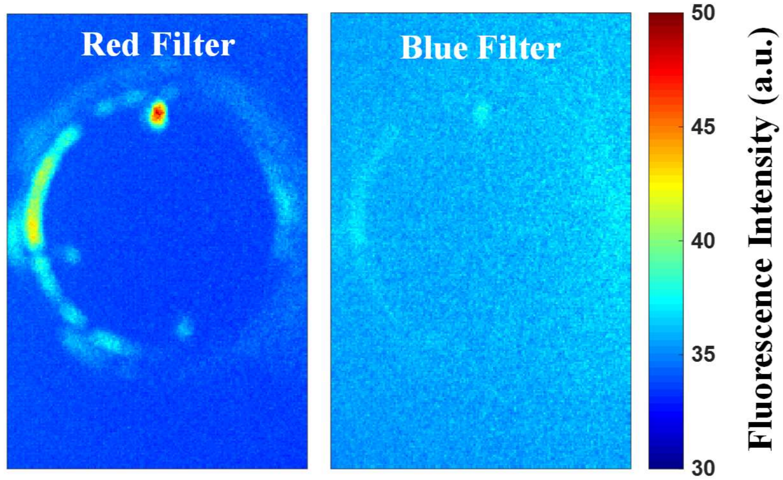

(a)

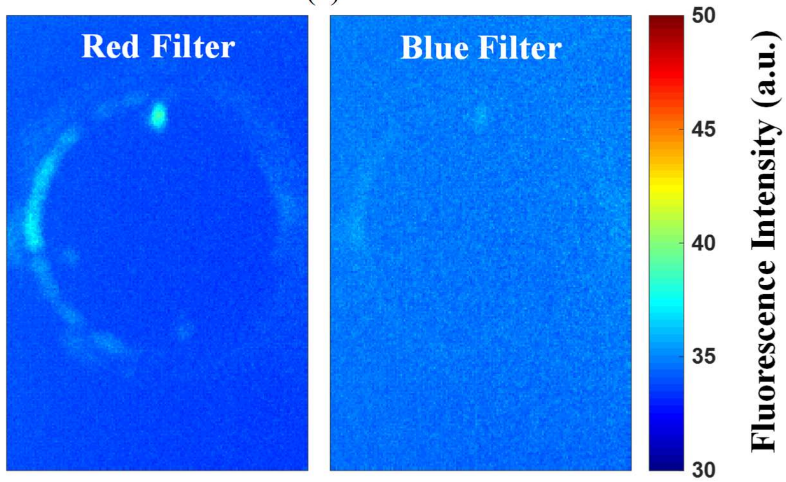

(b)

Figure 4.4. Intensity distribution of averaged background images, a. T = 297.87 K (reference temperature), b. T = 306.21 K

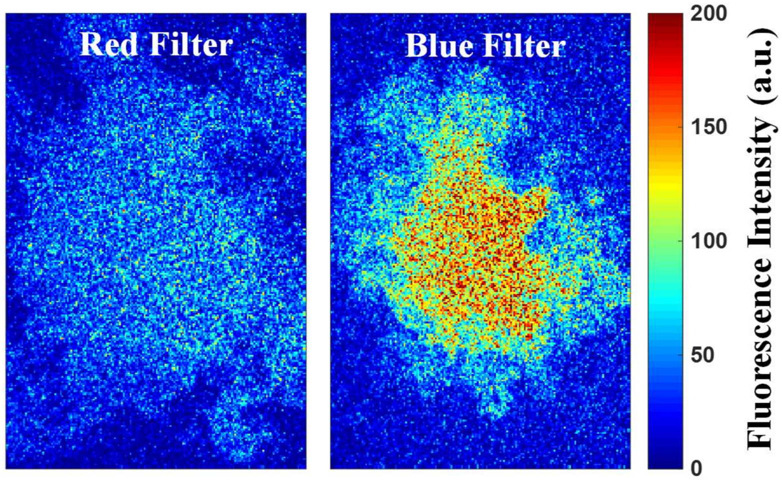

(a)

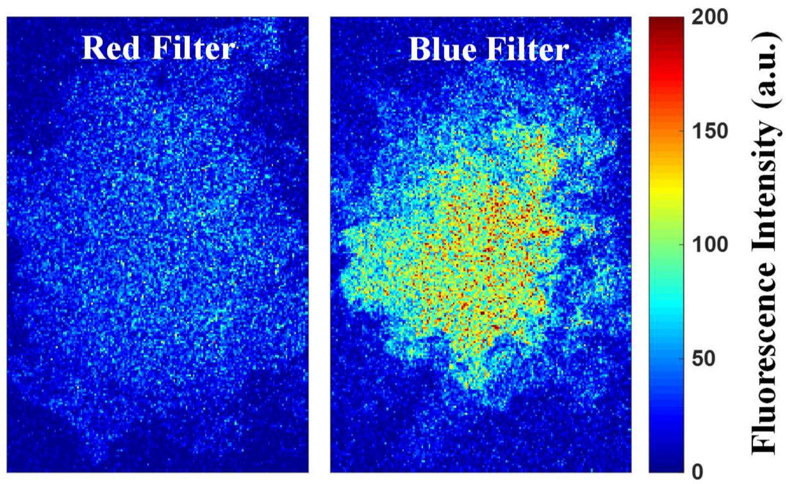

(b)

Figure 4.5. Intensity distribution of a single background-subtracted air / toluene image, a. T = 297.87K (reference temperature), b. T = 306.21K

As can be seen in Figure 4.3, some of pixels do not capture fluorescing tracer particles. The MATLAB code is written in a way that it includes the pixels with fluorescence intensity greater than zero for calculating the average. The time averaged images are shown in Figure 4.6. The two-color method is applied on the time averaged results; red filter intensities divided by blue filter intensities. The ratio eliminates the effect of concentration, the results for the reference temperature and T = 306.21K are provided in Figure 4.7. Then, the two-colored intensities (Figure 4.7.b) are normalized by the two colored results at the reference temperature (Figure 4.7.a).

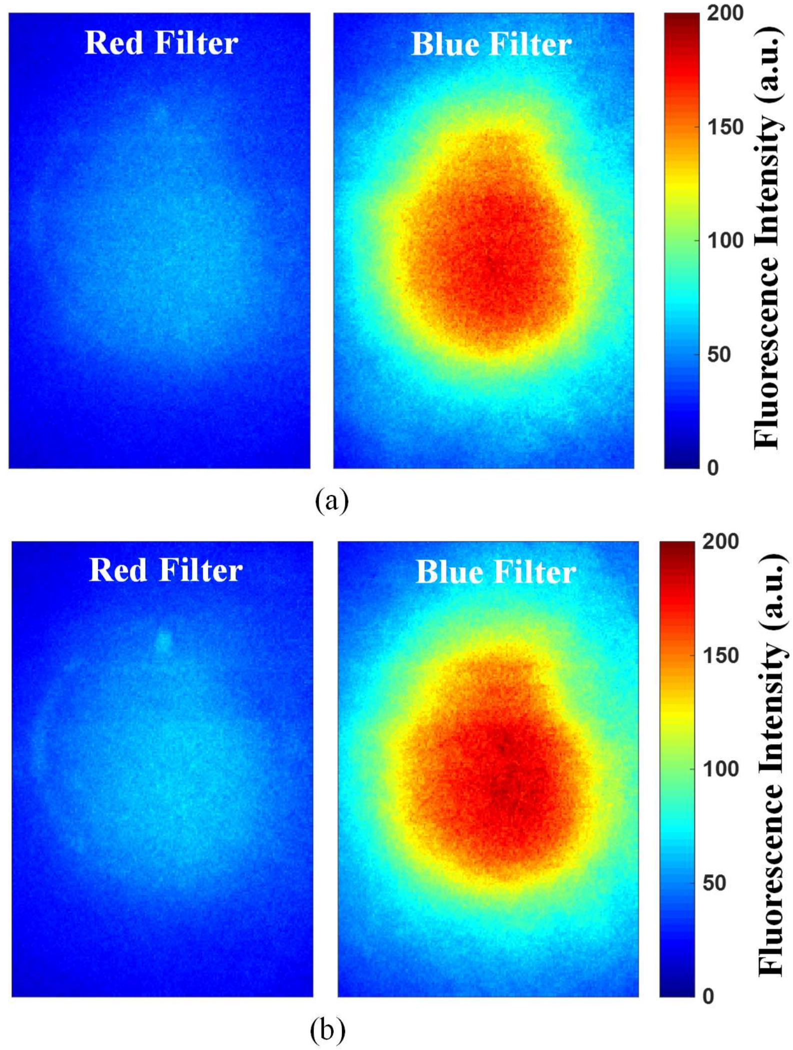

Figure 4.6. Intensity distribution of time-averaged background-subtracted air / toluene images, a. T = 297.87 K (reference temperature), b. T = 306.21 K

Figure 4.8 shows the results of the normalizing. The primary reason for normalizing is to reduce effects of inconsistencies in spatial illumination and camera sensitivity [3]. A flow chart regarding the post processing procedure, Figures 4.2 - 4.8, is provided in

Figure 4.9. The procedure is repeated for images at a variety of temperatures between room temperature and 400 K with the step size of 25 K.

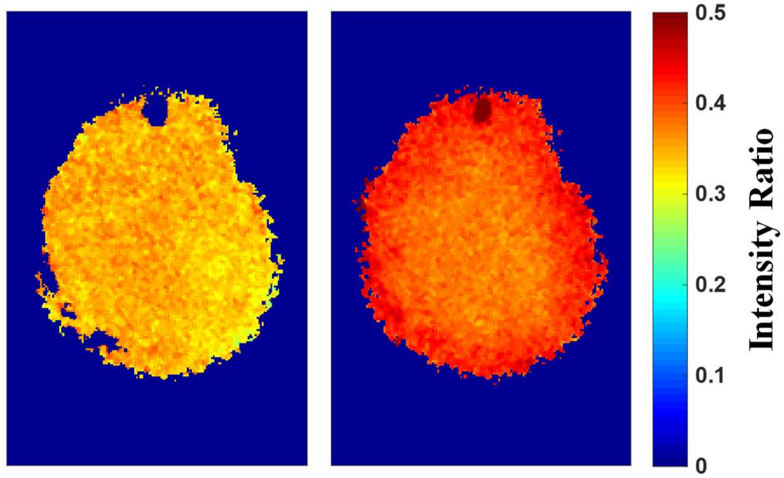

Figure 4.7. Intensity ratio distribution from two color method, a. T = 297.87 K (reference temperature), b. T = 306.21 K

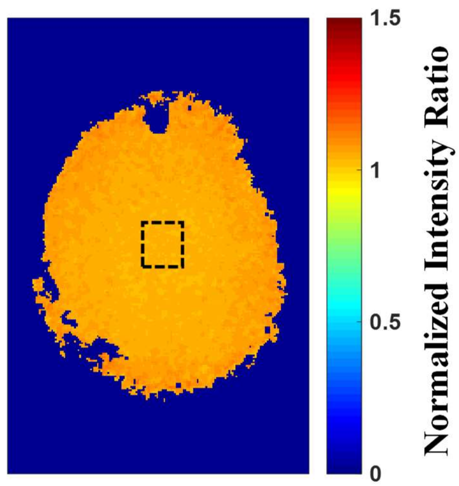

Figure 4.8. Normalized intensity ratio T = 306.21 K

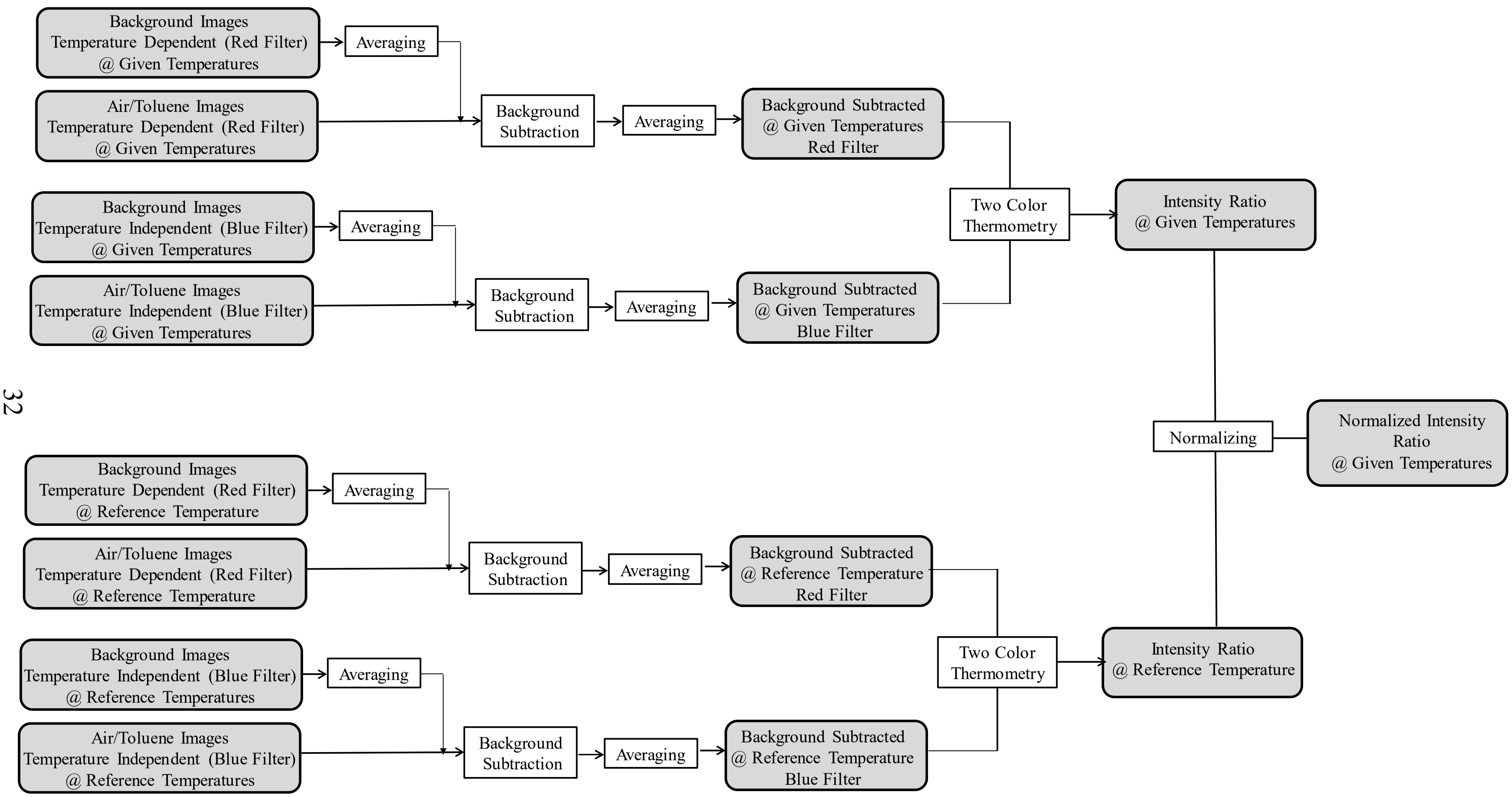

Figure 4.9. PLIF calibration procedure

In order to apply this method to measure the flow temperature, the relation between the fluorescence intensity and the flow temperature has to be determined. Therefore, a 10×10 pixel frame is created at the center area of the jet cross section for each temperature (Figure 4.8). Normalized intensity ratios (Equation 4.1) within the frame are averaged and recorded for each temperature. The normalized temperature is fitted (Equation 4.2) as a function of normalized fluorescence signal ratio I_N using the method of least squares regression with a 95% confidence interval. This function will then be applied to assign temperatures corresponding to each pixel for the measured PLIF ratio image. Figure 4.10 presents the data points that are used in the calibration process as well as the calibration curve. Six sets of data, each including five data points, were collected at different times, and used to create the calibration curve. The fitted equation for the linear method that describes the relation between the temperature and normalized fluorescence signal ratio is:

$$I_N = \left. \left(\frac{I_{Red} - I_{Back-Red}}{I_{Blue} - I_{Back-Blue}} \right) \right|_T \Big/ \left. \left(\frac{I_{Red} - I_{Back-Red}}{I_{Blue} - I_{Back-Blue}} \right) \right|_{T_{Ref}} \tag{4.1}$$

$$\frac{T}{T_{Ref}} = 0.6816 I_N + 0.3200 \tag{4.2}$$

The R-squared value for the regression is equal to 0.9235. Equation 4.2 can be used to predict the temperatures (K) corresponding to a range of value for normalized fluorescence signal ratio. The corresponding risk to accept the conclusion that Equation 4.2 is expressing the relationship between temperature and normalized fluorescence signal ratio is equal to 5%.

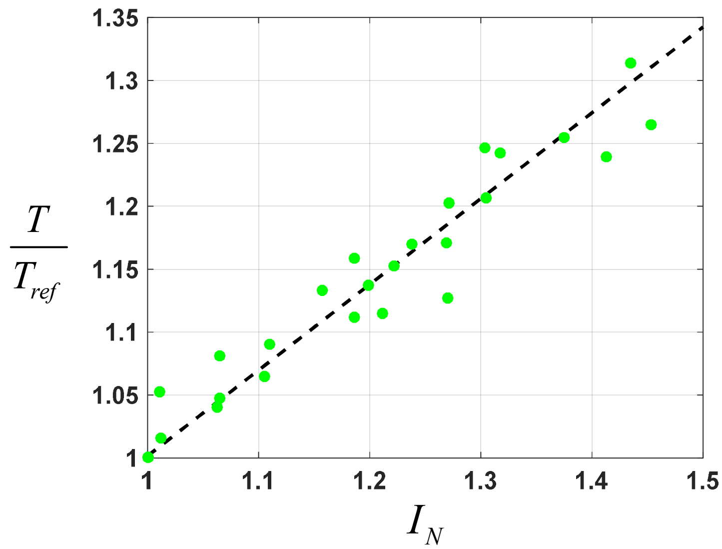

Figure 4.10. Regression for PLIF calibration

Repeatability of Calibration Experiment

For this study, the calibration is conducted under specific experimental conditions. The flow Reynolds number is approximately 10,000, the seeding setup is arranged in a way that 20% of the flow goes to the seeder and the rest goes to the heater, and 500 images are captured for each filter. In order to verify the repeatability of the calibration data, impacts of the three factors on calibration data are investigated: different Reynolds numbers, seeding setups, and number of images.

Two sets of calibration experiments are conducted at Re $\approx$ 5,000 and Re $\approx$15,000 and the results are compared with the data used for calibration curve at Re $\approx$10,000. As can been seen in Figure 4.11, data from varying the Reynolds number falls within the 95% confidence interval.

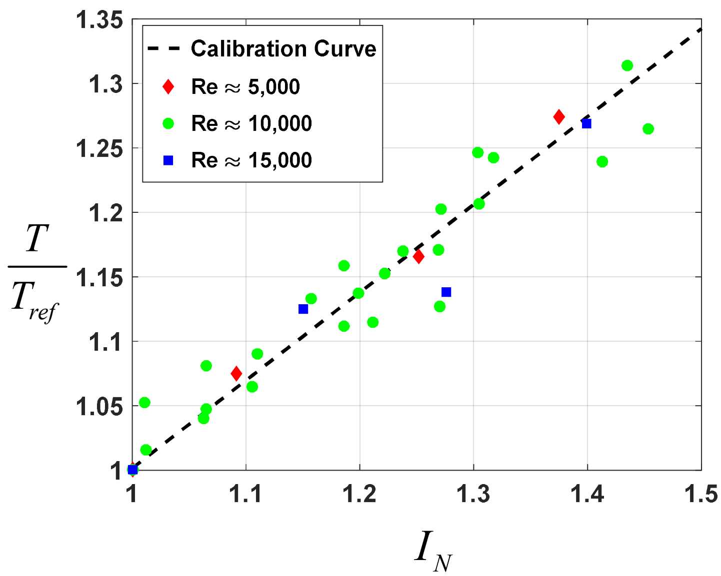

Figure 4.11. Impact of Reynolds number on PLIF calibration data

Three different seeding setups are used to validate the repeatability of the two color method at higher toluene concentrations. The setup arrangements are summarized in Table 4.1, and the results are compared in Figure 4.12. Seeding setup I is used to create the calibration data. Finally, the impact of number if images on the calibration data is studied. For this purpose, calibration experiments were conducted on four different days. Different numbers of images, with the range of 100 to 400, were captured on each day. Figure 4.13 shows a good agreement between the three seeding systems. Data from varying the toluene concentration falls within the 95% confidence interval. As was mentioned earlier in this chapter, for calibration post processing, a small area within center of the jet is used to collect the intensity information. However, for other applications that require a larger area, more images may be required.

Table 4.1. Toluene seeding setup arrangement for PLIF calibration

Seeding Setup	Heater Flow (%)	Seeder Flow (%)
Seeding Setup I	80	20
Seeding Setup II	75	25
Seeding Setup III	50	50

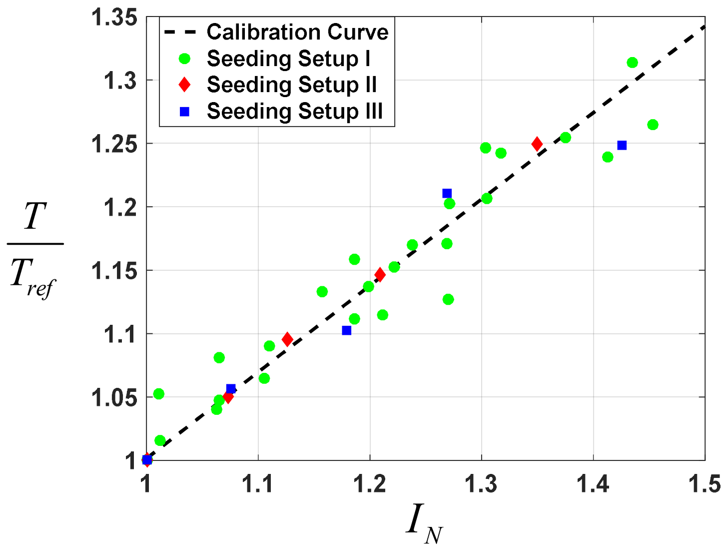

Figure 4.12. Impact of toluene seeding setup on PLIF calibration data

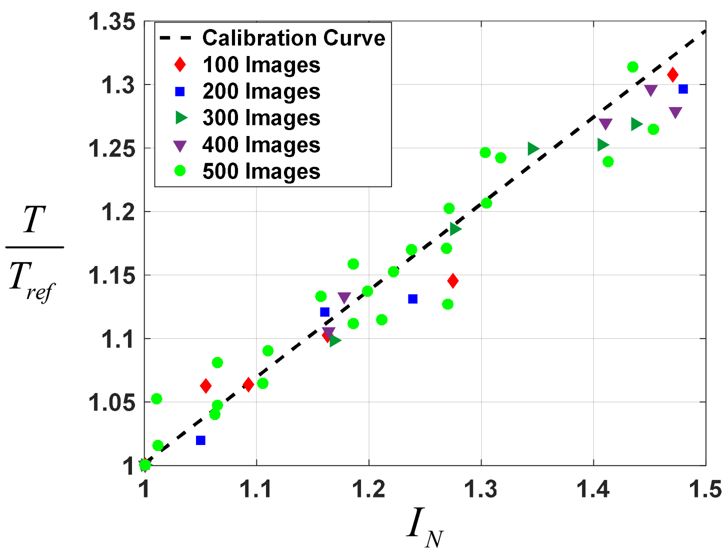

Figure 4.13. Impact of number of images on PLIF calibration data

Fluorescence Intensity Standard Deviation

The PLIF temperature distribution is determined in the following steps: background subtraction, two color method, and normalizing. The accuracy of each step contributes to the overall precision of the temperature measurement. Using theory of propagation for a given function:

$$X = f\left(A, B, C, \ldots\right), \tag{4.3}$$

The standard deviation of X is written as:

$$\sigma_X^2 = \left(\frac{\partial f}{\partial A}\sigma_A\right)^2 + \left(\frac{\partial f}{\partial B}\sigma_B\right)^2 + \left(\frac{\partial f}{\partial C}\sigma_C\right)^2 + \ldots \tag{4.4}$$

The calibration curve, Equation 4.2, can be described in a general form as

$$T = aI + b \tag{4.5}$$

If the calculation steps are added to Equation 4.5, the temperature can be written as:

$$T = T_{ref}\left(a\left.\left(\frac{I_{Red} - I_{Back-Red}}{I_{Blue} - I_{Back-Blue}}\right)\right|_{T} \Big/ \left.\left(\frac{I_{Red} - I_{Back-Red}}{I_{Blue} - I_{Back-Blue}}\right)\right|_{T_{Ref}} + b\right) \tag{4.6}$$

Thus, the fluorescence intensity of the raw images, references images, and background images are contributing to the overall precision of the PLIF method. Using Equation 4.4, the standard deviation of the temperature can be calculated as:

$$\sigma_T = \frac{T_{Ref}a}{\left(I_{Blue}-I_{Back-Blue}\right)\left(I_{Ref-Blue}-I_{Back-Ref-Red}\right)}\sqrt{\begin{array}{l}\left(I_{Ref-Blue}-I_{Back-Ref-Blue}\right)^2\left(\sigma^2_{I_{Red}}+\sigma^2_{I_{Ref-Blue}}\right)+\\ \dfrac{\left(I_{Red}-I_{Black-Red}\right)^2\left(I_{Ref-Blue}-I_{Back-Ref-Red}\right)^2}{\left(I_{Blue}-I_{Back-Blue}\right)^2}\left(\sigma^2_{I_{Blue}}+\sigma^2_{I_{Back-Blue}}\right)+\\ \dfrac{\left(I_{Red}-I_{Black-Red}\right)^2\left(I_{Ref-Blue}-I_{Back-Ref-Red}\right)^2}{\left(I_{Ref-Blue}-I_{Back-Ref-Red}\right)^2}\left(\sigma^2_{I_{Ref-Blue}}+\sigma^2_{I_{Back-Ref-Red}}\right)+\\ \left(I_{Red}-I_{Black-Red}\right)^2\left(\sigma^2_{I_{Ref-Blue}}+\sigma^2_{I_{Back-Ref-Blue}}\right)\end{array}} \quad (4.7)$$

The standard deviation of temperatures corresponding to the data used to create the calibration curve is calculated using Equation 4.7. The maximum standard deviation, based on post processing of 500 images, is equal to 12.50 K at 334.87 K. The maximum relative standard deviation for this study is approximately 3.73%, $\left(12.50\ \mathrm{K}/\ 334.87\ \mathrm{K}\right)$. Sensitivity of the standard deviation to each step varies at different temperatures. However, the calculations show that the background subtraction and two color method have the lowest and highest contribution to the standard deviation, respectively. At a maximum standard deviation of 3.73%, the proportion of background subtraction, two color method, and normalizing steps are, namely, 16.25%, 54.12%, and 29.63%.

The standard deviation is in agreement with literature standard deviation corresponding to LIF experiments. As an example, Kearney et al. [47] estimated the standard deviation of 1.8% for temperature measurement in a turbulent, thermal convection study using acetone-LIF. A standard deviation of 4.5% was reported by Byrne et al. [48] in PLIF temperature measurement in laminar hypersonic flat plate flows.

Standard deviations of temperature measurement are presented in Figure 4.14. As is seen, there is no evidence of a specific relationship between the standard deviation and temperature. This reveals that the operating temperature would not raise any concerns for the toluene PLIF application for temperature measurement purposes.

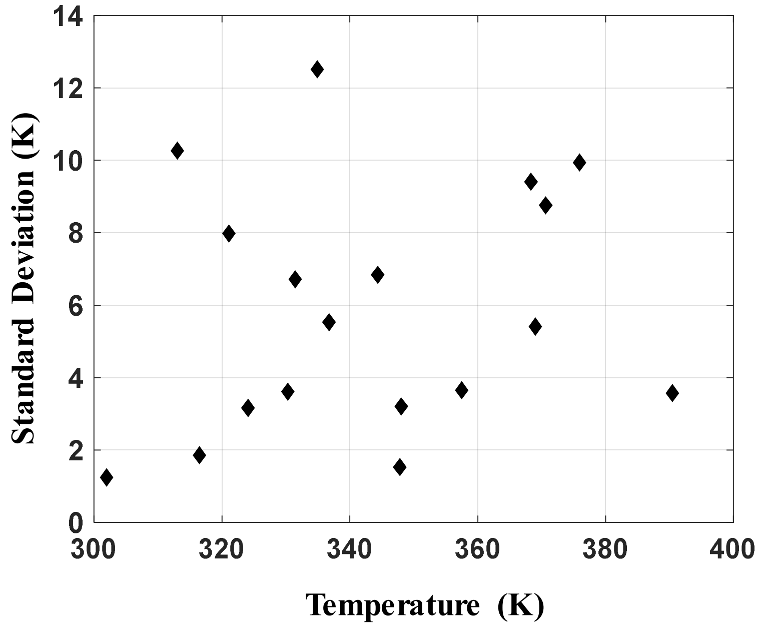

Figure 4.14. Standard deviation of fluorescence intensity measurements as a function of temperature for calibration data

Figure 4.14 only provides standard deviations of the fluorescence intensities collected through the calibration tests. Standard deviations corresponding to the slope and intercept of the calibration curve have to be considered to obtain the uncertainty of the calibration tests. Since a linear least squares curve fit is made for the calibration set of data, a standard error of regression can be applied to calculate the standard deviation corresponding to the slope and intercept [49]. The standard deviation for the slope and intercept from the calibration curve can be written as Equations 4.8 and 4.9, respectively.

$$S_a = \left(\frac{S_{T_N}^2}{S_{I_N I_N}} \right) \tag{4.8}$$

$$S_b = \left[S_{T_N}^2 \left(\frac{1}{N} + \frac{\bar{I}_N^2}{S_{I_N I_N}} \right) \right]^{1/2} \tag{4.9}$$

Where

$$\bar{I}_N = \frac{1}{N} \sum_{i=1}^{N} I_{N_i} \tag{4.10}$$

and

$$S_{I_N I_N} = \sum_{i=1}^{N} I_{N_i}^2 - \frac{\left(\sum_{i=1}^{N} I_{N_i} \right)^2}{N} \tag{4.11}$$

Using Equations 4.8-4.11, the standard deviation for the slope and intercept of Equation 4.2 is equal to 0.068 (9.94%) and 0.041 (12.75%), respectively. The theory of propagation can be used to combine the standard deviations of fluorescence intensities, calibration curve slope, and intercept. The overall uncertainty corresponding to calibration tests is equal to 16.59%.

The major sources of uncertainty for the PLIF calibration study could be related to camera noises, filter detectability error, laser energy, and toluene purity. Cameras create dark and shot noises. In the PLIF study, the majority of dark noises are removed through the background subtraction process. The shot noises are results of capturing undesirable information, and impact the image resolution. Sensitivity of the standard deviation to each of the steps (background subtraction, two color method, and normalizing) is calculated. It is found that the background subtraction step has the lowest impact on the standard deviation.

The standard deviation for the PLIF calibration has the highest sensitivity to the two color method step. In the PLIF calculation, the intensity ratio of the temperature dependent images to temperature independent images are calculated to eliminate the effect of concentration. For this study, a single camera is used to capture the temperature dependent and temperature independent fluorescence signals. Therefore, the two types of images are not recorded simultaneously. The delay between switching the filters and capturing two types of images could create errors.

For this study, a planar laser is used to induced toluene molecules. The laser energy may change within its plane, and results in creating an uncertainty. Two color method and normalizing can partially remove this effect. However, since two types of images (temperature dependent and independent) are recorded separately, the possibility that the laser energy varies during the data collection and its gradient impact the florescence quality. To reduce the laser energy error, the laser energy has to be monitored and adjusted during image collection using laser power meters.

Toluene impurity could contribute to error production. The PLIF method works based on capturing the toluene fluorescence intensity. The toluene molecules absorb the energy of the laser and travel to a higher energy state. The excited molecules emit energy, in the form of fluorescence, while they are reaching the equilibrium state. The presence of contamination and impurities in toluene could impact the energy absorption and photon emission.

The purpose of this study is to develop toluene based PLIF to study the thermal flow field. In this chapter, the setup and procedure to collect PLIF data for calibration purposes are offered. Finally, an empirical relationship between toluene fluorescence and temperature is developed and the repeatability of the calibration correlation is validated. This correlation can be applied to predict fluid temperature distribution within gaseous flows.

CHAPTER FIVE

PLIF Validation Using Free Jets

This study focuses on developing a novel non-intrusive method to measure the flow field temperature. In chapter four, an empirical relationship between the temperature and fluorescence intensity was developed. This chapter presents experimental results of a PLIF application on free jets for validation purposes. To start, a general background behind free turbulent flows is summarized. Secondly, features of the experimentation for the free jets are outlined. Finally, the results of PLIF experimentation are provided and compared with an analytical solution.

Turbulent Jets

Free turbulence flows are shear streams with high Reynolds number flow through an open environment fluid. A turbulent flow is known as free if it is not confined by a solid surface. Figure 5.1 shows three types of free turbulent flows; jets, wakes, and mixing layers. A free jet is formed when a flow leaves a nozzle or orifice and is discharged into a flow with a negligible velocity (Figure 5.1.a). A wake occurs behind a solid body which is traveling within a stagnant fluid (Figure 5.1.b). A mixing layer is created between two flows which are traveling at different velocities [12] .

Free jet flows are widely used in many engineering applications such as drying, cooling, propulsion, and air conditioning systems. The jets are flows with a specific momentum that spread into another fluid (usually a stagnant fluid).

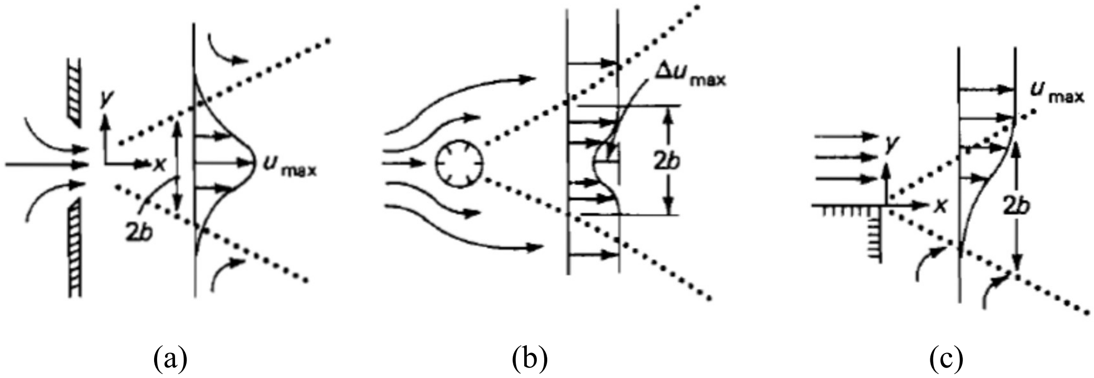

Figure 5.1. Free turbulent flow, a. Free jet, b. Wake of a body, c. Mixing layer [1]

Transition from laminar to turbulence for round jets occur at Reynolds numbers on the low side of 10^2 [50] and become fully turbulent for $\mathrm{Re} > 2,000$ [51]. Heat and mass transfer enhancement are special characteristics of the turbulent jets. There are two main arrangements for a jet: free or impinging. In a free jet flow, the jet is suitably far from a solid surface; therefore, the effects of the wall do not exist within the jet flow. However, in an impinging jet, a thin boundary layer is created on the surface. Thus, the effects of wall are not negligible. A general background of jet impingement is offered in chapter six.

Fellouah et al. [52] investigated the effects of jet Reynolds number at different distances downstream from the jet exit $(0 < X/D < 25)$ using a hot-wire technique to determine the differences in mean velocity and turbulence intensity distribution. The Reynolds numbers used for the experiment were 6,000, 10,000, and 30,000. It was shown that the impact of Reynolds number varies at different regions of the jet. The effect of the Reynolds number is more significant within the shear layer region. It was also found that by increasing the Reynolds number, the thickness of the boundary layer at the jet exit decreases and the length of the potential core increases.

There are some experimental studies with the main purpose of illustrating the behavior of the flow using visualization techniques. Popiel et al. [53] visualized the behavior of natural free jets, for two Reynolds numbers of 10,000 and 20,000, at regions near the nozzle exit using the smoke-wire flow visualization technique. It was found that the creation of vortices near the nozzle exit disturbs the boundary layer and leads to the elongation of the jet core. Kwon et al. [54] used the particle image velocimetry (PIV) method to obtain the jet mean velocity and study the impact of Reynolds number on development of flow regions within free jets. It was found that the turbulent flow spreading rates gradually decreased by increasing the Reynold number. Dimotakis et al. [55] used laser induced fluorescence and particle streak velocity methods to obtain some physical insights into the structure and dynamics of turbulent jets.

The most available visualization techniques, such as smoke-wire, can illustrate the flow structure; however, to gain deeper understanding of the flow and turbulent phenomena, there is a need to obtain detailed information about the velocity and temperature field. Traditional techniques such as thermocouples and hot/cold wires provide information at locations where the instruments are implemented. It is impossible to obtain a detailed distribution of velocity and temperature for the whole flow field. Any measurement probes are counted as an external object and disturb the flow field.

Recently many researchers have been using the PIV method to study the flow field. There is still a need to investigate the thermal flow fields, especially within the boundary layers where obtaining measurements is complicated. There are some theoretical studies available for the prediction of turbulent temperature distributions. Several assumptions are used to obtain a theoretical solution for simplification purposes. The theoretical models still need to be verified and this cannot be done correctly without having appropriate experimental data.

Theory Behind Free Jets

Development of the free shear layer on the edge of a free jet is presented in Figure 5.2. Large eddies impact the interface between the jet stream and stagnant fluid, and thus the thickness of the shear layer forming along the interface [50]. The thickness of the shear layer increases as the fluid moves away from the nozzle exit [56]. In order to study the shear layer thickness, the temperature and velocity distributions of the jet need to be predicted.

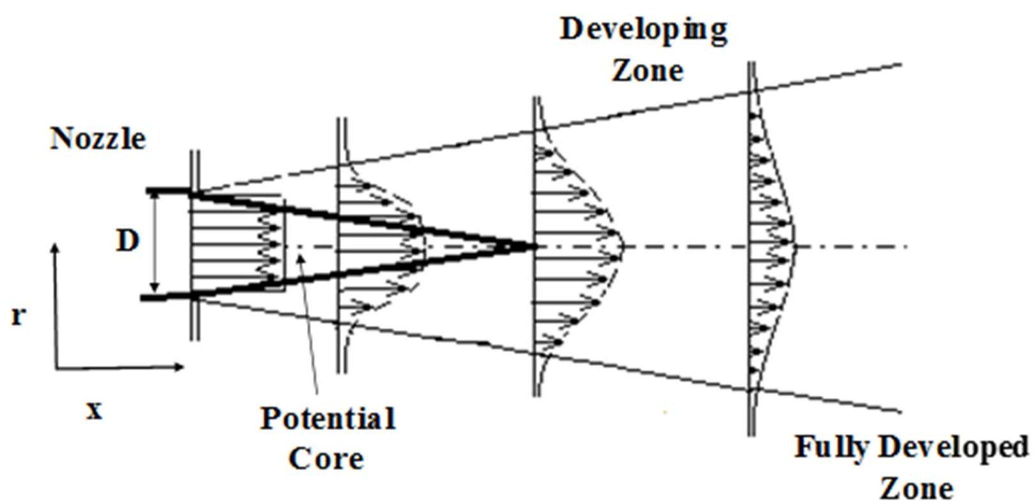

Figure 5.2. Details of the development of a round free jet [50]

Temperature and velocity distributions can be found by solving the continuity, momentum, and energy equations (governing equations) [50, 57, 58]. Assuming that the flow is steady, flow density is constant and its variation is not linked to the pressure (incompressible flow), and the flow structure is two dimensional, the governing equations are written as Equations 5.1-5.3.

$$\frac{\partial \overline{u}}{\partial x}+\frac{-1}{r}\frac{\partial}{\partial r}\left(r\overline{v}\right)=0 \tag{5.1}$$

$$\overline{u}\frac{\partial \overline{u}}{\partial x}+\overline{v}\frac{\partial \overline{u}}{\partial r}=-\frac{1}{\rho}\frac{d\overline{P}}{dx}+\left(\nu+\varepsilon_M\right)\frac{1}{r}\frac{\partial}{\partial r}\left[r\frac{\partial \overline{u}}{\partial r}\right] \tag{5.2}$$

$$u\frac{\partial \overline{T}}{\partial x}+v\frac{\partial \overline{T}}{\partial r}=\left(\alpha+\varepsilon_H\right)\frac{\partial}{\partial r}\left[r\frac{\partial \overline{T}}{\partial r}\right] \tag{5.3}$$

In order to solve the continuity and momentum equations numerically, three major assumptions are usually made. First, the pressure gradient is negligible in the longitudinal direction $\left(d\overline{P}/dx=0\right)$. Second, the kinematic viscosity is much smaller than the momentum eddy diffusivity $\left(\nu \ll \varepsilon_M\right)$ and can be omitted from the momentum equation. Third, the momentum eddy diffusivity is assumed to be constant for turbulent round jets [50]. For the energy equations, the first and second assumptions are applied: $\alpha \ll \varepsilon_H$ and ε_H is constant. It is also assumed that the turbulent Prandtl number is equal to one:

$$\Pr_t=\frac{\varepsilon_M}{\varepsilon_H}\cong 1 \tag{5.4}$$

Applying the mentioned assumptions, the boundary layer momentum and energy equations reduce to the following equations:

$$u\frac{\partial \overline{u}}{\partial x}+\overline{v}\frac{\partial \overline{u}}{\partial r}=\varepsilon_M\frac{1}{r}\frac{\partial}{\partial r}\left[r\frac{\partial \overline{u}}{\partial r}\right] \tag{5.5}$$

$$u\frac{\partial \overline{T}}{\partial x}+v\frac{\partial \overline{T}}{\partial r}=\varepsilon_H\frac{\partial}{\partial r}\left[r\frac{\partial \overline{T}}{\partial r}\right] \tag{5.6}$$

A similarity solution is used to solve the governing equations analytically. Similarity solutions are techniques for reducing a partial differential equation (governing equations) to an ordinary differential equation or to a simplified partial differential equation with fewer independent variables.

Before applying the similarity solution, the relationship between u and x is determined by integrating the momentum equation from $r = -\infty$ to ∞ [1].

$$\int_{-\infty}^{\infty}\overline{u}_c{}^2dr=U_0^2D_0 \tag{5.7}$$

The order of magnitude of $\overline{u}^2D_x$ is equal to $U_0^2D_0$. Assuming: $D_x/D_0=x/x_0$

$$\overline{u}_c/U_0=\left(x/x_0\right)^{1/2} \tag{5.8}$$

which $\overline{u}_c$ is the velocity at the centerline of the jet, D_0 and U_0 are the diameter and velocity of the jet at the nozzle exit, respectively. The similarity variable is defined as:

$$\eta\left(x,r\right)=\gamma\frac{x}{r} \tag{5.9}$$

$$\overline{u}=U_0\left(\frac{x}{x_0}\right)^{-1/2} \tag{5.10}$$

The streamfunction corresponding to the similarity solution is written as

$$\overline{\psi}=\frac{1}{\gamma}U_0x_0^{1/2}x^{1/2}F\left(\eta\right) \tag{5.11}$$

Where,

$$\overline{u} = \frac{\partial \overline{\psi}}{\partial r} \tag{5.12}$$

$$\overline{v} = -\frac{\partial \overline{\psi}}{\partial x} \tag{5.13}$$

The momentum equation is reduced to a dimensionless function:

$$\left(F^{'}\right)^{2} + FF^{"} + \frac{1}{2}F^{'''} = 0 \tag{5.14}$$

The boundary conditions used to solve the reduced dimensionless function are listed in Equations 5.15 and 5-16:

$$F = 0 \text{ and } F^{"} = 0 \qquad \text{at } \eta = 0 \tag{5.15}$$

$$F^{'} = 0 \qquad \text{at } \eta = \infty \tag{5.16}$$

Similarity solutions for the turbulent free shear layer problem are written as Equations 5.17 and 5.18. The details of the steps to obtain the solution can be found in open literature [1, 50].

$$\overline{u} = \frac{U_0}{2}\left[1 + erf\left(\sigma \frac{r}{x}\right)\right] \tag{5.17}$$

Reichardt [59] showed that there is a relationship between the temperature and velocity fields as

$$\frac{\overline{T} - T_\infty}{T_0 - T_\infty} = \left(\frac{\overline{u}}{U_0}\right)^{Pr_t} \tag{5.18}$$

Thus:

$$\frac{\overline{T} - T_\infty}{T_0 - T_\infty} = \left(\frac{1}{2}\left[1 + erf\left(\sigma \frac{r}{x}\right)\right]\right)^{\Pr_t} \tag{5.19}$$

The empirical value for σ is reported to be equal to 13.5 for the linear growth of the shear layer [50]. For this study, the similarity solution results are used to validate the PLIF experimental method and will be discussed later in this chapter.

Experimentation Facility

The general overview of the flow line was described in chapter two. All experimentation done for this dissertation was performed in the Convective Heat Transfer Laboratory (CHTL) at Baylor University. The Baylor PLIF experimental facility consists of an air compressor, flowmeters, pressure gauge, inline pipe heater, optical setup, toluene seeder, and data acquisition system. The existing PLIF setup is shown in Figure 5.3. The jet temperature and jet Reynolds number can be independently varied to fully characterize the flow field temperature.

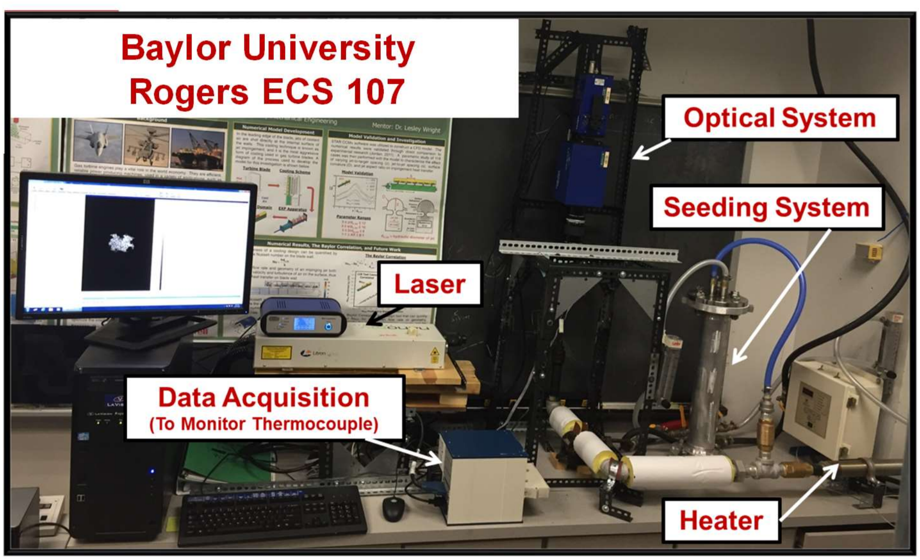

Figure 5.3. Baylor PLIF test section

The compressed air is supplied to the CHTL laboratory by a large compressor in the basement of the Baylor Rogers Engineering and Computer Science Building. In order to remove the moisture from the air, upon entering the laboratory, two moisture separators are located on the compressed air line.

The flow rate through the system is determined using the appropriate Reynolds number based on the tube inner diameter. There are flowmeters and pressure gauges in the PLIF test section to measure the air flow rate for accurate calculation of Reynolds number. The jet Reynolds number is written as:

$$\mathrm{Re} = \frac{\rho U D}{\mu} \tag{5.20}$$

An inline heater from Farnam Custom Product is used to generate high temperature jets. The entire line is wrapped in fiberglass insulation to reduce heat loss from the test section. Standard T-type thermocouples are placed at desirable locations to monitor the flow temperature. The thermocouples' output is monitored and recorded using LabVIEW software from National Instruments. The output temperatures are recorded every second and written to a data file. The details of the PLIF test section piping, optical and laser setup, and data acquisition system are provided in the chapter four.

Jets Configuration

The flow path of air for the free jet is very similar to the calibration setup (Chapter Four). The jet cross section was used for the calibration purposes. For the PLIF validation, a streamwise cut at the center of the jet is desirable. In order to produce a free jet, a 0.0127 m diameter aluminum tube is connected to the PLIF flow line using the appropriate fitting. The tube length and jet diameter are 0.2540 m and 0.0127 m, respectively. The ratio of the jet length-to-jet diameter is equal to 20. The thermal entrance length for turbulent flow is approximately equal to ten pipe dimeters [60]. For this study, the tube is long enough to produce fully developed flow.

A schematic of the free jet setup is shown in Figure 5.4. The camera is placed at a distance from the jet to record the length equal to 0.127m downstream of the jet exit. The jet temperature is measured at the center of the jet at the nozzle exit, and varies between 300 K to 375 K with the step size of 25 K. Three Reynolds numbers of 5,000, 10,000, and 15,000 are used to produce turbulent free jets. The jet exit, jet streamwise cut, origin and the coordinate system used to present the free jet results are also illustrated in Figure 5.4.

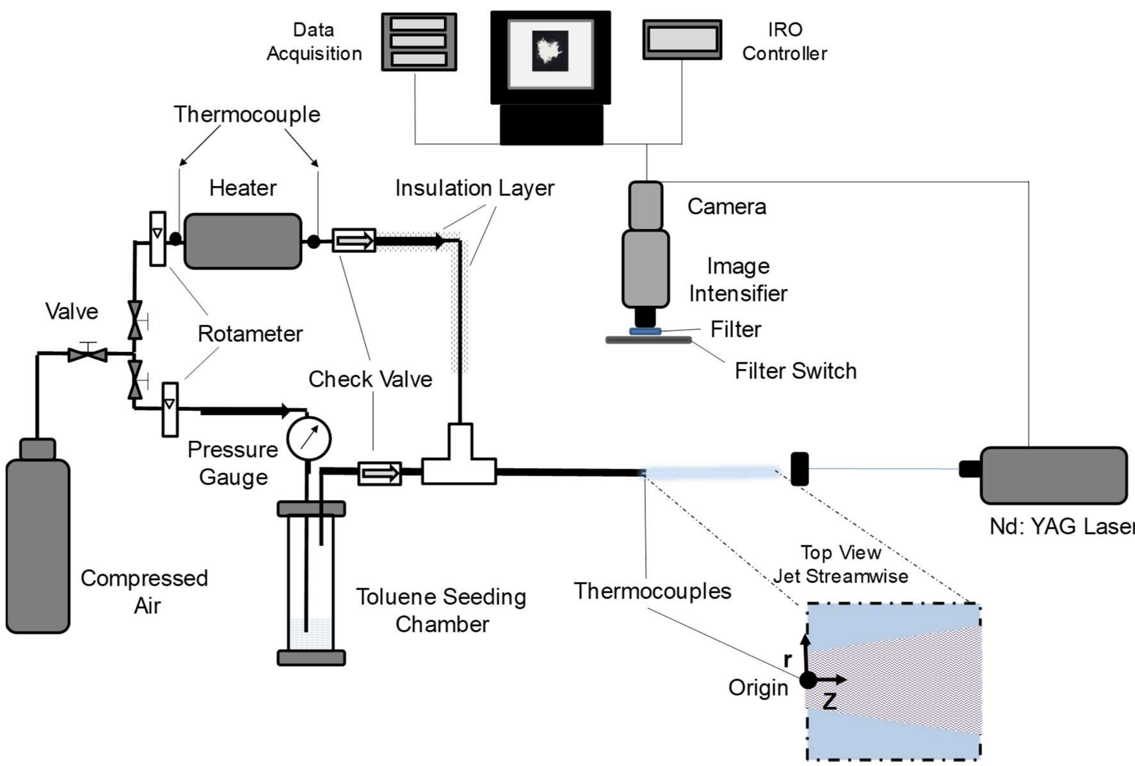

Figure 5.4. Sketch of free jet experimentation facility

Experimental Procedure

The PLIF experimental procedure for free jet tests consists of three main image recording steps: background images, reference images, and air/toluene images at different experimental conditions. For each step, two sets of 500 images are recorded: temperature dependent (using red filter) and temperature independent (using blue filter). Background images are captured while the laser is on and there is only airflow in the system (no tracer particles). Reference images are taken while the mixture of air and toluene is flowing in the system at room temperature (297 K) and the laser is on. Background images are taken for each filter at each temperature. There are two thermocouples located at the center of the jet at the nozzle exit. The temperature is closely monitored. After the jet reaches the steady state condition (constant temperature at the tube outlet), the toluene is introduced to the flow line from the seeding system. It is important to monitor the total flowrate to maintain the same Reynolds number. The air/toluene images are recorded while the laser is on. Davis 8.3 software from LaVision is used to record the raw images. For each step, flow and ambient temperatures, gauge pressure, and flowrate are monitored and recorded. Images are exported from Davis in the tagged image file (TIF) format then post processed using an in-house MATLAB code (Appendix A).

Data Reduction

The data reduction for free jet experiments is very similar to the calibration data reduction (Chapter Four). However, in order to reduce the noise, the two color method process is slightly different for the free jet experiment. For the calibration image processing, a very small area located at the center of the jet cross section was desirable to collect the intensity information. However, for the free jet tests, the whole jet is studied for the PLIF validation. As was mentioned in Chapter Four, there are some pixels that do not capture fluorescing tracer particles. Figure 5.5 illustrates an example of a single raw image of a free jet; as can be seen, there are some areas that do not carry the valuable fluorescence signal. Including these pixels in the time averaging process and two color method would lead to increase the uncertainty of the experiment as well as including additional noise.

For this investigation, the 500 single raw images are background subtracted and time averaged. It is important to note that only pixels that carry an intensity magnitude greater than zero are considered in the time averaging process. A distribution of the number of images that carry desirable intensities (intensity greater than zero) for the time averaged images are created. This distribution, known as count, is used later as a threshold for the two color method procedure. The count distribution presents how many images at each pixel are used for the time average process. In the other words, it shows the distribution of the number of images that capture fluorescence tracer particle at each pixel. Figure 5.6.a-d illustrates the time averaged images for temperature dependent (red filter) and temperature independent (blue filter) images, as well as the count distribution for each of the averaged images.

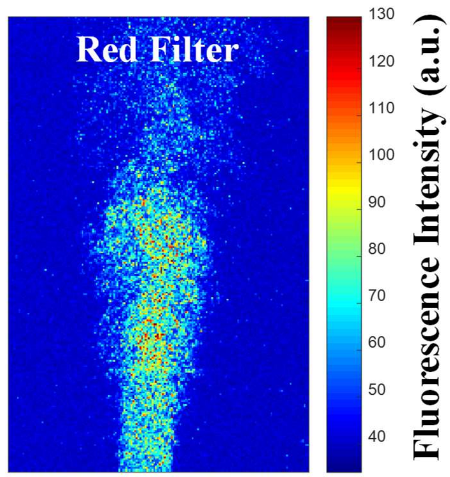

Figure 5.5. Fluorescence distribution of a single air/toluene raw image, T = 324.60 K and Re = 10,000

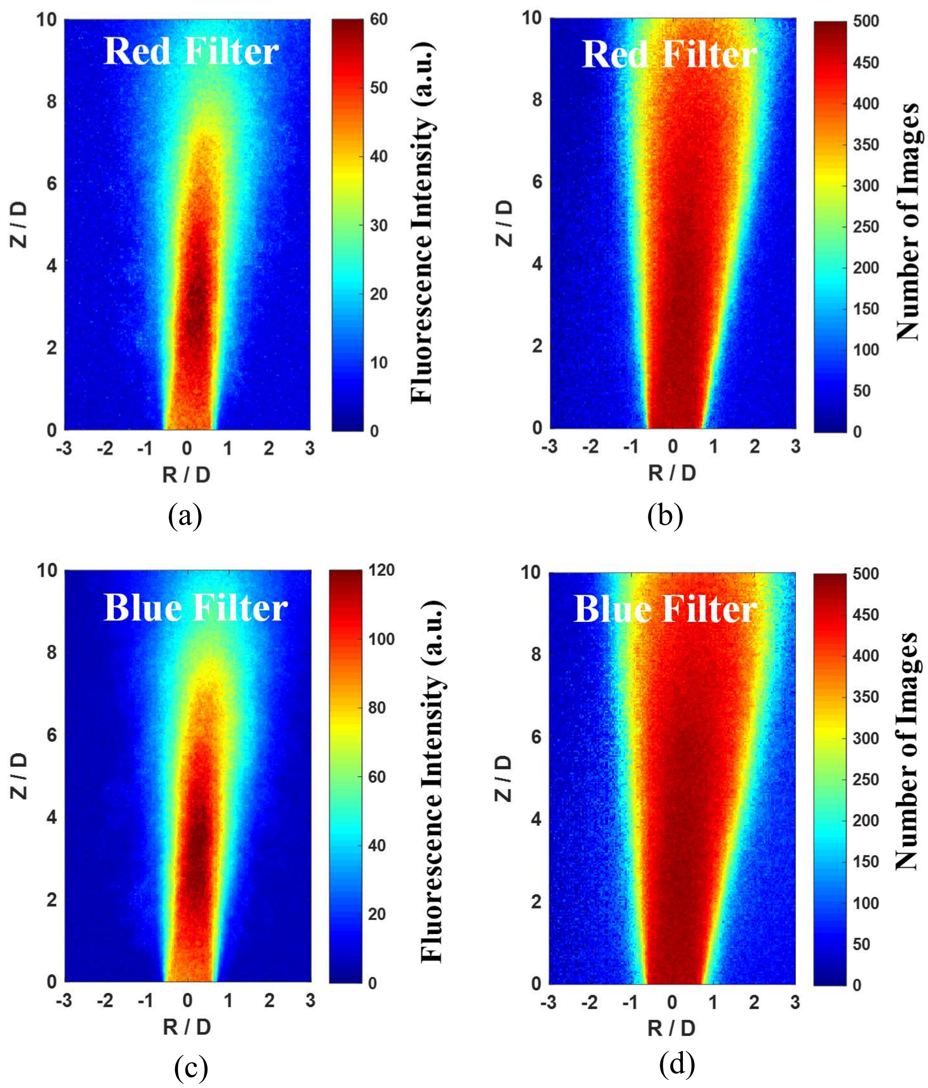

Figure 5.6. Time averaged air / toluene images at T = 296.60 K and Re = 10,000, a. Temperature dependent intensity distribution, b. Temperature dependent count distribution, c. Temperature independent intensity distribution, d. Temperature independent count distribution

In order to apply the two color method, propagation of the temperature dependent and the temperature independent count is calculated as

$$\text{Combined Count} = \sqrt{(\text{Temperature Dependent Count})^2 + (\text{Temperature Independent Count})^2} \tag{5.21}$$

The combined count distribution is shown in Figure 5.7.a. The median value of the combined count is extracted and used as a threshold for the two color method. Pixels of the time averaged images that carry a count greater than the median value of the combined count are used in the two color method (Figure 5.7.b). The in-house MATLAB codes that are used for processing are provided in the Appendix A. The same procedure is repeated on the free jets at higher temperatures. Figure 5.8 presents the post processing results on the free jet at T = 324.60 K and Re = 10,000.

The room temperature is the reference temperature for this experiment. The intensity ratio at the reference temperature is used in the normalizing procedure. The normalized image is the result of dividing the intensity ratio image from Figure 5.8 by intensity ratio image from Figure 5.7. The normalized intensity ratio distribution is shown in Figure 5.9. The normalizing procedure reduces the effect of inconsistencies in spatial illumination and camera sensitivity. In order to calculate the temperature distribution, the PLIF calibration correlation, Equation 4.2, is applied to the normalized intensity ratio. The temperature distribution for T = 324.6 K at Re = 10,000 is presented in Figure 5.10.

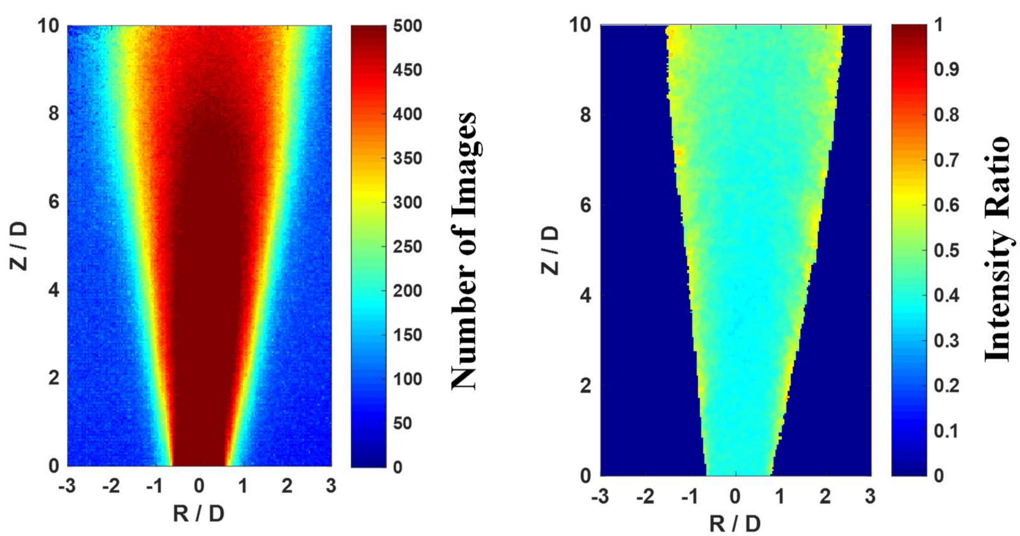

(a) (b)

Figure 5.7. Free jet two color method at T = 296.60 K and Re = 10,000, a. Combined count distribution, b. Intensity ratio distribution

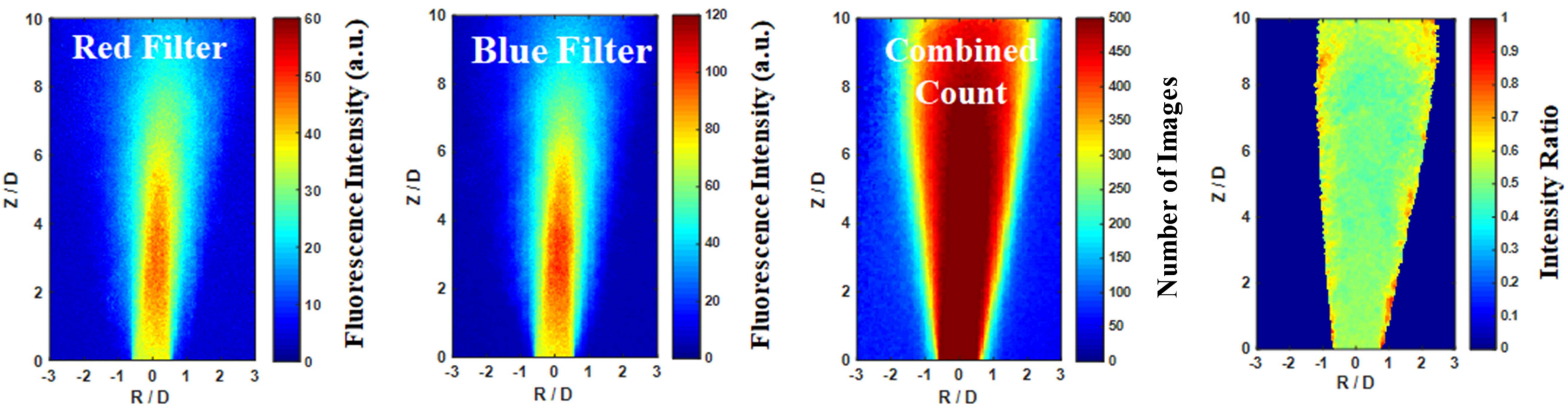

Figure 5.8. Two color method, T = 324.60 K and Re = 10,000

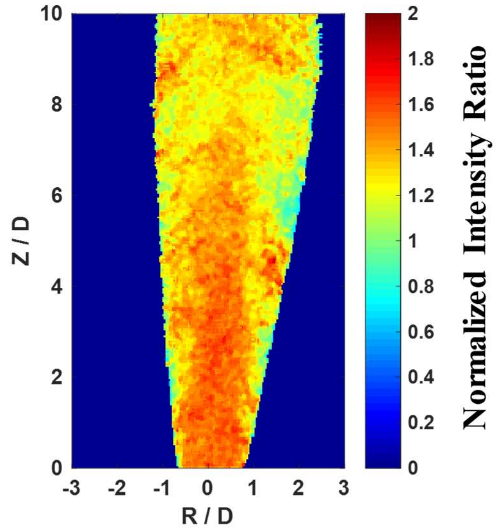

Figure 5.9 Normalized intensity ratio, T = 324.60 K, Re = 10,000

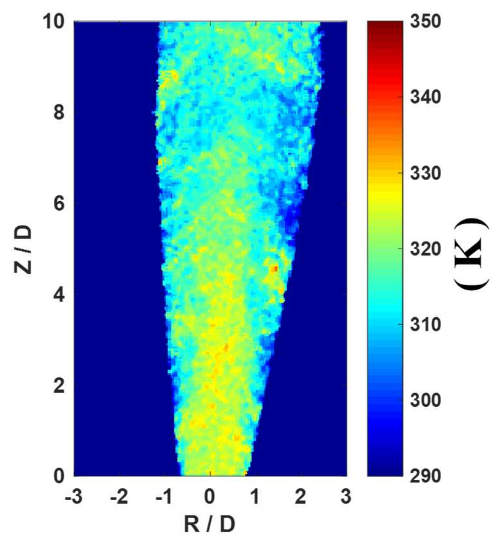

Figure 5.10. Temperature distribution, T = 324.60 K, Re = 10,000

For the free jet experiments, 500 images are recorded for each test. The impact of number of images on the experiments are studied to confirm that 500 image are an adequate number. For this purpose, a comparison was conducted among a variety of numbers of images that are used for the post processing. Figure 5.11 presents the impact of the number of images on the lateral temperature distribution at downstream location of Z / D = 5 for free jets at T = 324.60 K and Re = 10,000. As is seen, the data corresponding to 50 images are dispersed. As the number of images is increased, the data consistency improves. The impact of the number of images on the PLIF results are studied for all cases. At a 95% level of confidence, the data provide sufficient evidence that using more than 350 images does not affect the results.

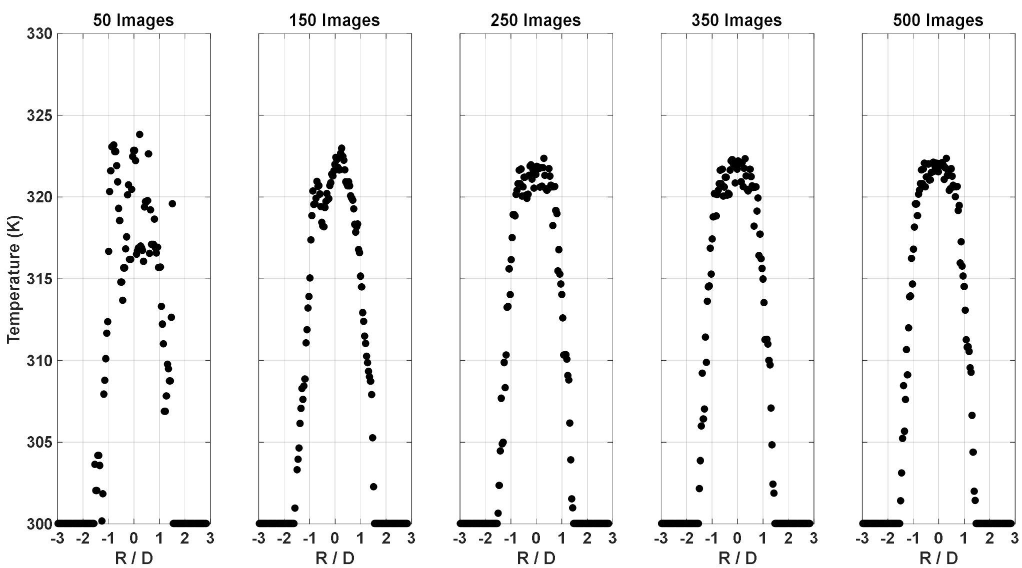

Figure 5.11. Impact of number of images on PLIF free jet results, Z / D =5, T = 324.60 K, and Re = 10,000

PLIF Free Jets Results

For this study, free jet tests are created at nozzle temperatures between 300 – 375 K with the step size of 25 K. From these cases, impacts of jet Reynolds number on thermal development are investigated to validate the PLIF technique. The test cases are summarized in Table 5.1.

Table 5.1. Free jet test cases

Re	Temperature (K)
5,000	300, 325, 350, 375
10,000	300, 325, 350, 375
15,000	300, 325, 350, 375

Detailed temperature distributions for cases with Re = 10,000 are presented in Figure 5.12. The temperatures at the jet nozzle exit, recorded by thermocouples, are provided above the distribution. The PLIF experimental results near the jet exit closely agree with the thermocouple data. The relative error for the temperature near the jet exit, $\left|\left(T_{PLIF} - T_{TC}\right)/T_{TC}\right|$, for all cases are less than 6%. The standard deviation analysis for whole jets is performed on the case with Re = 10,000. The details of the standard deviation calculation were provided in Chapter Four. The relative uncertainties for the free jets at jet nozzle temperatures equal to 300.30 K, 324.60 K, 347.70 K, and 372.40 K are equal to 0.98%, 1.58%, 3.18%, and 2.76%, respectively. The uncertainties calculated for free jets agree with the calibration uncertainties found in Chapter Four.

The free jet experiments were conducted on different days. Thus, the reference temperature (room temperature) is not constant for all cases. The impact of this change is mostly eliminated through the normalizing process.

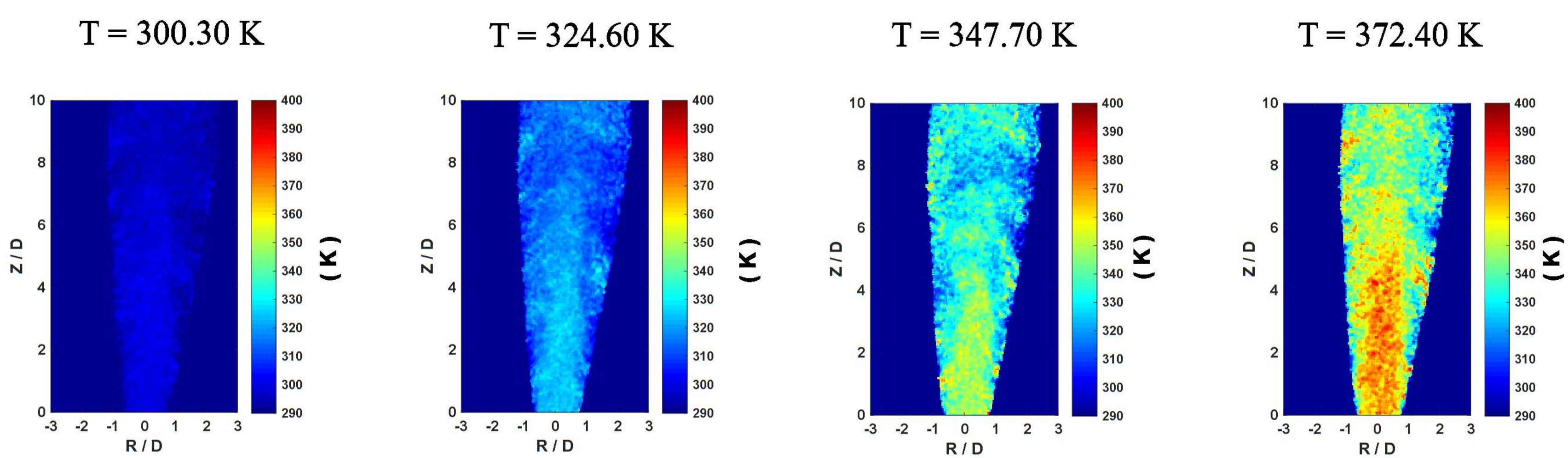

Figure 5.12. Temperature distributions of PLIF free jet tests at Re = 10,000

A dimensionless temperature, θ, is defined (Equation 5.22) to maintain the consistency in comparing the results of the PLIF free jet cases. The reference temperatures (room temperatures) for this calculation are provided from thermocouple data; the jet and nozzle outlet temperatures are directly extracted from the PLIF results. The dimensionless temperature, θ, varies between the range of zero and one. The θ equal to zero means that the jet temperature is equal to the reference temperature, and the θ equal to one means that the jet temperature is equal to the jet temperature at the nozzle exit. When the turbulent flow exits the nozzle, a mixing occurs between the jet core and ambient flow. The dimensionless temperature illustrates the extent of the mixing between the jet core and the ambient flow. For the areas with θ equal to one, there is no mixing effect and jet is maintaining the nozzle exit temperature. The mixing effect is at its highest for areas with θ equal to zero when jet reaches the room temperature.

$$\theta = \frac{T_{Jet} - T_{ref}}{T_{Outlet} - T_{ref}} \tag{5.22}$$

Detailed dimensionless temperature distributions for cases with $\mathrm{Re} = 10,000$ are presented in Figure 5.13. The evidence of turbulent flow structure and jet shear layer eddies are observed at the edge of the free jet. The free jet at $\mathrm{Re} = 10,000$ is considered as a fully turbulent flow, and can consist of eddies of different sizes. The eddy structures are results of instabilities within free flow due to the existence of turbulence. The structure of the turbulent flow for the free jet and its energy cascade are shown in Figure 5.14. The energy cascade, in continuum mechanics, is the energy transferred from larger eddies to smaller eddies. The larger eddies are unstable and transfer their energy to the smaller ones.

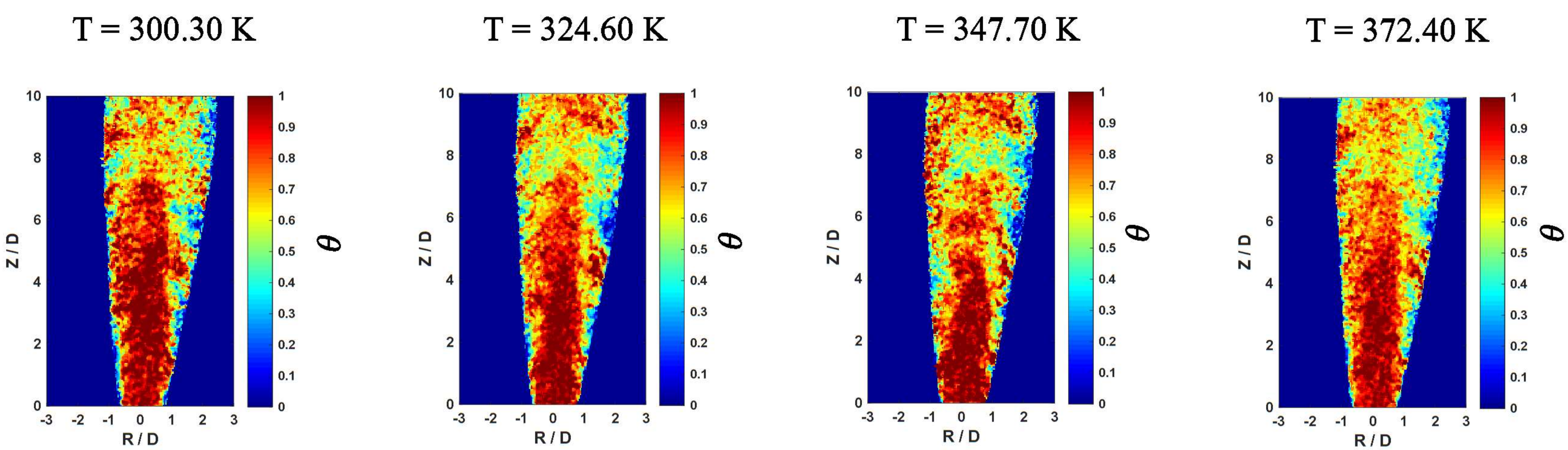

Figure 5.13. Dimensionless temperature distributions of PLIF free jet tests at Re = 10,000

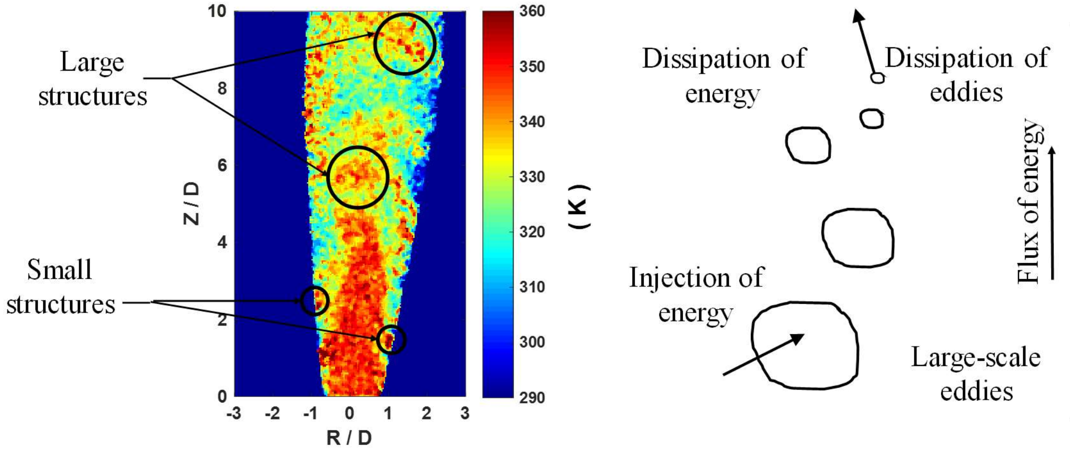

Figure 5.14. Free jet energy cascade

This processes repeats in a sequence between eddies with different sizes. The turbulent kinetic energy of smaller eddies converts into heat; thus, some hotspots are observed downstream of the jet. Furthermore, Figure 5.13 provides information about the jet core region. The jets retain the nozzle exit temperature in their potential cores. Moreover, the potential cores remain intact until approximately the same distance from the jet outlet $(Z / D \approx 5)$ for all four cases, which is expected to be observed for cases with the same Reynolds number. For the momentum potential cores, it is expected to observe the uniform velocity until approximately seven diameters downstream from the jet outlet [5, 11]. Available experimental investigations on free jets mostly focused on the velocity distribution.

There are very few experimental studies on temperature distributions within free jets, using direct methods, such as hot wire and thermocouples. These methods provide temperature information at locations that probes are instrumented. Thus, the available methods are not able to provide a detailed temperature distribution through the jet.

Therefore, for this study, analytical solutions are used to check the validity of the PLIF application on free jet tests.

Integrating Equation 5.18, and applying Equations 5.17 and 5.19, an expression is obtained for the dimensionless temperature as Equation 5.23,

$$\frac{T_c - T_\infty}{T_0 - T_\infty} \cong 5.65 \frac{D_0}{x} \tag{5.23}$$

Using Equation 5.23, it is expected that the thermal core remains intact until approximately 5.65 diameters downstream from the nozzle exit [50]. The thermal potential cores observed from PLIF tests only for cases with Re = 10,000 agree with the theoretical solutions. The theoretical solution does not capture the impact of Reynolds number on the potential core length. As it will be shown later in this chapter, the length of potential core increases as the Reynolds number increases.

Reynolds Number Influence on the Jet Core

The Reynolds number has the most influence on the free jet development [55]. In this study, the impact of increasing the jet Reynolds number is investigated. Figure 5.15 presents the detailed distribution of the temperature and dimensionless temperature at T $\approx$ 325 K for three different Reynolds numbers of jets. As shown in Figure 5.15, an increase in the Reynolds number leads to an increase in the length of the jet potential core zone. The Reynolds number is a dimensionless flow parameter that is a function of the flow velocity, nozzle inner diameter, and kinematic viscosity. For this study, the flow velocity is the only factor that is increased to provide the higher Reynolds number. The jets with a lower velocity (lower momentum) start exchanging the energy of the jet with the surrounding flow at a distance closer to the nozzle exit; thus, jets with lower Reynolds numbers have a shorter potential core. The impact of the Reynolds number depends on the jet regions. As is seen in Figure 5.15, the effect of the Reynolds number is more significant in the shear layer region where larger spread of momentum exists. The impact of the turbulent flow structure at the edge of the jet increases with increasing Reynolds number. The eddies are mostly formed at the interface of two fluids due to the turbulent instabilities. Increasing the Reynolds number leads to an increase of the formation of eddies, which is also seen in Figure 5.15. For jets with the Reynolds number equal to 5,000, the shear layer vortices disappear at approximately one diameter downstream of the jet nozzle exit. Clearly, at higher Reynolds number the jet shear layer vortices exist at a further distance downstream.

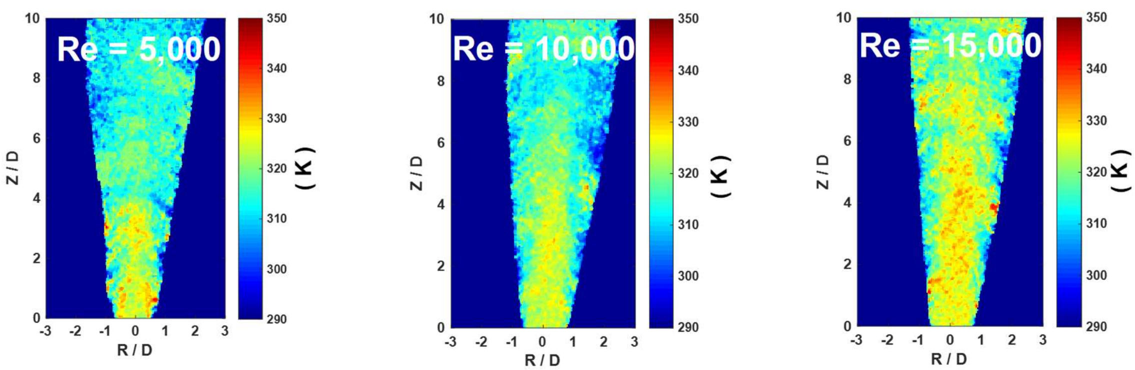

(a)

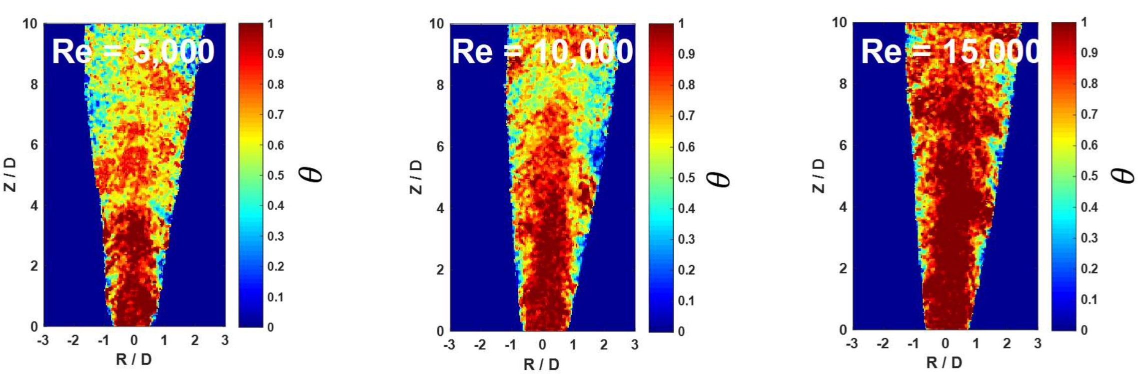

(b)

Figure 5.15. Effect of Reynolds number on free jet core development (T ≈ 325 K), a. Detailed temperature distribution, b. Detailed dimensionless temperature distribution

Figure 5.15 also shows mixing layer development within free jets. Mixing layers are created between two flows with different velocities. For this study, turbulent jets spread into ambient flow with zero velocity. Figure 5.15 shows that mixing layers are formed near the nozzle exit lip, and grow toward the end of jet core. The dimensionless temperature distribution in Figure 5.15 provides a better visualization between jets at different Reynolds number. As is seen, the angle of spread of the mixing layer is the same for all Reynolds numbers.

Figures 5.16 shows the impact of the jet Reynolds number on the radial, dimensionless temperature distribution. Data is categorized based on four distances from the jet nozzles; one, three, five, and seven diameters. As was mentioned earlier, the dimensionless parameter shows the impact of mixing. In general, the dependency of the mixing on Reynolds number is more significant at locations greater than three diameters downstream of the nozzle exit. The mixing is reduced as the jet moves toward the downstream. This reduction is more significant with the Reynold number of 5,000. As the Reynolds number increases, less reduction is observed at greater distances. This can be related to the higher kinetic energy that eddies are carrying within flows with higher Reynolds number.

The results are categorized based on Reynolds numbers in Figure 5.17. For distances greater than three diameters, increasing the Reynolds number leads to an increase in the mixing effect, no significant impact is observed for data at a distance equal to one diameter. The reason behind this phenomenon corresponds to the conversion of turbulent energy to internal energy by viscous dissipation. Figure 5.17 shows that at distances less than one diameter from the nozzle exit, no injection of energy from eddies has occurred.

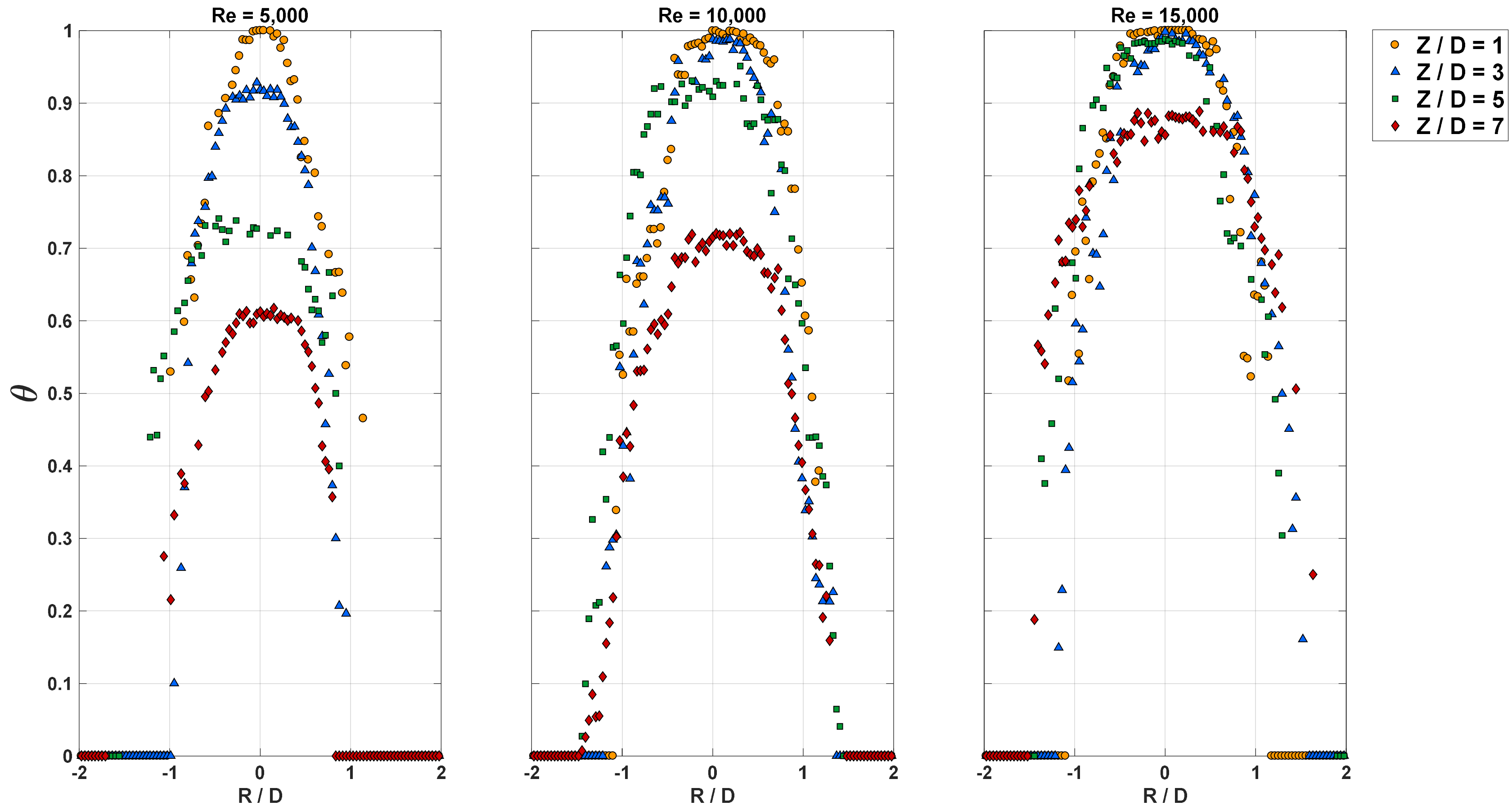

5.16. Radial dimensionless temperature distribution (T ≈325 K), effect of Reynolds number

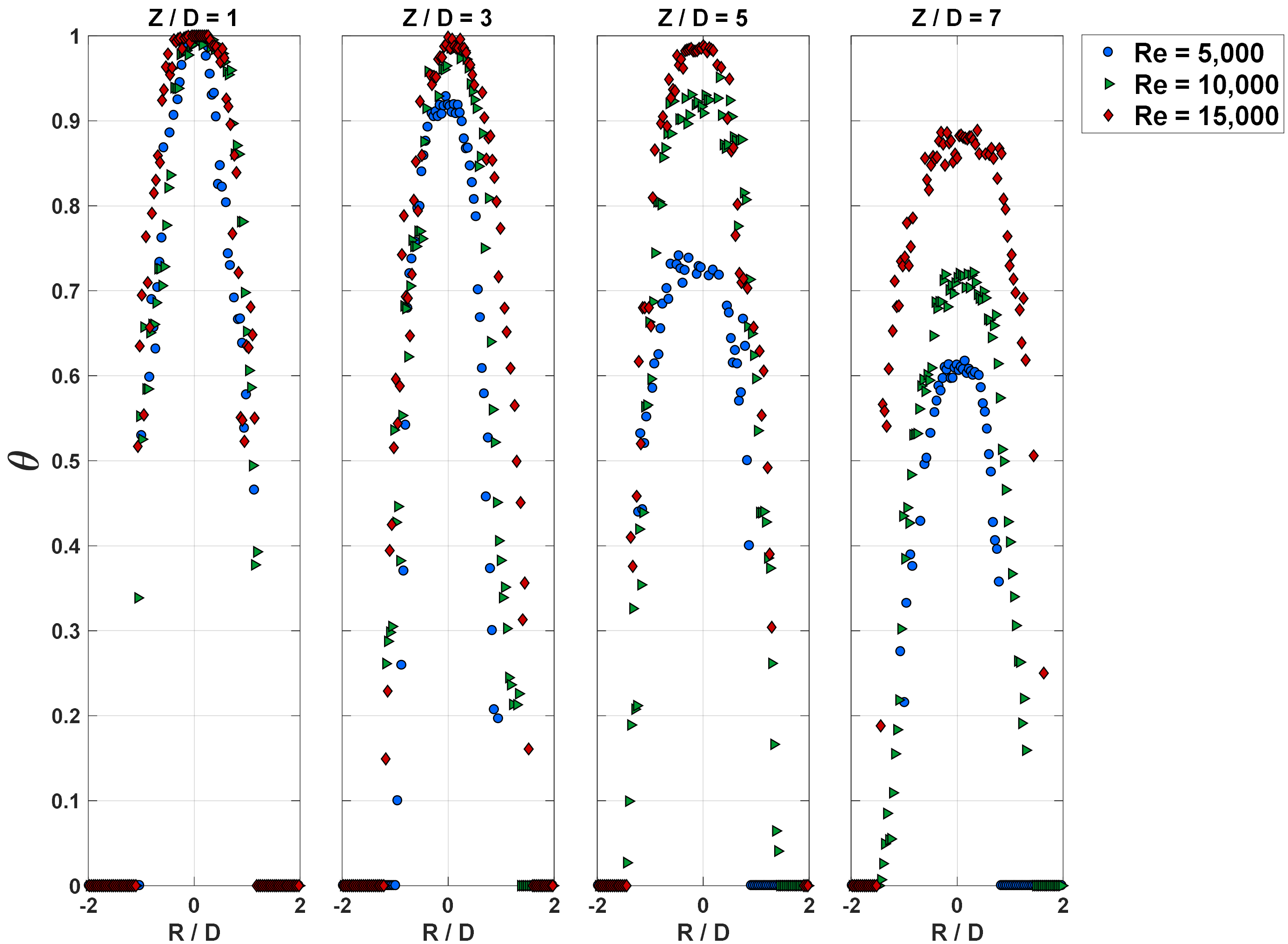

5.17. Radial dimensionless temperature distribution (T ≈325 K), effect of jet downstream location

Comparison of PLIF Results and Theoretical Solutions

As was mentioned earlier in this chapter, the temperature distribution of free turbulent flows can be written as Equation 5.19 [50]. The variables for this equation are modified to match the variables that are used in this study. For this study, the reference temperature is equal to the room temperature, and R and Z are the lateral and streamwise coordinates, respectively. The expression for θ is then

$$\theta = \frac{T - T_{Ref}}{T_{Outlet} - T_{Ref}} = \frac{1}{2}\left[1 + erf\left(\sigma \frac{R}{Z}\right)\right]^{\Pr_t} \tag{5.24}$$

Figure 5.18 offers a comparison between the PLIF results and the theoretical solution. The PLIF data and analytical solution are in a close agreement. Though, overall, the PLIF results have a flat profile near the center of the jet.

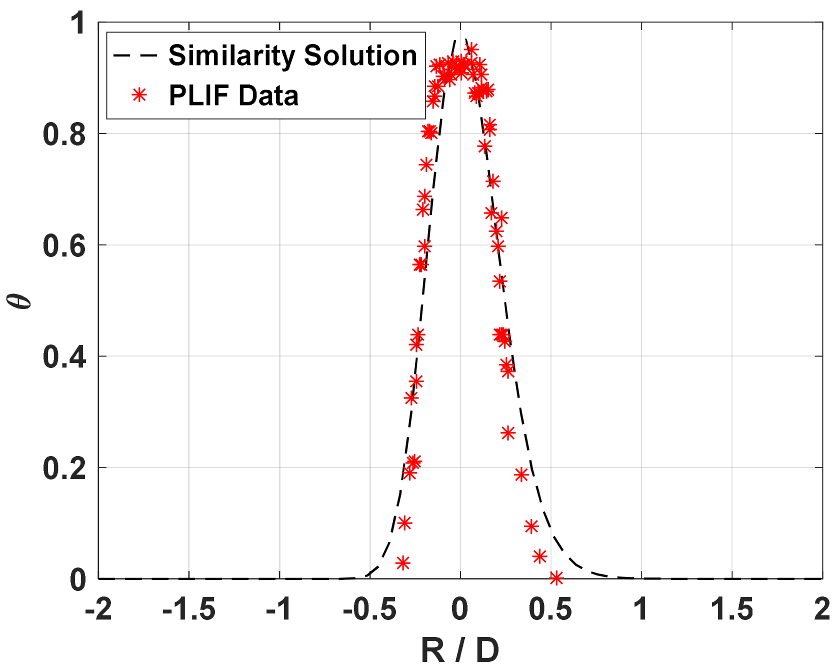

Figure 5.18. Comparison of theoretical data and PLIF results, T = 324.6 K and Re =15,000 at Z / D = 7)

As was mentioned earlier in this chapter, several assumptions have made to solve the governing equations analytically. As an example, considering $\Pr_t = 1$ to make an analogy between the dimensionless temperature and velocity. Also, theoretical solutions are not able to capture the effect of eddies and instability at different regions of the jet. The theoretical solutions are more accurate for fully developed regions. As is shown in Figure 5.2, flat profile is observed within the potential core. As jets move away from the potential core and start to develop, the flat shaped profile converts to a bell shape profile. Fully developed regions for a turbulent jet are located at $Z/D > 15$. For this study, maximum streamwise distance is equal to 0.127m $(Z / D = 10)$. Thus, the PLIF data captures only potential core and developing zones.

In this chapter, an application of PLIF method on free round turbulent jets was presented. The main purpose of this investigation is to validate the PLIF method. The PLIF technique was applied to several cases of jets at different temperatures and Reynolds numbers. A comparison between the PLIF results and theoretical data was performed. A relatively close agreement was observed between the experimental and theoretical data. The PLIF results on free jets show that this method is capable of providing a detailed temperature distribution within gaseous flow as well as insight towards flow structure.

CHAPTER SIX

PLIF Validation Using Flat Plate Jet Impingement

In the previous chapter, the results of PLIF applied to turbulent free jets were presented. In this chapter, the PLIF method is applied to a single turbulent impinging jet on a surface with a uniform heat flux boundary condition. To start, a general history of impinging jets is provided. Next, the development of an experimental arrangement for a flat plate jet impingement and the experimental results are outlined. Lastly, the PLIF method is validated against regionally averaged heat transfer coefficients using traditional heat transfer calculations.

Jet Impingement Background

Jet impingement is a configuration of jets in which a coolant air stream is forced out of a hole or slot and impinges on a hot surface known as a target surface. A schematic of the flow structure of a single round or slot shaped gas jet is illustrated in Figure 6.1. An impinging jet consists of three regions: free jet, stagnation, and wall jet. In the free jet region, the flow is unaffected by the target surface. The momentum exchanged between the jet and its surroundings creates an area known as the potential core, where the velocity profile is preserved uniformly.

The potential core begins to shrink after the jet exit, due to the development of a shear layer around the jet and the loss of momentum to the surroundings (Figure 6.1.b). The potential core entirely disappears about six to seven jet diameters from the orifice exit, and the jet then becomes fully developed [9]. In the stagnation region, as the jet nears the target surface, the structure of the jet changes due to the influence of the surface. The flow velocity decreases in the normal direction because of presence of the wall (Figure 6.1a). Very thin boundary layers are developed on the surface which relatively improve heat transfer through the stagnation region.

The heat transfer rate varies based on the nozzle shape, jet Reynolds number, and jet-to-target plate spacing. In the wall jet region, the horizontal accelerating flow converts to a decelerating flow due to the momentum exchange between the flow and surroundings. With increasing distance from the center, as the boundary layer grows thicker along the wall, generally the heat transfer decreases away from the stagnation point. The Nusselt number has its highest value at the center of the jet and its value decreases outward from the stagnation point.

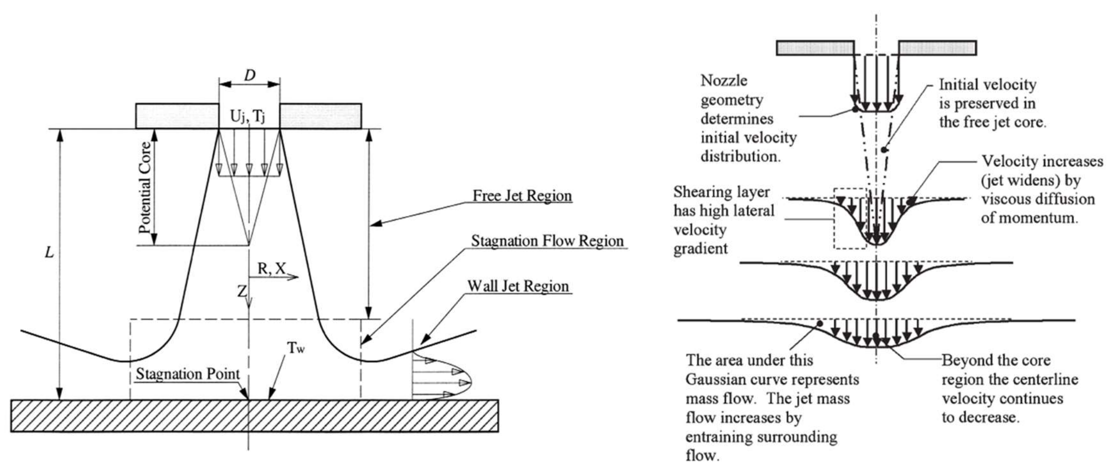

Figure 6.1. a. Impingement jet structure [5], b. Free jet core [10]

Multiple impinging jets are used in a variety of heat transfer applications to obtain a uniform high heat transfer [61]. Each jet, after impingement, is deflected by the cross flow coming from the upstream jet. At the same time, interaction of adjacent jets creates a secondary stagnation region in addition to the regions describe previously.

The regional heat transfer coefficient is defined as Equation 6.1, where q_s is the surface heat flux, q_{loss} is the heat loss, T_s is the surface temperature, and T_{jet} is the jet temperature. The regional heat transfer coefficient can be express as a dimensionless parameter, Nusselt number, as shown in Equation 6.2. The Nusselt number presents the ratio of convective heat transfer to conductive heat transfer across the boundary between two fluids. In laminar flow, the heat transfer from convection and conduction are of similar magnitude, so the Nusselt number is close to unity. The Nusselt number increases with more active convection. Generally, the Nusselt number values in turbulent flow are in the range of 100-1000.

$$h = \frac{q_s - q_{loss}}{T_s - T_{jet}} \tag{6.1}$$

$$Nu = \frac{hD}{k_f} \tag{6.2}$$

Jet flows are complex to study because they can be impacted by a variety of factors such as nozzle geometry, flow velocity (Reynolds number), and jet-to-target plate spacing. Ashforth-Frost et al. [62] studied the impact of nozzle geometry and confinement on the potential core length of turbulent jets. It was observed that potential core length was longer for jets with a fully developed jet exit profile.

Comprehensive studies [63-65] have been performed on an impinging jet to investigate the impact of different test parameters on the heat transfer distribution. Goldstein et al. [66] presented the impact of jet-to-target plate spacing (H / D) on stagnation point heat transfer. It was shown that for jet-to-target plate spacing smaller than the length of the potential core, the stagnation Nusselt number is relatively low. As the spacing increases, the Nusselt number also increases and reaches it maximum at H / D = 8. This heat transfer improvement is due to diffusion of the turbulence from the shear layer at the edge to the centerline of the jet. Lee et al. [67] offered a similar investigation on the stagnation point heat transfer; the maximum Nusselt number was observed for H / D = 6. The only difference between the two studies corresponded to the potential core length. In a separate study, Ashforth-Frost et al. [68] stated that the length of potential core impacts the heat transfer rate; it was shown that the Nusselt number reaches its maximum value at a jet-to-target spacing approximately 110% of the potential core length. At this location, the turbulence intensity overcomes the velocity loss, and leads to an increase in heat transfer.

The jet-to-target surface spacing also impacts the radial heat transfer distribution. Several studies have been performed on single impinging jets with a relativity large jet-to-target plate spacing (4 < H / D < 58) [69, 70]. In a study by Mohanty and Tawfek [71], the heat transfer peak is observed at the stagnation point and it declines exponentially as radial distance increases for R / D < 0.5. Baughn et al. [72], Huang et al. [73], and Goldtein et al. [66] reported a secondary peak for the heat transfer coefficient. As the jet travels further from the stagnation point, the heat transfer rate reduces due to an increase in the laminar boundary layer thickness. As jets enter the fully turbulent wall region, the heat transfer rate increases, and therefore, a secondary peak is observed [74, 75].

The Nusselt number distribution of a relatively small jet-to-target spacing (H / D = 2) is compared to a large one (H / D = 6) by Goldstein and Timmers [76] using constant heat flux at the target surface. It was shown that for the same Reynolds number, the Nusselt number is higher for larger spacing. The flow within the potential core experiences lower turbulence; as the spacing increases, the shear layer mixing diffuses into the jet, and thus the heat transfer is enhanced.

Goldstein et al. [66] studied the jet-to-target surface spacing and Reynolds number in the range of 2 to 10 and 60,000 to 124,000, respectively. In general, it was shown that the heat transfer coefficient is higher at the stagnation point. However, a secondary peak was found based on the jet-to-target spacing and Reynolds number. It was seen that a secondary peak occurs at two diameters from the stagnation point. It was shown that the jet-to-target surface spacing of eight has the highest heat transfer coefficient.

Empirical correlations were developed by Golestein et al. [77] to estimate the heat transfer coefficient for single impinging jets. The correlations express the Nusselt number as a function of Reynolds number and jet-to-target surface spacing for two types of boundary conditions at the target surface: constant temperature and constant heat flux (Equations 6.3 and 6.4). These correlations develop a linear relationship between the Nusselt number and jet-to-target surface spacing. Also, the Nusselt number increases with an increase in jet Reynolds number. According to these correlations, Goldstein et al. stated that jet-to-target surface spacing of 7.75 provides the maximum average heat transfer coefficient.

$$\frac{\overline{Nu}}{\mathrm{Re}^{0.76}} = \frac{24 - \left|\frac{H}{D} - 7.75\right|}{533 + 44\left(\frac{R}{D}\right)^{1.394}} \quad \text{constant surface temperature} \tag{6.3}$$

$$\frac{\overline{Nu}}{\mathrm{Re}^{0.76}} = \frac{24 - \left|\frac{H}{D} - 7.75\right|}{533 + 44\left(\frac{R}{D}\right)^{1.285}} \quad \text{constant surface heat flux} \tag{6.4}$$

Experimentation Facility

Jet Impingement Configuration

A steady-state flat plate jet impingement facility is used for this investigation. Figure 6.2 illustrates a sketch of the PLIF jet impingement test section. The jet impingement setup consists of three main components: the plenum, jet plate, and target plate. The plenum and the jet plate are made from polycarbonate plastic with a length and width of 0.1778 m, and a thickness of 0.0127 m. A 0.1524 m × 0 .1524 m perforated plate is placed in the middle of the plenum. The plenum provides uniform coolant flow (room temperature) to the jet plate through which the coolant flow moves to impinge on the hot target surface. A single round hole with a diameter of 0.0127 m is placed in the middle of the jet plate. Two standard T- type thermocouples are placed in the plenum near the jet exit to record the coolant flow temperature. The target plate surface consists of 81 aluminum plates, measuring 0.0127 m × 0.0127 m. The heater is placed in the support base and covered with a thin layer of high thermally conductive filled silicone paste (OMEGATHERM 201). This layer provides a great means of conducting heat from the heater to the aluminum plates. A standard T-type thermocouple is imbedded at the back center of each aluminum plate using a high thermally conductive, two component adhesive (OMEGABOND 101 resin and catalyst).

Four threaded rods and hex nuts are used to connect the target plate to the plenum. Loosening the nuts and sliding the target plate up and down changes the jet-to-target spacing in the range of two to ten. Experimental tests are performed for impinging jets with Reynolds numbers of 5,000, 10,000, and 15,000. A variable transformer is used to regulate the voltage to the heater and achieve the desirable power for the heater. The temperatures of the aluminum plates are monitored and recorded. The temperatures are used to calculate the steady state local Nusselt number. The Nusselt numbers from PLIF results are compared with the traditional results from the thermocouples.

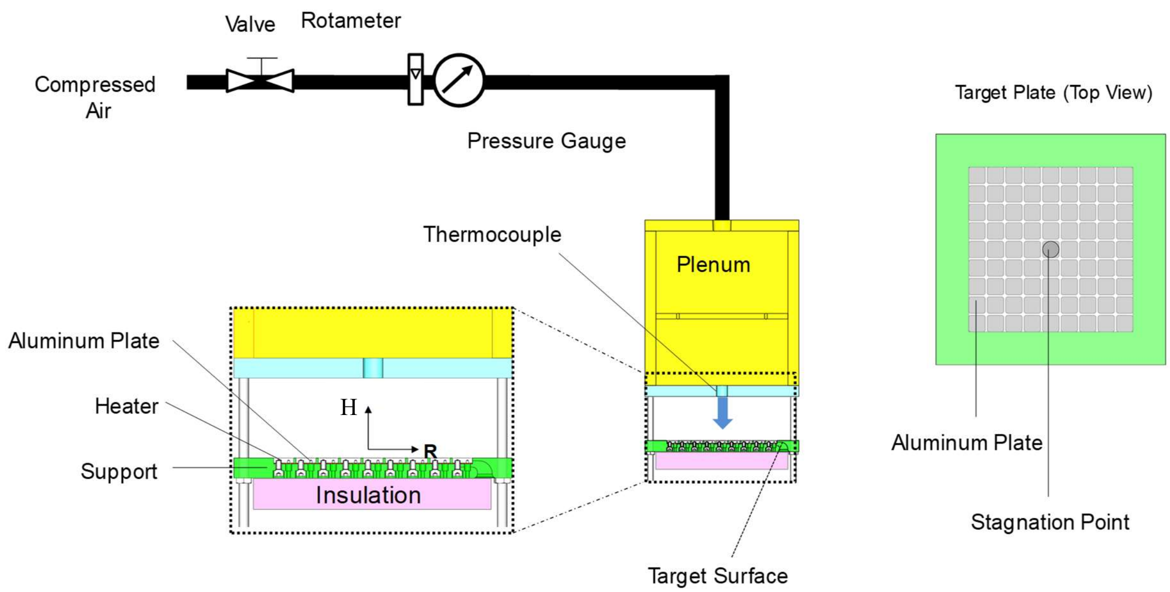

Figure 6.2. Sketch of the jet impingement section

Validation of the Jet Impingement Setup

The heat transfer from the heated surface is first validated with the correlation (Equation 6.4) developed by Goldstein et al. [77]. When the heated target surface reaches steady state (constant temperature at each aluminum plate), the fluid and solid temperatures and power to the heater are recorded. Heat transfer coefficients are found using the Newton's law of cooling using Equation 6.1.

A heat loss calibration is performed for all experimental cases to obtain the net surface heat flux convected to the air. To calculate the heat loss, the gap between the jet plate and target surface is filled with a low conductivity material to prevent the heat transfer by convection. The target surface is insulated to maximize the resistance to heat transfer within the supporting material. The surface is heated to two temperatures: low and high temperatures. These temperatures are the lowest and highest temperature that are observed in the actual impinging tests for all cases. The aluminum plate temperatures and jet temperature at the nozzle are measured using thermocouples. There is no flow in the system; therefore, the power of the heater that is used to reach the surface temperature is approximately equal to the heat loss. Using linear interpolation [78] between the temperatures and powers applied to the heater, the heat loss can be found for each impingement test. The heat loss varies between 8.95% and 10.84% for this study.

The Nusselt number is calculated at different locations using Equation 6.2, and compared with the values from the Goldstein correlation (Figure 6.3). As was discussed in the history of the impinging jet, Goldstein et al. [66] estimated that the maximum Nusselt number occurs at H / D = 8; however, for this study, the maximum Nusselt number is observed at H / D = 6. Goldstein et al. [66] developed the correlations for turbulent jets at relatively higher Reynolds numbers (60,000 - 124,000) in comparison to this study (5,000 - 15,000). It was offered by Ashforth-Frost et al. [68] that there is a relation between the potential core length, jet-to-target surface spacing, and the maximum Nusselt number measured on the target surface. The Reynolds number impacts the length of the potential core and that may explain the reason behind observing the maximum Nusselt number at a different H / D in comparison with Goldstein et al. It was reported by Ashforth-Frost that the maximum Nusselt number occurs at 110% of the potential core length from the jet exit. The Goldstein et al. correlations provide an estimate for the Nusselt number; however, there are other factors such as potential core length that impact the Nusselt number.

A difference is observed in data obtained for cases with H / D = 4 in comparison with the Goldstein correlation. The results from this study show that cases with H / D = 4 have the higher Nusselt number after cases with H / D = 6. However, the Goldstein correlation shows that cases with H / D = 4 has the lowest Nusselt number. As was mentioned earlier, Goldstein et al. performed the tests at much higher Reynolds number in comparison with the Reynolds numbers used in this study. Reynolds number impacts the potential core length and that may explain the reason behind the observed discrepancy.

The theory of propagation is used to calculate the uncertainty of the steady state experiments. Using Equation 6.2, the uncertainty of the Nusselt number can be written as:

$$\Delta Nu = \sqrt{\left(\frac{\partial Nu}{\partial h}.\Delta h\right)^2 + \left(\frac{\partial Nu}{\partial D}.\Delta D\right)^2 + \left(\frac{\partial Nu}{\partial k}.\Delta k\right)^2} \tag{6.5}$$

The diameter of the nozzle is constant and it is assumed that there is no change in the thermal conductivity of the jet. The uncertainty of the Nusselt number due to measured net heat flux, surface temperature, and flow temperature can be written as Equation 6.6.

$$\Delta h = \sqrt{\left(\frac{\partial h}{\partial q_{net}} \Delta q_{net}\right)^2 + \left(\frac{\partial h}{\partial T_s} \Delta T_s\right)^2 + \left(\frac{\partial h}{\partial T_j} \Delta T_{jet}\right)^2} \tag{6.6}$$

Evaluating the partial derivatives in the Equation 6.6. gives:

$$\Delta Nu = \frac{D}{k} \sqrt{\left(\frac{\Delta q_{net}}{T_s - T_j}\right)^2 + \left(-\frac{q_{net} \Delta T_s}{\left(T_s - T_j\right)^2}\right)^2 + \left(\frac{q_{net} \Delta T_{jet}}{\left(T_s - T_j\right)^2}\right)^2} \tag{6.7}$$

The uncertainty is calculated for all cases using Equation 6.7. The maximum uncertainty among all tests was observed for the case with H / D = 6 at the stagnation point, and is equal to 2.86. The proportion of uncertainty corresponding to the net heat flux, surface, and flow temperature measurement are 47.1%, 27.8%, and 25.1%, respectively.

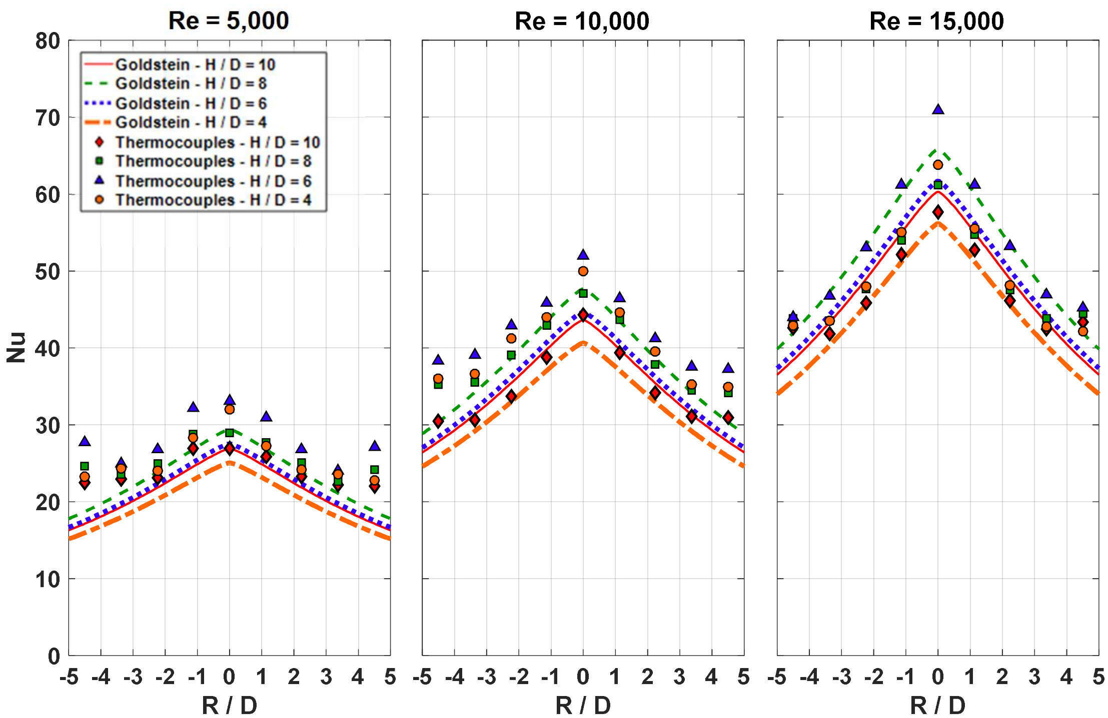

Figure 6.3. Regionally averaged Nusselt number distribution

PLIF Experimental Procedure and Data Reduction

The PLIF experimental procedure for the impinging jet tests is very similar to the free jet experiments. A schematic figure of the PLIF setup is presented in Figure 6.4. The main difference between the procedures is the presence of a hot surface plate. The data collection for this study consists of three main image recording steps: background images, reference images, and air/toluene images at different experimental conditions. For each step two sets of 500 images are recorded: temperature dependent (using red filter) and temperature independent (using blue filter). Background images are captured while the laser is on and there is only airflow in the system. Reference images are taken while the mixture of air and toluene flows into the system at room temperature (297 K), and the laser is on. For the reference images, the target surface is not heated. The jet for all test cases is at room temperature. After the target surface reaches the steady state condition (constant temperature at each aluminum plate), the toluene is introduced to the flow line from the seeding system. It is important to monitor the total flowrate to maintain the same Reynolds number. The air / toluene images are recorded while the laser in on. Davis 8.3 software from LaVision is used to record the raw images. For each step, flow and ambient temperatures, aluminum plate temperatures, and flowrate are monitored and recorded. Images are exported from Davis in the tagged image file (TIF) format then post processed using an in-house MATLAB code (Appendix A). The maximum area available with the current imaging system is equal to ten-by-six jet diameters. Having the jet at the center of the frame provides a maximum length of three jet diameters of the wall jet region. In order to capture a larger length, the camera is repositioned to view an area further from the center of the jet, and each test is repeated.

The post processing includes the following steps: background subtraction, time averaging, two color thermometry, and normalizing the fluorescence intensity $\left(I/I_{ref}\right)$. The image processing for the jet impingement data is identical to the free jet data reduction (Chapter Five). The results of post processing for the case with jet Reynolds number of 10,000 and H / D = 10 are presented in the Figures 6.5 - 6.7.

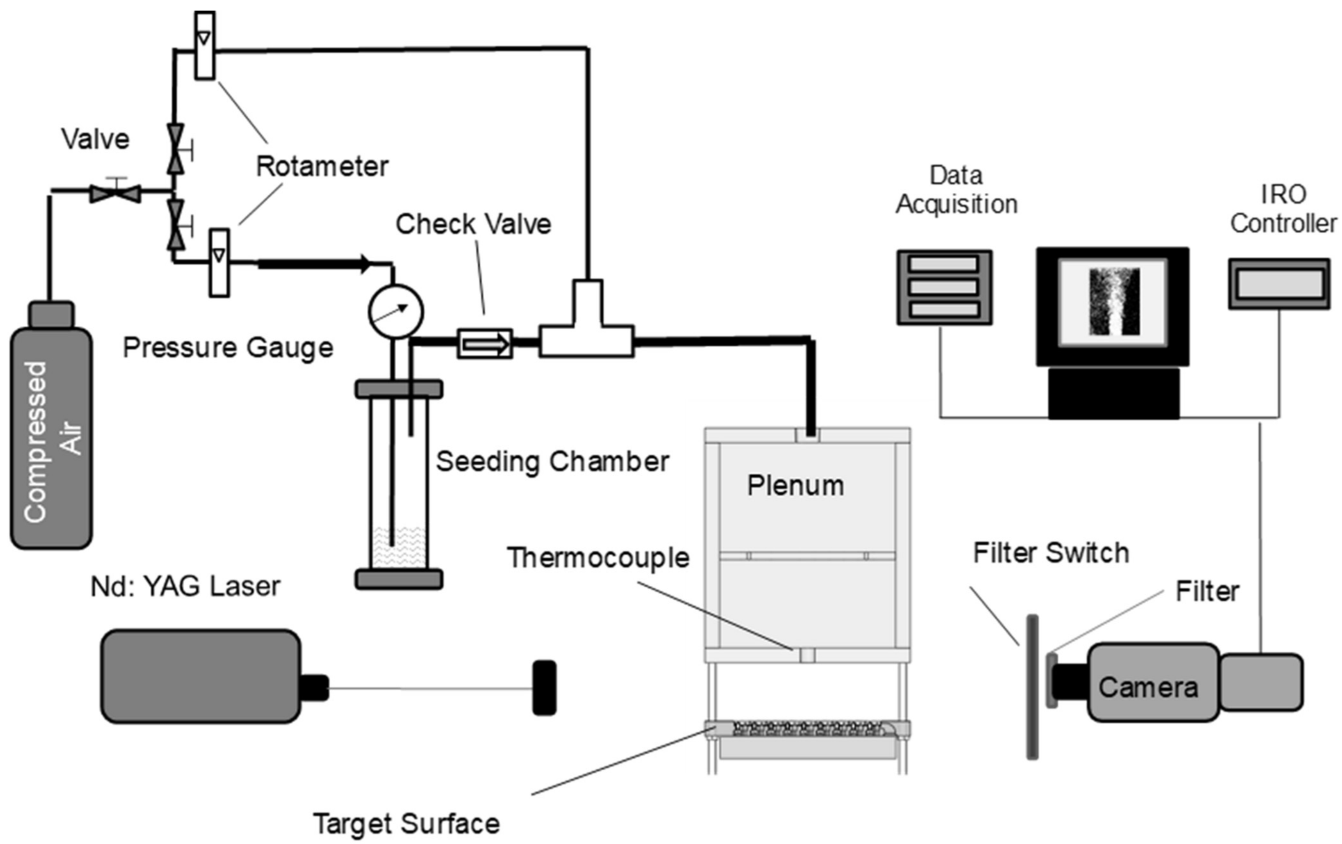

Figure 6.4. PLIF experimental setup for jet impingement

PLIF Impinging Jet Results

To validate the PLIF method, single free jets and flat plate jet impingement are investigated. The results of the free jets were presented in the previous chapter. In this chapter, the application of the PLIF technique on 12 cases of jet impingement for validation purposes is outlined

Effect of Jet Reynolds Number

Detailed temperature distributions for impinging jet tests are shown in Figures 6.8- 6.11. The three flow regions: free jet, stagnation, and wall jet, are distinguishable. The turbulent flow structures, shear layer formation, are more visible at the edge of the jets. Thus, higher mixing is expected to be observed at the edge. The PLIF results illustrate the impact of this mixing at the edge of the jets. The results for all cases show that the potential core region is unaffected by the radial growth of the shear layer. As the jet moves toward the target surface, in the downstream locations, the shear layer grows because of the instability of eddies. The momentum energy of the shear layer is converted to heat at the edge of the jets which is seen in the results.

A very thin boundary layer is formed in the stagnation zone. For the Reynolds numbers used in this study, the stagnation boundary layer remains laminar. However, turbulence in the impinging jet disturbs this thin boundary layer. Thus, the heat transfer is increased significantly. As the Reynolds number increases, the turbulence in the impinging jet also increases, and therefore, more disruption occurs within the boundary layer. As can be seen in the figures, the temperature gradient increases near the stagnation region with an increase in jet Reynolds number. This effect of heat transfer transition is also observed at the wall jet region.

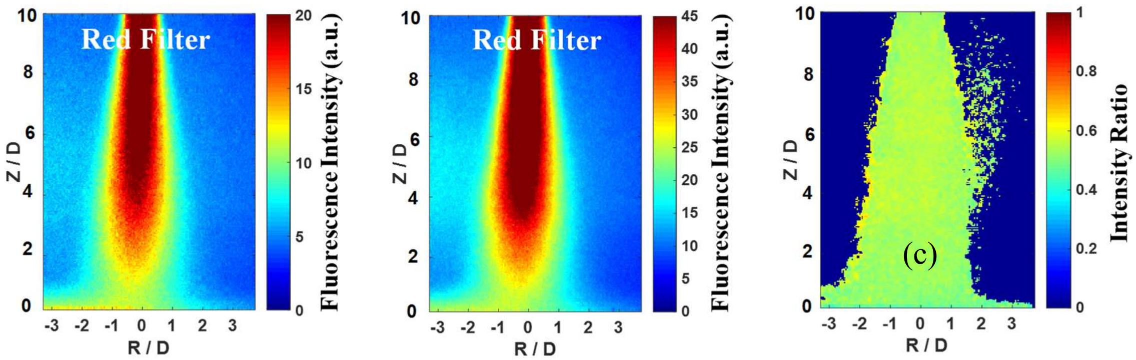

Figure 6.5. Impingement results for the cold target surface (reference images) for Re = 10,000, H / D = 10, a. Background subtracted, time averaged temperature dependent, b. Background subtracted, time averaged temperature independent, c. Two color thermometry, intensity ratio

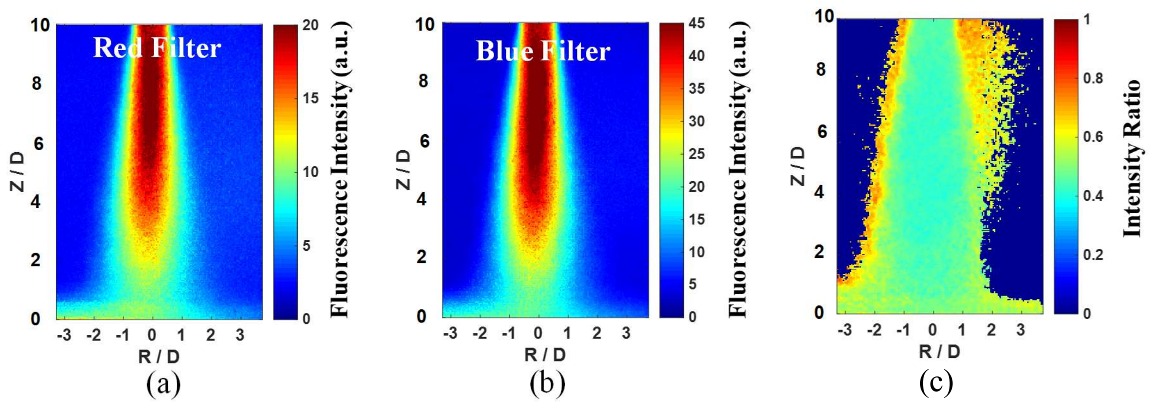

Figure 6.6. Impingement results for target surface with constant heat flux boundary for Re = 10,000, H / D = 10, a. Background subtracted, time averaged temperature dependent, b. Background subtracted, time averaged temperature independent, c. Two color thermometry, intensity ratio

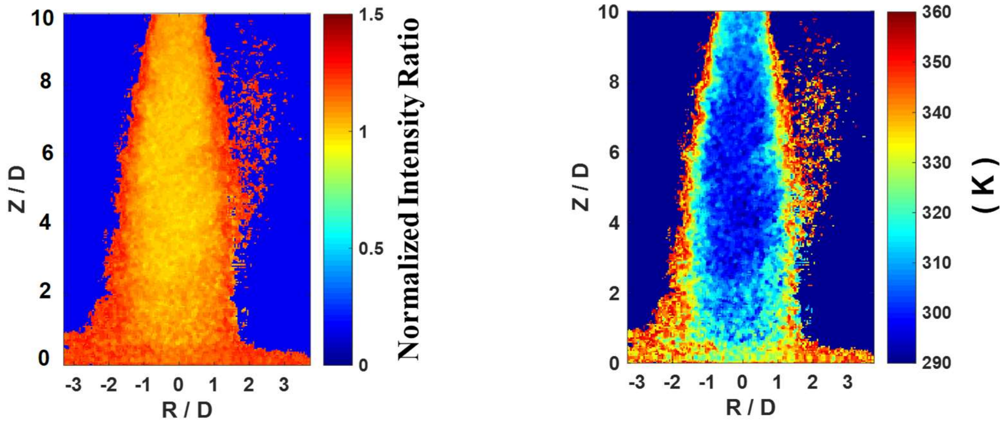

(a) (b)

Figure 6.7. Impinging results for cold target surface for Re = 10,000, H / D = 10, a. Normalized intensity ratio, b. Temperature distribution

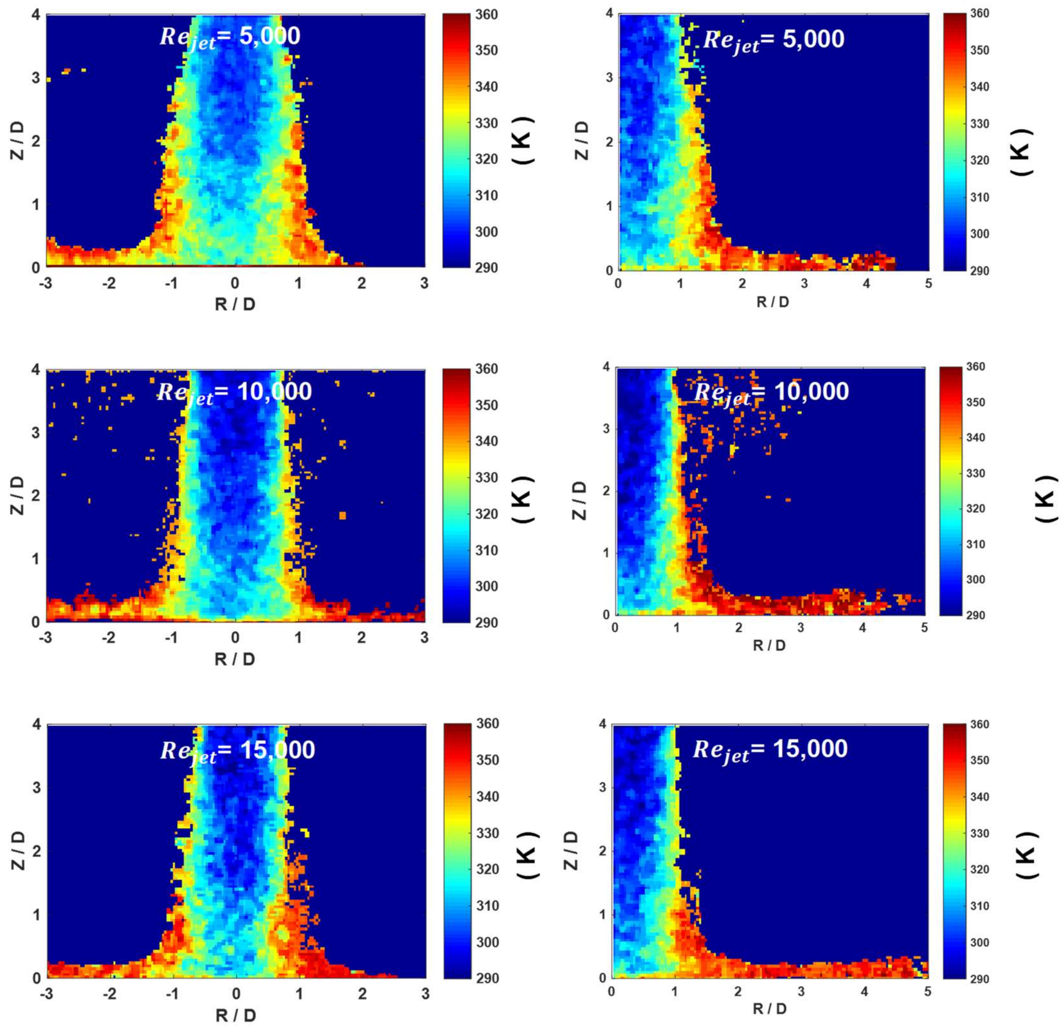

Figure 6.8. Temperature distribution for jet impingement cases with H / D = 4

As an example, it is seen in Figure 6.8 that there is no significant temperature gradient within the wall jet region for Re = 5,000. As the Reynolds number increases, a higher temperature gradient is observed within the region. This happens because at a lower Reynolds number, the mixing impact is lower, and the jet loses its effectiveness as it covers the target surface in the wall jet region. As the jet Reynolds number increases, the instability within that region increases. Therefore, the jet retains its cooling effectiveness through this region.

For cases with greater jet-to-target surface spacing (Figures 6.10 and 6.11), for a lower Reynolds number, a thicker boundary layer is observed. As the Reynolds number increases, the boundary layer gets thinner. Flow separation is observed for cases with H / D = 10 as fluid travels towards the wall jet region (in the radial direction). As an example, in Figure 6.11, for impinging jet with Re = 15,000 and H / D = 10, flow slips on the surface at R / D approximately equal to three. The impact of this separation increases as the Reynolds number increases. This may be related to the reduction of the kinetic energy transportation within the boundary layer in the wall jet region. As kinetic energy transportation reduces, the potential energy increases, and therefore, the fluid pressure increases. The increase in pressure may slow the fluid on the surface or even cause revered flow. More study on flow momentum is required to achieve a better understanding of the flow separation that is observed.

To have a consistent comparison between data, a dimensionless temperature, η, is defined as Equation 6.8. The dimensionless temperature is used to compare the effect of jet Reynolds number and jet-to-target plate spacing among the PLIF experimental cases.

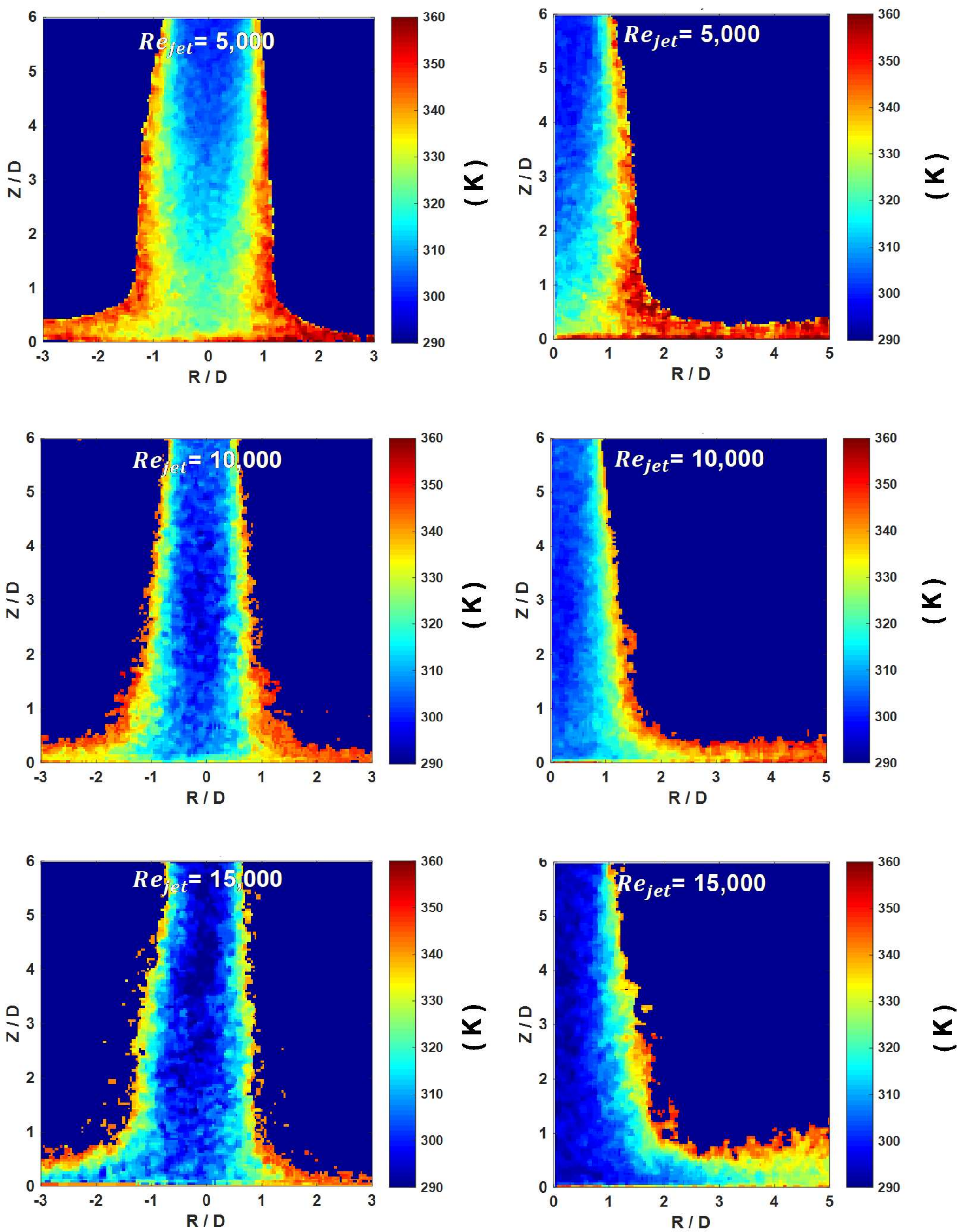

Figure 6.9. Temperature distribution for jet impingement cases with H / D = 6

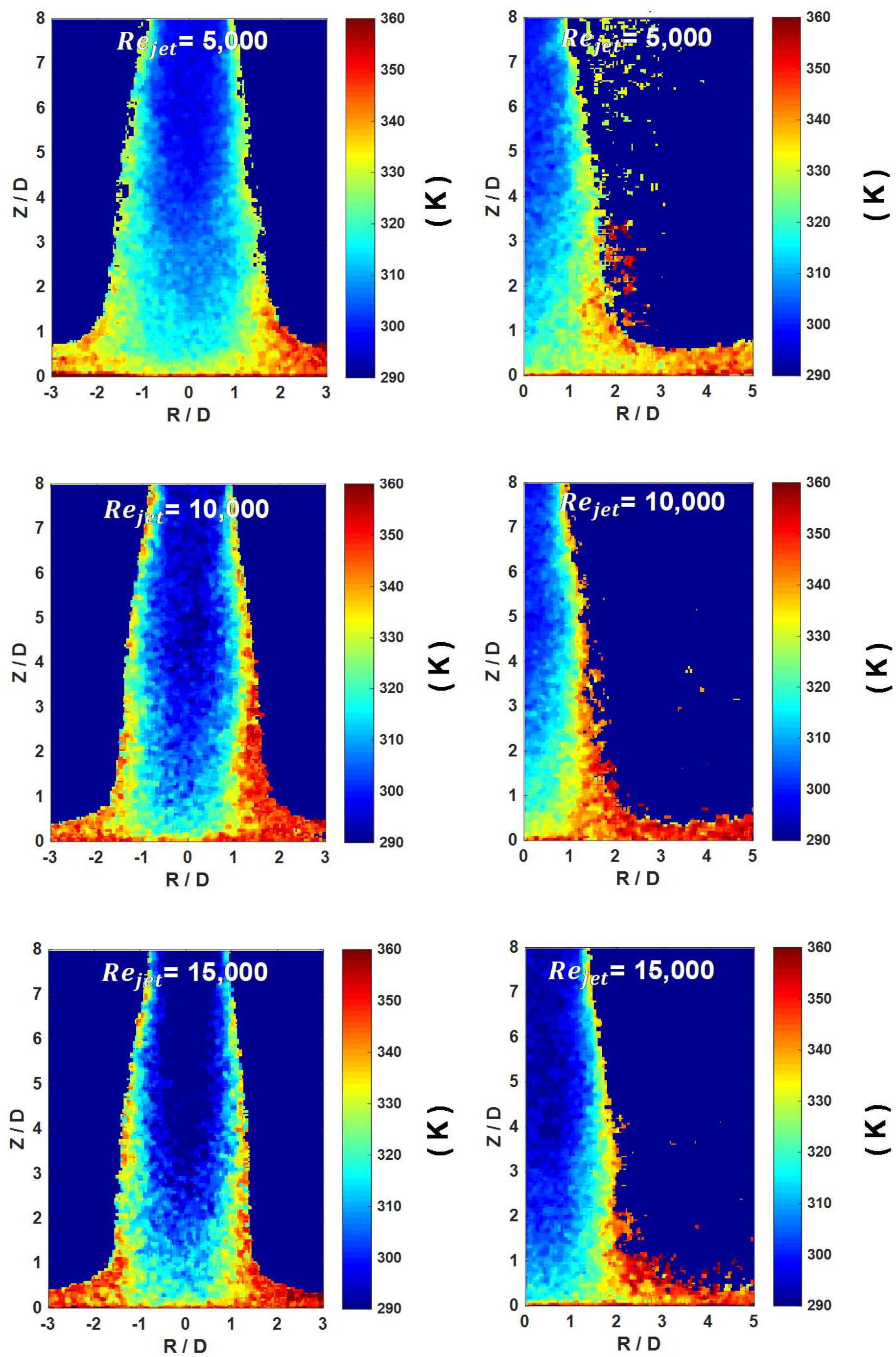

Figure 6.10. Temperature distribution for jet impingement cases with H / D = 8

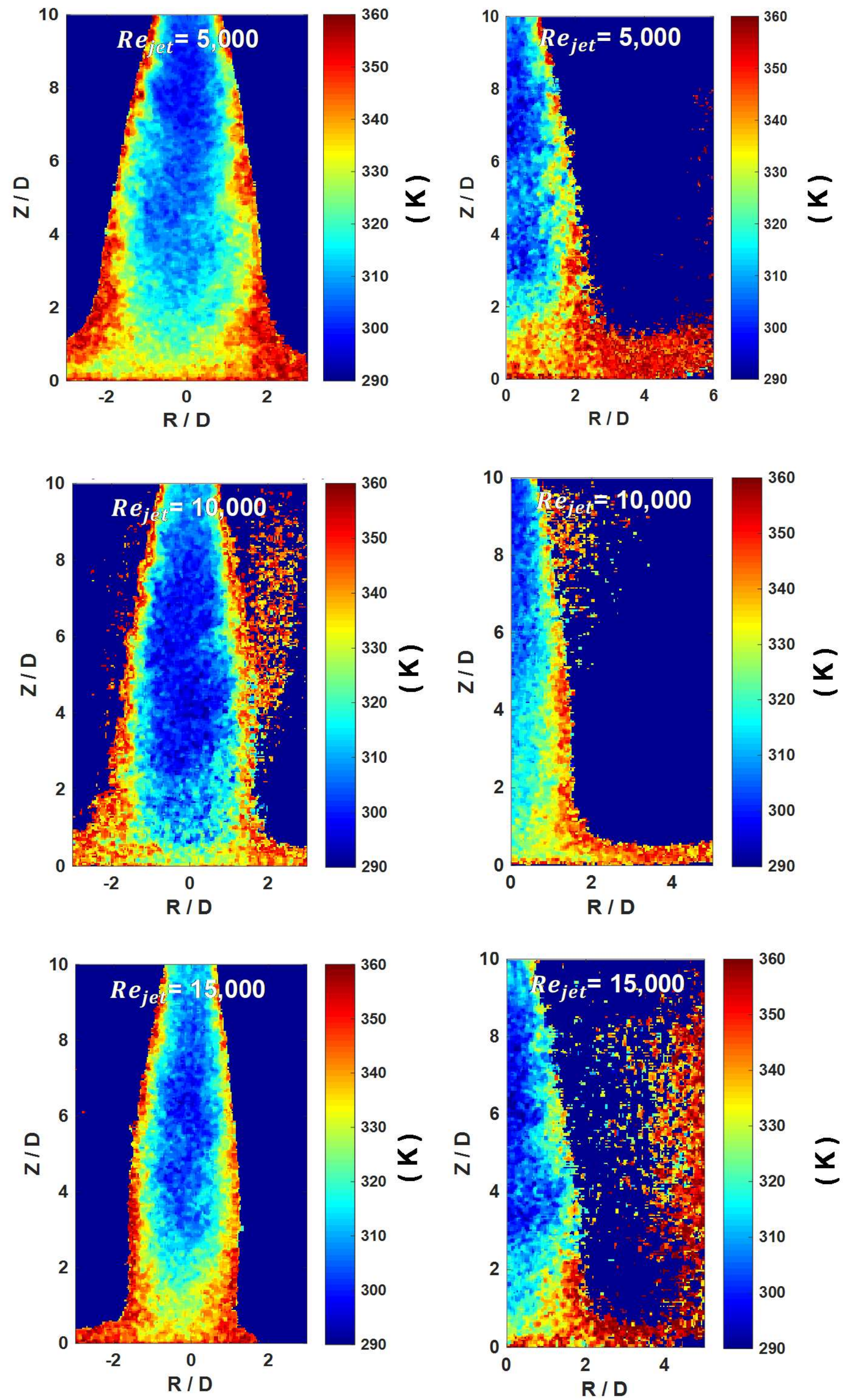

Figure 6.11. Temperature distribution for jet impingement cases with H / D = 10

The wall and ambient temperatures come from thermocouple data, and jet temperature is extracted from the PLIF data. The dimensionless temperature varies in the range of zero to one. For η equal to zero, the jet temperature is equal to the ambient temperature, as the value of η increases, the jet temperature gets closer to the surface temperature; $\eta = 1$ means that the jet temperature is equal to the wall temperature at a specific radial location.

$$\eta = \frac{T_{jet} - T_{\infty}}{T_{Wall} - T_{\infty}} \tag{6.8}$$

The dimensionless temperature presents the effectiveness of the impinging jet for cooling the plate. The dimensionless temperatures are calculated for cases using Equation 6.8. The radial, dimensionless temperature distribution at the stagnation point (R / D = 0) for all cases are presented in Figure 6.12. As it is seen, for Re = 5,000, the jet effectiveness is similar for cases with H / D = 4, 6, and 8. As the Reynolds number increases, the dependency of the jet effectiveness on the jet-to-target spacing increases. For all cases, the maximum jet effectiveness at the stagnation point is observed for cases with a jet-to-target spacing of 6 and the minimum is observed for cases with a jet-to-target spacing of 10.

To study the Reynolds number dependency, the results of the dimensionless temperature are categorized for the three Reynolds numbers at each jet-to-target surface spacings in Figure 6.13. Comparing the results indicates that the effectiveness at the stagnation point is relatively independent of the Reynolds number, however; a dependency on jet-to-target surface spacing is observed.

Thermal boundary layer dependency on the jet Reynolds number and jet-to-target surface spacing is seen through PLIF results. The thermal boundary layer is defined as the distance from a target surface where the temperature is equal to 99% of the ambient temperature. According to Equation 6.8, the thermal boundary layer can be measured when η is approximately equal to zero. Figure 6.14 presents the dimensionless temperature for cases with a jet-to-target surface spacing of 10, at different radial locations. It can be seen that the thickness of the boundary layer increases as the jet travels away from the stagnation point. It is expected to observe a decrease in the heat transfer rate, and as a result, a decrease in the temperature gradient. It is observed that the temperature gradient decreases as the distance from the stagnation point increases. The dimensionless temperatures for cases with different jet-to-target surface spacings are illustrated in Figures 6.15 - 6.16. It is seen that a thicker boundary layer is observed for a lower Reynolds number. The jet with the lower Reynolds number (Re = 5,000), creates a laminar boundary layer, and the transition between laminar to turbulent occurred at a larger radial location in comparison to the jets with a higher Reynold number. This impact is more significant for jets with a higher jet-to-target surface plate with a lower Reynolds number. As the jet leaves the nozzle and reaches the jet wall region, it loses its momentum, and as a result, a laminar boundary layer is created. For cases with a higher Reynolds number, the jet maintains a higher velocity, and the boundary layer transitions from laminar to turbulence closer to the stagnation point.

Thermal Boundary Layer Measurement Using PLIF

The single jet impingement setup is used to validate the novel PLIF technique. Previously in this chapter, results of PLIF for different cases were presented.

In this section, local Nusselt numbers are calculated, and compared with the results from thermocouples. First, the local heat transfer coefficients are obtained from combining Fourier's and Newton's laws as expressed in Equation 6.9.

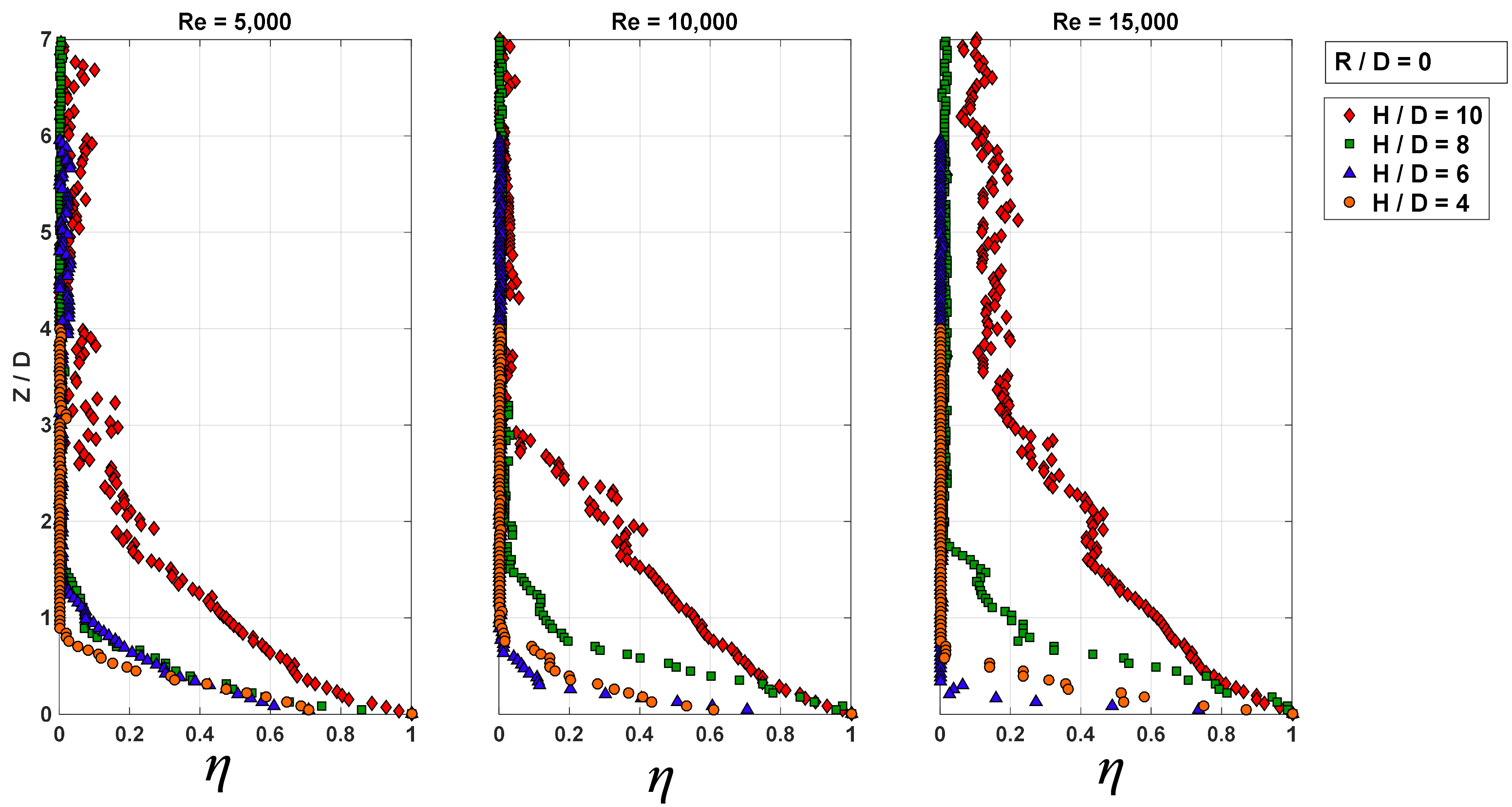

Figure 6.12. Dimensionless temperature distribution at the stagnation point, impact of jet-to-target surface spacing

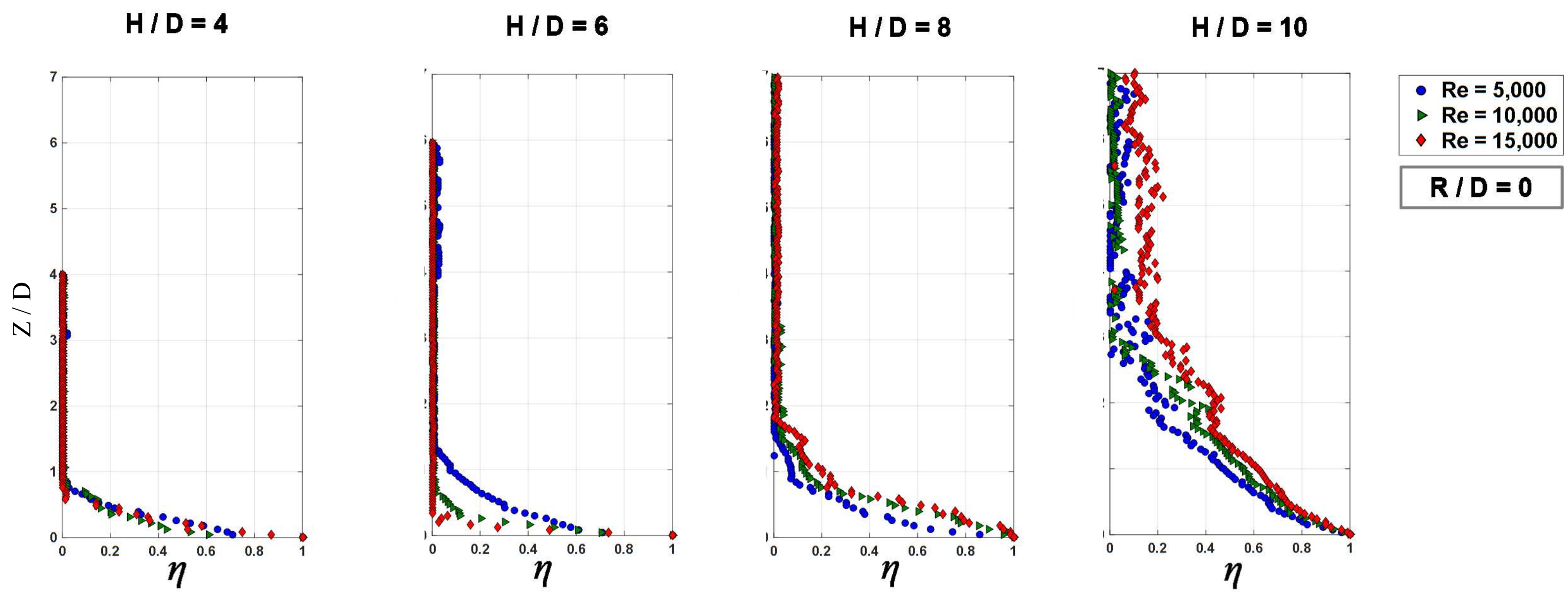

Figure 6.13. Dimensionless temperature distribution at the stagnation point, impact of Reynolds number

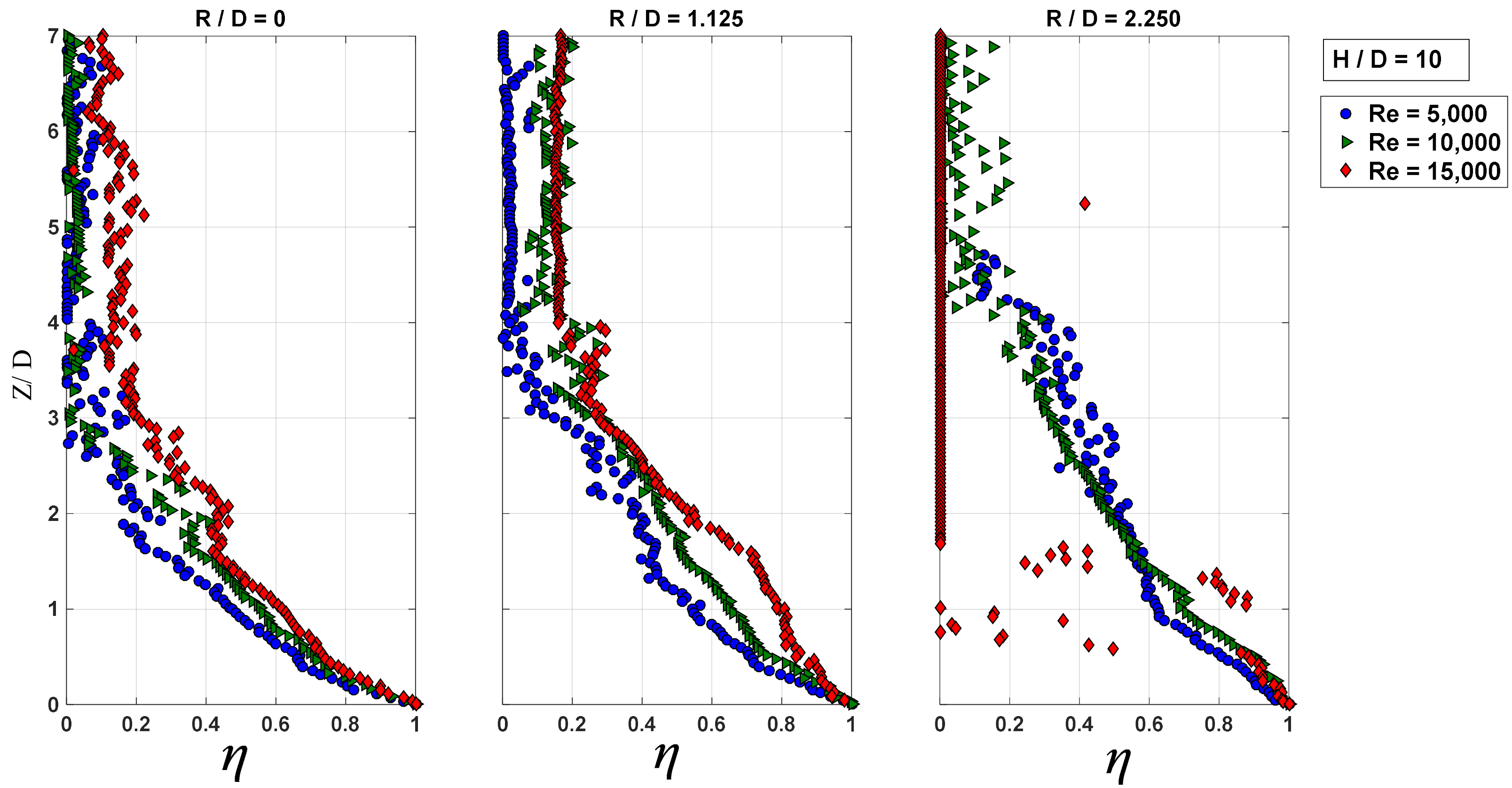

Figure 6.14. Impact of R / D on the boundary layer growth, H / D = 10

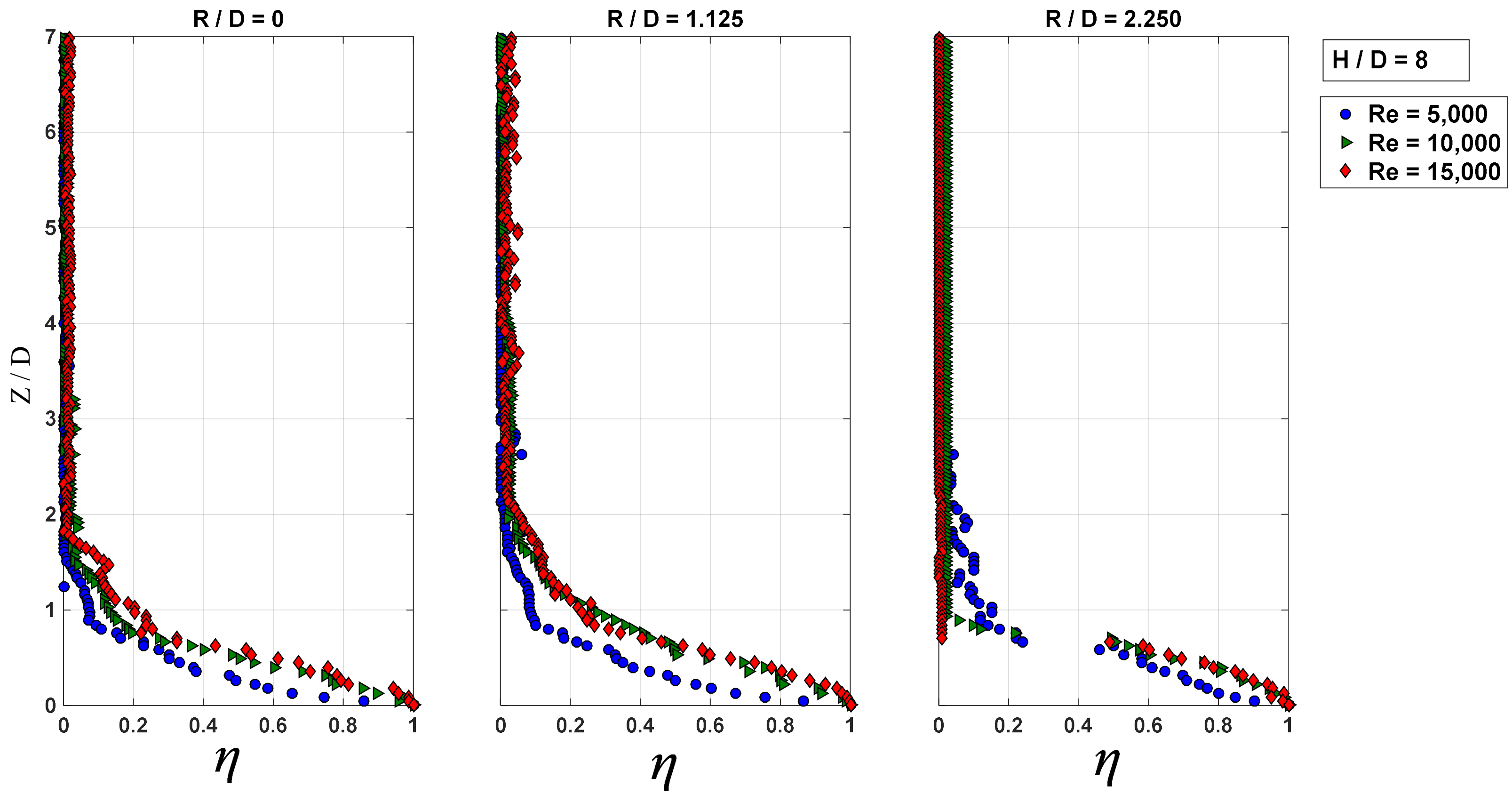

Figure 6.15. Impact of R / D on the boundary layer growth, H / D = 8

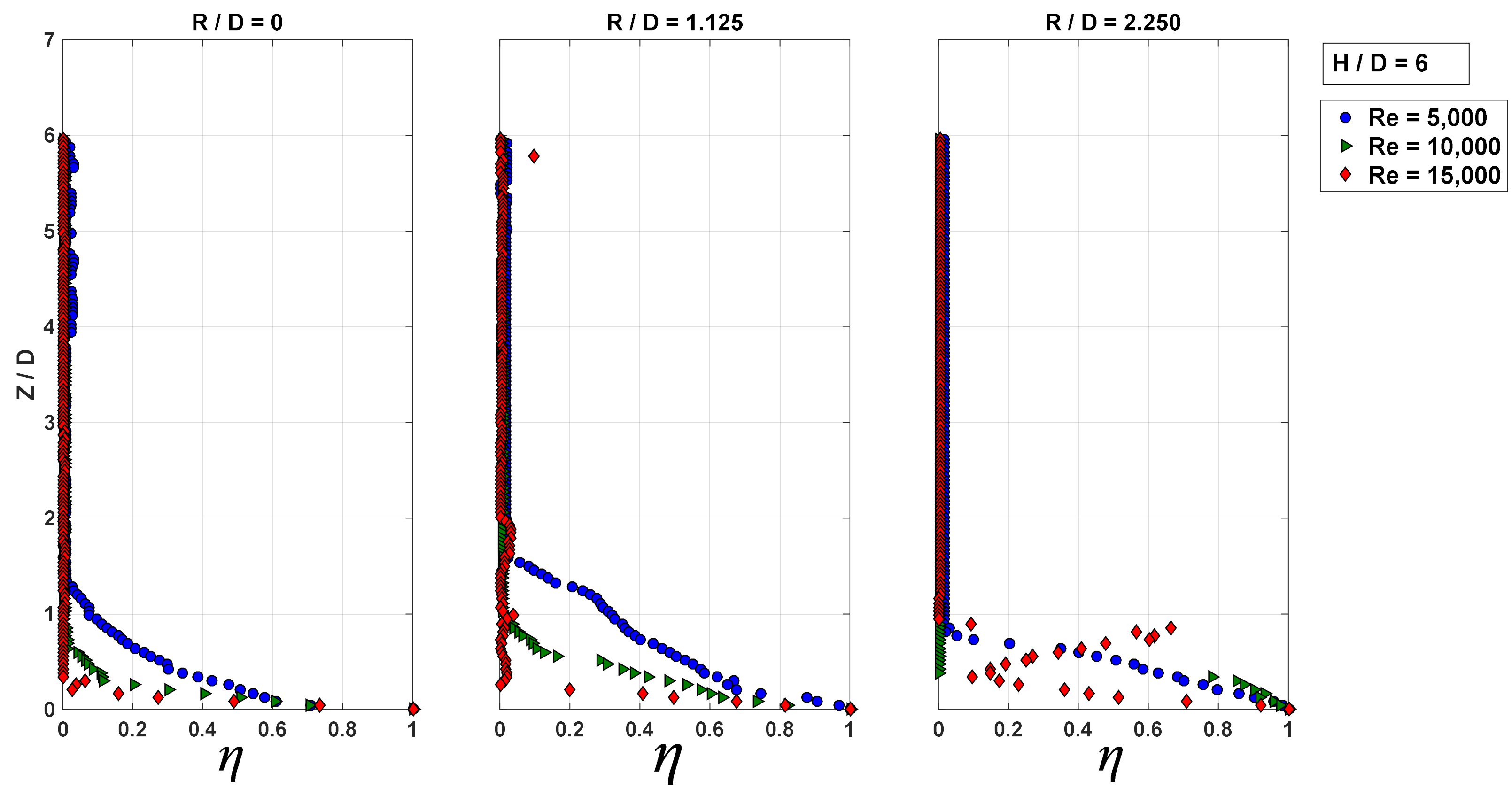

Figure 6.16. Impact of R / D on the boundary layer growth, H / D = 6

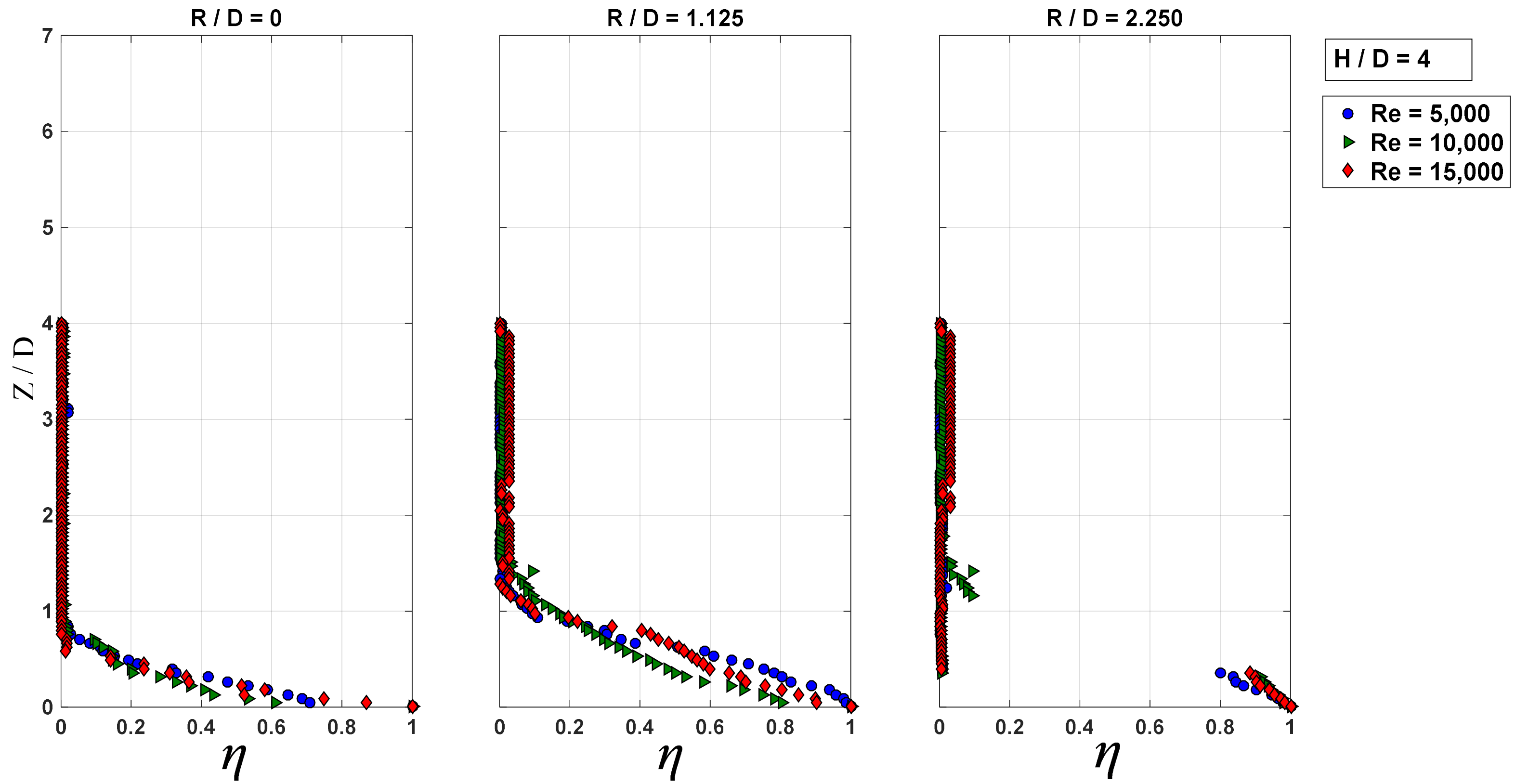

Figure 6.17. Impact of R / D on the boundary layer growth, H / D = 4

$$h = \frac{-k_f \left.\dfrac{\partial T}{\partial Z}\right|_{Z=0}}{\left(T_s - T_{jet}\right)} \tag{6.9}$$

Thermocouples provide the surface temperatures, and the jet temperature is directly extracted from the PLIF results. In order to calculate the numerator of Equation 6.9, relations between temperature and vertical distance from the surface (H) are built at the stagnation point (R / D = 0), R / D = 1.125, and R / D = 2.250. The temperature is extracted from PLIF results and y is the location above the surface. In order to estimate the derivative in the viscous sublayer, the first three pixels above the surface are selected to build the temperature equation as a function of location. Then, $\partial T/\partial Z$ can be obtained at the surface (Z = 0). After the heat transfer coefficient is obtained, the Nusselt number is calculated using Equation 6.2. The procedure for calculating Nusselt number for one case is given in Equations 6.10 - 6.12.

$$T = 177633.35Z + 338.61 \tag{6.10}$$

$$h = \frac{-k_f \dfrac{dT}{dZ}|_{Z=0}}{\left(T_s - T_{jet}\right)} = \frac{-\left[k_f \, {}^{W}\!/_{m.K}\right].\left[-177633.35 \, {}^{K}\!/_{m}\right]}{\left(338.59 - 302.77\right)K} = 4959.05 k_f \left[{}^{W}\!/_{m^2K}\right] \tag{6.11}$$

$$Nu_{PLIF} = \frac{hD}{k_f} = \frac{\left[4959.05 k_f \, {}^{W}\!/_{m^2K}\right].\left[0.0127m\right]}{k_f \, {}^{W}\!/_{m.K}} = 62.98 \tag{6.12}$$

The same procedure was repeated for all cases and compared with the Nusselt numbers calculated using the steady state, traditional heat transfer experiment (Nusselt from thermocouples data). The results of the comparison between the PLIF and thermocouple results are shown in Figure 6.18. The results show that the Nusselt number calculated from combining the Fourier and Newton's law are in a good agreement with the Nusselt number obtained from the traditional method. The maximum error offset ($\left(Nu_{PLIF} - Nu_{traditional}\right) / Nu_{traditional}$) among all cases was is equal to 8.75%.

In this chapter, an application of the PLIF technique on single impingement jets was presented. The PLIF technique was applied to several cases at different Reynolds numbers and jet-to-target surface spacings for validation purposes. The results were compared with the results from thermocouples. Moreover, this method was validated against regionally averaged Nusselt numbers using traditional heat transfer calculations. Results show that PLIF method is capable of resolving a near wall thermal boundary layer. PLIF provides a detailed distribution of the temperature, and provides the opportunity to fully study the structure the thermal field without disturbing the flow. The traditional methods to study the heat transfer with the turbulent flows only provide information in specific locations. The PLIF method also has the potential to visualize the turbulence structure and flow thermal behavior simultaneously. This opens new opportunities to gain better understanding of complex physics, and improve the available correlations that are being used in computational fluid mechanics tools.

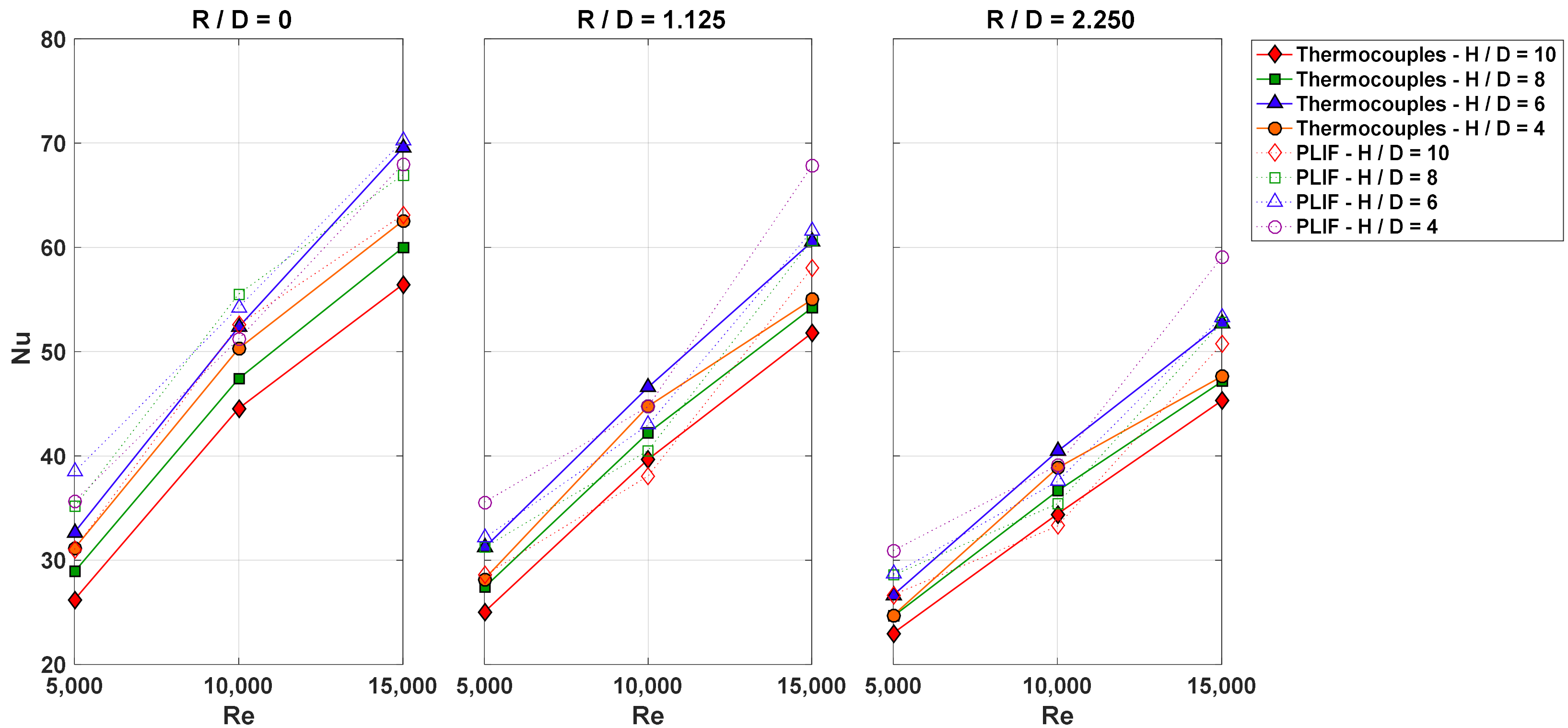

Figure 6.18. Validating PLIF data using a traditional, steady state experiment

CHAPTER SEVEN

Conclusions and Recommendations

Summary of Experimental Investigation

In this chapter a general overview on the development of the PLIF method and its validation are provided. In addition, recommendations for future work are discussed. This novel method was developed to satisfy the need to study thermal flow fields non-intrusively. The PLIF technique is a visualization technique that has detailed quantitative probing capability to measure the temperature gradient without disturbing the flow. Toluene was selected as the tracer because of its outstanding spectroscopy properties and temperature sensitivity. The excitation at 266nm was employed to take advantage of high fluorescence quantum yield and absorption cross section.

The focus of this study was then to develop an empirical relationship between the toluene fluorescence signal and temperature that can be used in quantitative temperature measurement studies. The fluorescence signal is a function of temperature and concentration. To remove the effect of concentration, fluorescence intensities at two regions, temperature sensitive and insensitive, were collected. The ratio of the intensities from these two bands cancelled the effect of the concentration. Thus, the fluorescence intensity ratio is only a function of temperature. A jet cross section is used for this calibration, and a correlation is built between the dimensionless temperature and intensity ratio. A standard deviation analysis was performed on the calibration data using the theory of propagation. The maximum relative standard deviation for this study was approximately 3.73%.

The PLIF technique was applied on free jets and jet impingement to validate the method. For free jet studies, a comparison between PLIF experimental and theoretical data was performed. For impinging jet studies, the results were validated using a traditional heat transfer experiment. The PLIF results on free jets and impinging jets demonstrate that this method is capable of providing a detailed temperature distribution within gaseous flow as well as insight towards flow structure. Also, this method has the capability to resolve a near wall thermal boundary layer which has always been a challenge to fully understand the flow behavior especially in highly turbulent flows. PLIF has the potential to be used in other applications that require the knowledge of fluid temperature gradients. With the application to highly turbulent flows (as seen in gas turbine cooling application), the results could also be used to validate state of the art CFD codes.

Suggested Future Work

In this study, a toluene-based PLIF diagnostic method was successfully developed. With this success, this method can be used on a number of future applications. Future study directions are described in three main categories: usage of a higher purity tracer, improvement of the diagnostic setup, and new flow field applications.

For this study, industrial grade toluene was used as the fluorescing tracer. For future studies, it is recommended to use higher purity toluene. The presence of impurity affects the fluorescence intensity especially at lower temperatures [79]. The impurities may absorb a proportion of the laser energy and impact the toluene fluorescence quality. In this study, applying the two color method and normalizing the results removed the impact of impurities. However, using a higher quality toluene may improve the quality of the fluorescence and make the post processing procedure easier.

The second area of interest is to improve the diagnostic setup. For this study, a single camera is used to capture fluorescence intensities from both filters. Therefore, there was not a possibility to capture intensities simultaneously. For each set of data, images with the blue filter were captured first, then the filter was switched using a filter switch, and red images were collected. In order to remove the impact of the delay, all images were time averaged. Having two cameras, and capturing blue and red images simultaneously, offers the possibility of studying a single image temperature profile and tracking the flow instability and eddy movements over a period of time. It also provides opportunities to apply this method to transient heat transfer problems. Another improvement that can be applied to the diagnostic setup is corresponding to the laser energy. The laser energy plays a crucial role in PLIF experiments. For this study a planar laser sheet is used to excite the tracer particles. It would be beneficial to monitor the laser energy within the plane to provide a uniform energy within the entire flow domain.

Finally, the PLIF method can be applied on different flow field applications. This method can be used to study flow fields that require knowledge of temperature gradients. As an example, PLIF can be used to obtain the temperature distribution within film cooling boundary layers. PLIF is a novel, non-intrusive technique that visualizes the thermal flow field while offering a quantitative insight into convective heat transfer within the flow. PLIF can be used to study the thermal flow field to improve and validate the available theoretical solution of complex flow applications.

PLIF is an innovative optical diagnostic method to visualize the flow structure and measure the flow field temperature quantitatively. PLIF can be applied to turbulent, near wall flows, where traditional methods are not able to measure the temperature gradient. The measurement of fluid temperature and visualizing the flow structure are critical to improve understanding of the fluid flow, especially in those involving complex phenomena. PLIF offers a novel insight to couple the fluid dynamics and heat transfer, which the traditional methods are not capable of offering simultaneously.

APPENDICES

APPENDIX A

MATLAB Code

```
%%%%%%%%%%%%%%%%%%%%%%%%%%%%%%%%%%%%%%%%%%%%%%%%%%%%%%%%%%%%%%%%%%%%%%%
%%%
                %PLIF Post Processing MATLAB Code
% this Matlab script provide a general overview on the post processing
have
%been used for this study.
                               %
                        % By Sara Seitz%
                       % Date 03/15/201
%%%%%%%%%%%%%%%%%%%%%%%%%%%%%%%%%%%%%%%%%%%%%%%%%%%%%%%%%%%%%%%%%%%%%%%
%%%

% clearing and closing all prior data in MATLAB
close all
clear all
clc

%Starting timer
tic
%% Calculater the background average images
% change the directry
cd 'E:\MATLAB Files\PLIF\Calibration\T1\Black_C'
% import one image to obtain the dimension
image= strcat('B00001.tif');
I= imread(image, 'tif' );
Dimension=size(I);
H=Dimension(2);
W=Dimension(1);
X0=1;
Y0=1;
sum=zeros(W,H);
name='B0';
Start=1;
End=500;

% Calculating the average background images for C-filter
for i=Start:End %
        num = sprintf('%04d',i);
  ifile = strcat(name,num,'.tif');
  I = imread(ifile, 'tif' );
   I = I(X0:X0+W-1,Y0:Y0+H-1);
  intensity=double(I);
  sum=sum+intensity;
end
for ii=1:W
    X(ii)=(ii*D);
    for jj=1:H
        Y(jj)=(jj*D);
      black_avg(ii,jj)=sum(ii,jj)/(End-Start+1);
    end
end
% change the directry
cd 'E:\MATLAB Files\PLIF\Calibration\T1\Black_T'
% import one image to obtain the dimension
image= strcat('B00001.tif');
```

```
I= imread(image, 'tif' );
Dimension=size(I);
H=Dimension(2);
W=Dimension(1);
X0=1;
Y0=1;
sum=zeros(W,H);
name='B0';
ofile='Black_T.xlsx';
Start=1;
End=500;
% Calculating the average background images for T-filter
for i=Start:End %
        num = sprintf('%04d',i);
  ifile = strcat(name,num,'.tif');
  I = imread(ifile, 'tif' );
   I = I(X0:X0+W-1,Y0:Y0+H-1);
  intensity=double(I);
  sum=sum+intensity;
end
for ii=1:W
    X(ii)=(ii*D);
    for jj=1:H
        Y(jj)=(jj*D);
      black_avg(ii,jj)=sum(ii,jj)/(End-Start+1);
    end
end
% Calculate the time averaged intensity for C-filter and T-filter
% change the directry
cd 'E:\MATLAB Files\PLIF\Calibration\T1\Filter_C\'

image= strcat('B00001.tif');
I= imread(image, 'tif' );
Dimension=size(I);
H=Dimension(2);
W=Dimension(1);
name='B0';
Start=1;
End=500;
count=zeros(W,H);
sum=zeros(W,H);
avg=zeros(W,H);
for i=Start:End   % matlab read all the images
    num = sprintf('%04d',i);
    ifile = strcat(name,num,'.tif');
    I = imread(ifile, 'tif' );
    I = I(1:W,1:H);
     for ii=1:W
        for jj=1:H
            I_C(ii,jj)=I_C(ii,jj)- black_C(ii,jj);
            if I(ii,jj) > 0
                sum(ii,jj)=sum(ii,jj)+I(ii,jj);
                count(ii,jj)=count(ii,jj)+1; %
            end
        end
    end
```

```
end
for ii=1:W  % use to convert pixel to mm

    for jj=1:H
       if count(ii,jj)0
        avg(ii,jj)=sum(ii,jj)./count(ii,jj);
       else
           avg(ii,jj)=0;
    end
    end
end
% change the directry
cd 'E:\MATLAB Files\PLIF\Calibration\T1\Filter_T\'

image= strcat('B00001.tif');
I= imread(image, 'tif' );
Dimension=size(I);
H=Dimension(2);
W=Dimension(1);
name='B0';
Start=1;
End=500;
count=zeros(W,H);
sum=zeros(W,H);
avg=zeros(W,H);
for i=Start:End   % matlab read all the images
    num = sprintf('%04d',i);
    ifile = strcat(name,num,'.tif');
    I = imread(ifile, 'tif' );
    I = I(1:W,1:H);

    for ii=1:W

        for jj=1:H
            I_T(ii,jj)=I_T(ii,jj)- black_T(ii,jj);
            if I(ii,jj) > 0
                sum(ii,jj)=sum(ii,jj)+I(ii,jj);
                count(ii,jj)=count(ii,jj)+1; %
            end
        end
    end

end
for ii=1:W  % use to convert pixel to mm

    for jj=1:H
       if count(ii,jj)0
        avg(ii,jj)=sum(ii,jj)./count(ii,jj);
       else
           avg(ii,jj)=0;
    end
    end
```

```
end
cd 'E:\MATLAB Files\PLIF\Calibration\T_ref\Black_C_ref'
% import one image to obtain the dimension
image= strcat('B00001.tif');
I= imread(image, 'tif' );
Dimension=size(I);
H=Dimension(2);
W=Dimension(1);
X0=1;
Y0=1;
sum=zeros(W,H);
name='B0';
Start=1;
End=500;

% Calculating the average background images for C-filter
for i=Start:End %
        num = sprintf('%04d',i);
  ifile = strcat(name,num,'.tif');
  I = imread(ifile, 'tif' );
   I = I(X0:X0+W-1,Y0:Y0+H-1);
  intensity=double(I);
  sum_black_avg_C=sum_black_avg_C+intensity;
end
for ii=1:W
    X(ii)=(ii*D);
    for jj=1:H
        Y(jj)=(jj*D);
      black_avg_C(ii,jj)=sum_black_avg_C(ii,jj)/(End-Start+1);
    end
end
% change the directry
cd 'E:\MATLAB Files\PLIF\Calibration\T1_ref\Black_T_ref'
% import one image to obtain the dimension
image= strcat('B00001.tif');
I= imread(image, 'tif' );
Dimension=size(I);
H=Dimension(2);
W=Dimension(1);
X0=1;
Y0=1;
sum=zeros(W,H);
name='B0';
Start=1;
End=500;
% Calculating the average background images for T-filter
for i=Start:End %
        num = sprintf('%04d',i);
  ifile = strcat(name,num,'.tif');
  I = imread(ifile, 'tif' );
   I = I(X0:X0+W-1,Y0:Y0+H-1);
  intensity=double(I);
  sum=sum+intensity;
end
for ii=1:W
    X(ii)=(ii*D);
```

```
    for jj=1:H
        Y(jj)=(jj*D);
      black_avg(ii,jj)=sum(ii,jj)/(End-Start+1);
    end
end
% Calculate the time averaged intensity for C-filter and T-filter
% change the directry
cd 'E:\MATLAB Files\PLIF\Calibration\T_ref\Filter_C_ref\'

image= strcat('B00001.tif');
I= imread(image, 'tif' );
Dimension=size(I);
H=Dimension(2);
W=Dimension(1);
name='B0';
Start=1;
End=500;
count=zeros(W,H);
sum=zeros(W,H);
avg=zeros(W,H);

for i=Start:End   % matlab read all the images
    num = sprintf('%04d',i);
    ifile = strcat(name,num,'.tif');
    I = imread(ifile, 'tif' );
    I = I(1:W,1:H);

    for ii=1:W

        for jj=1:H
            I_C_ref(ii,jj)=I_C_ref(ii,jj)- black_C_ref(ii,jj);
            if I(ii,jj) > 0
                sum_C_ref(ii,jj)=sum_C_ref(ii,jj)+I_C_ref(ii,jj);
                count_C_ref(ii,jj)=count_C_ref(ii,jj)+1; %
            end
        end
    end


end

for ii=1:W  % use to convert pixel to mm

    for jj=1:H
       if count_C_ref(ii,jj)0
        avg_C_ref(ii,jj)=sum_C_ref(ii,jj)./count_C_ref(ii,jj);
       else
           avg_C_ref(ii,jj)=0;
    end
    end
end

% change the directry
cd 'E:\MATLAB Files\PLIF\Calibration\T_ref\Filter_T_ref\'
```

```
image= strcat('B00001.tif');
I= imread(image, 'tif' );
Dimension=size(I);
H=Dimension(2);
W=Dimension(1);
name='B0';
Start=1;
End=500;
count=zeros(W,H);
sum=zeros(W,H);
avg=zeros(W,H);
for i=Start:End   % matlab read all the images
    num = sprintf('%04d',i);
    ifile = strcat(name,num,'.tif');
    I = imread(ifile, 'tif' );
    I = I(1:W,1:H);

    for ii=1:W

        for jj=1:H
            I_T_ref(ii,jj)=I_T_ref(ii,jj)- black_T_ref(ii,jj);
            if I(ii,jj) > 0
                sum_ref_T(ii,jj)=sum_ref_T(ii,jj)+ I_T_ref(ii,jj);
                count_ref_T(ii,jj)=count_ref_T(ii,jj)+1; %
            end
        end
    end


end
for ii=1:W  % use to convert pixel to mm

    for jj=1:H
       if count_ref_T(ii,jj)0
        avg_ref_T(ii,jj)=sum_ref_T(ii,jj)./count(ii,jj);
       else
           avg_ref_T(ii,jj)=0;
    end
    end
end
%% two color method

% calculation the threshold

%reference threshold
Count_Ratio_ref = Count_ref_T ./ Count_ref_C;
Count_Mix_ref = sqrt( Count_ref_T.^2 + Count_ref_C.^2);
Th_ref = median(Count_Mix_ref);

%reference threshold
Count_Ratio = Count_T ./ Count_C;
Count_Mix = sqrt( Count_T.^2 + Count_C.^2);
Th = median(Count_Mix);
```

```
IntensityRatio = T./C;
Norm_T = avg_T./avg_T_ref;
Norm_C = avg_C./avg_C_ref;
NormIntensityRatio = Norm_T ./ Norm_C;

% Applying the Threshold
for ii=1:W
    for jj=1:H
        if Count_Mix(ii,jj)>Th
            IntensityRatio(ii,jj) = IntensityRatio(ii,jj);
            NormIntensityRatio(ii,jj) = NormIntensityRatio(ii,jj);
        else
            IntensityRatio(ii,jj)=0;
            NormIntensityRatio(ii,jj) =0;
        end
    end
end
% Calculating the Temperature
% T_ref is entered as
Temp_K=T_ref*(0.6816*NormIntensityRatio(ii,jj)+0.32)
```

APPENDIX B

Seeding System Construction

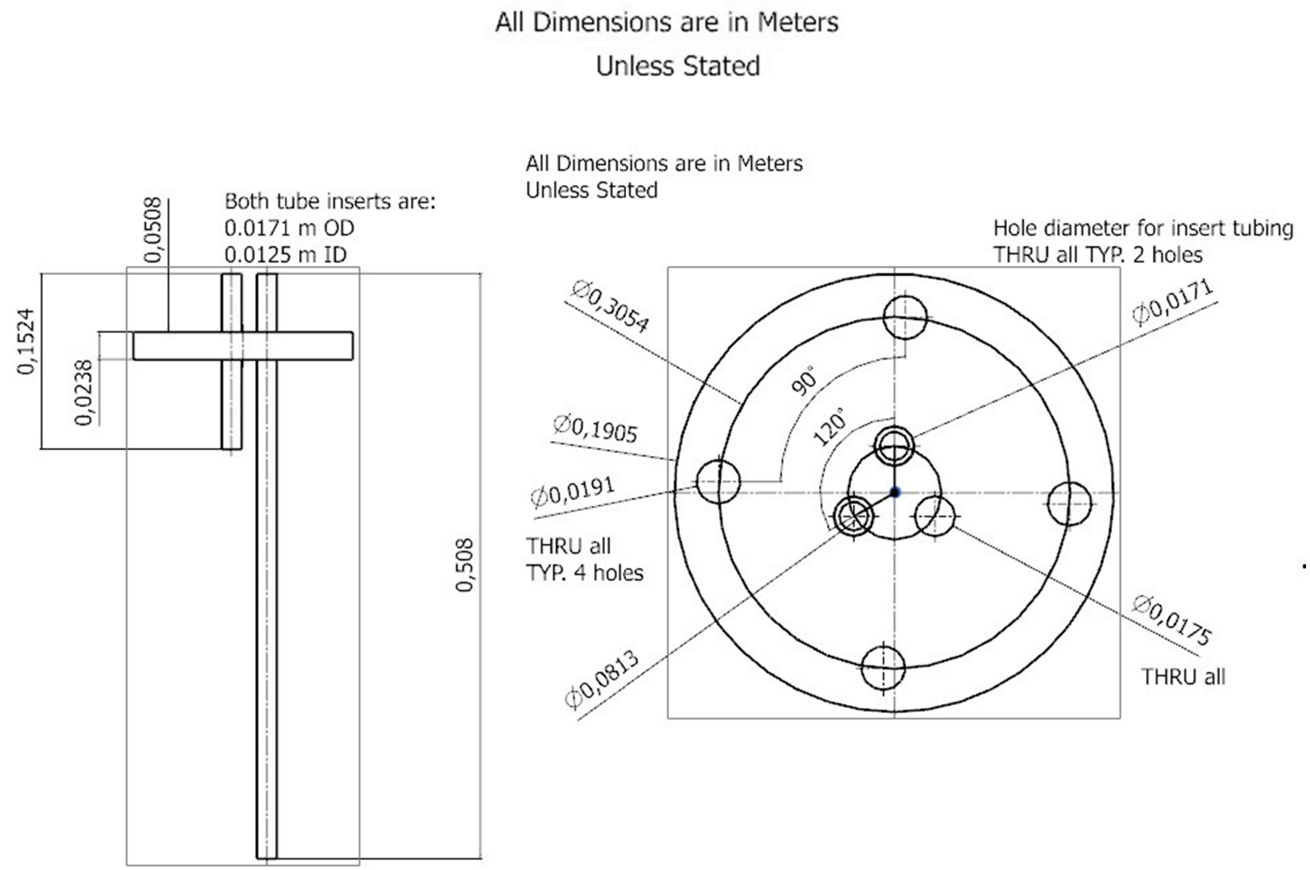

Figure B.1. Bubbling system drawing

APPENDIX C

Jet Impingement Surface Construction

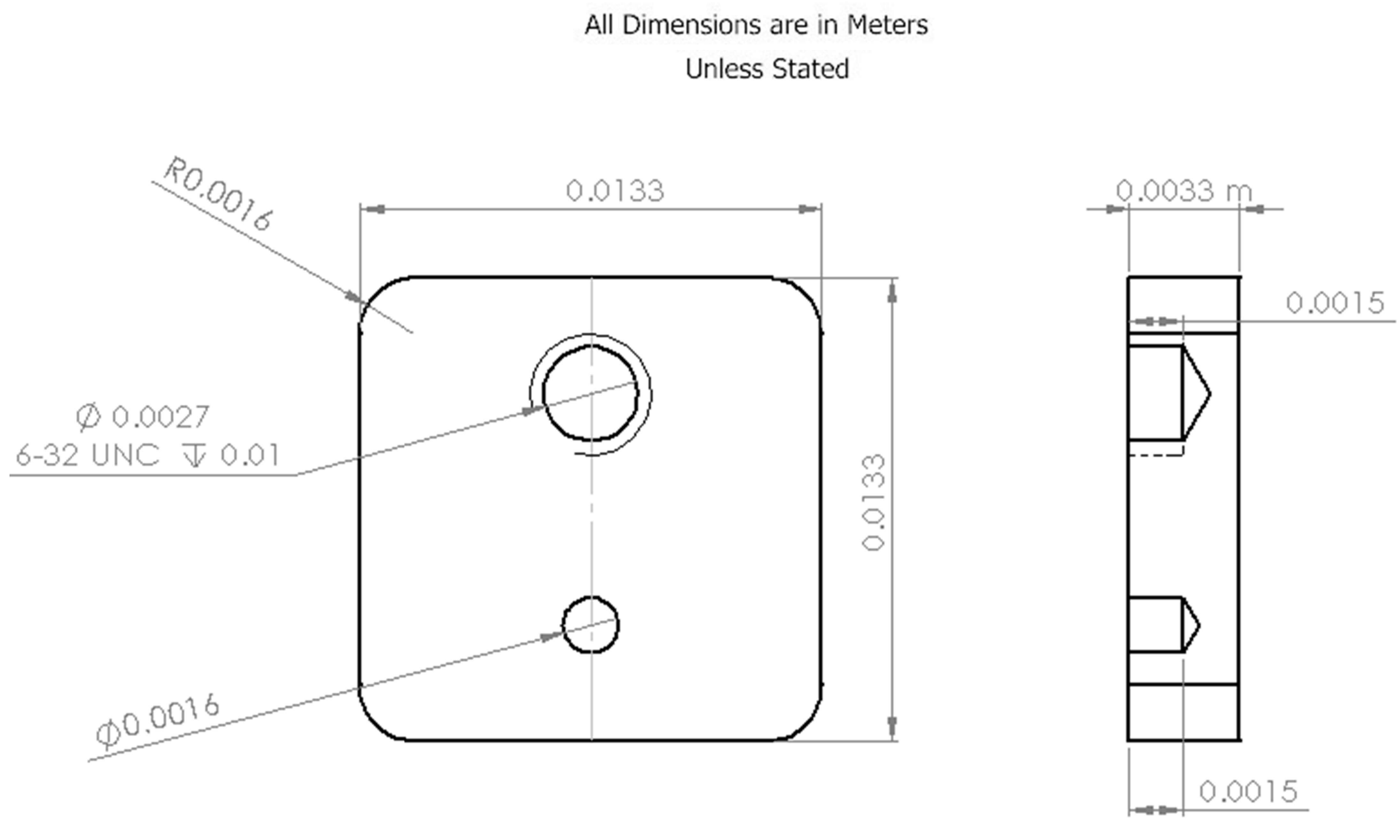

Figure C.1. Aluminum plate drawing

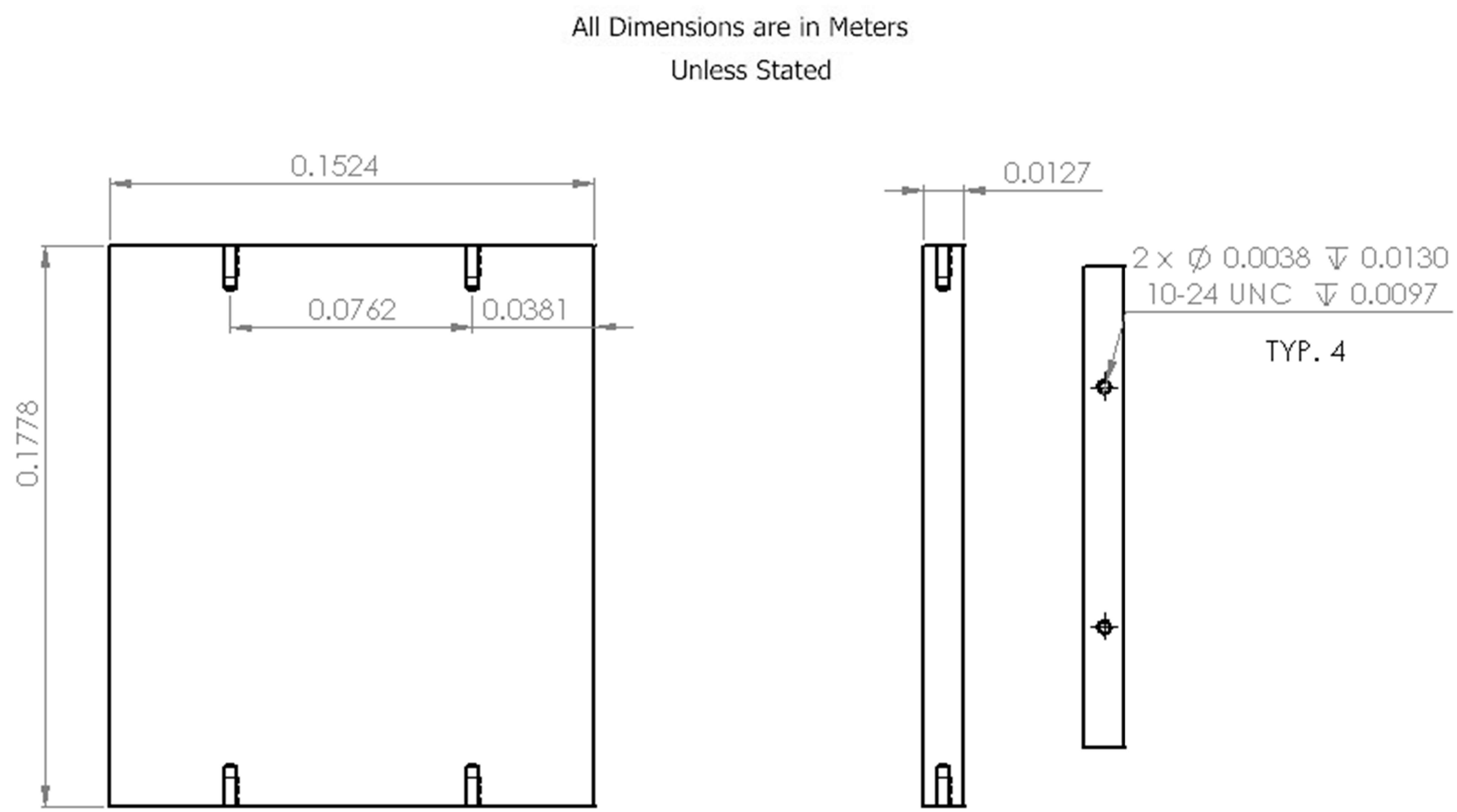

Figure C.2. Jet impingement plenum drawing, front view

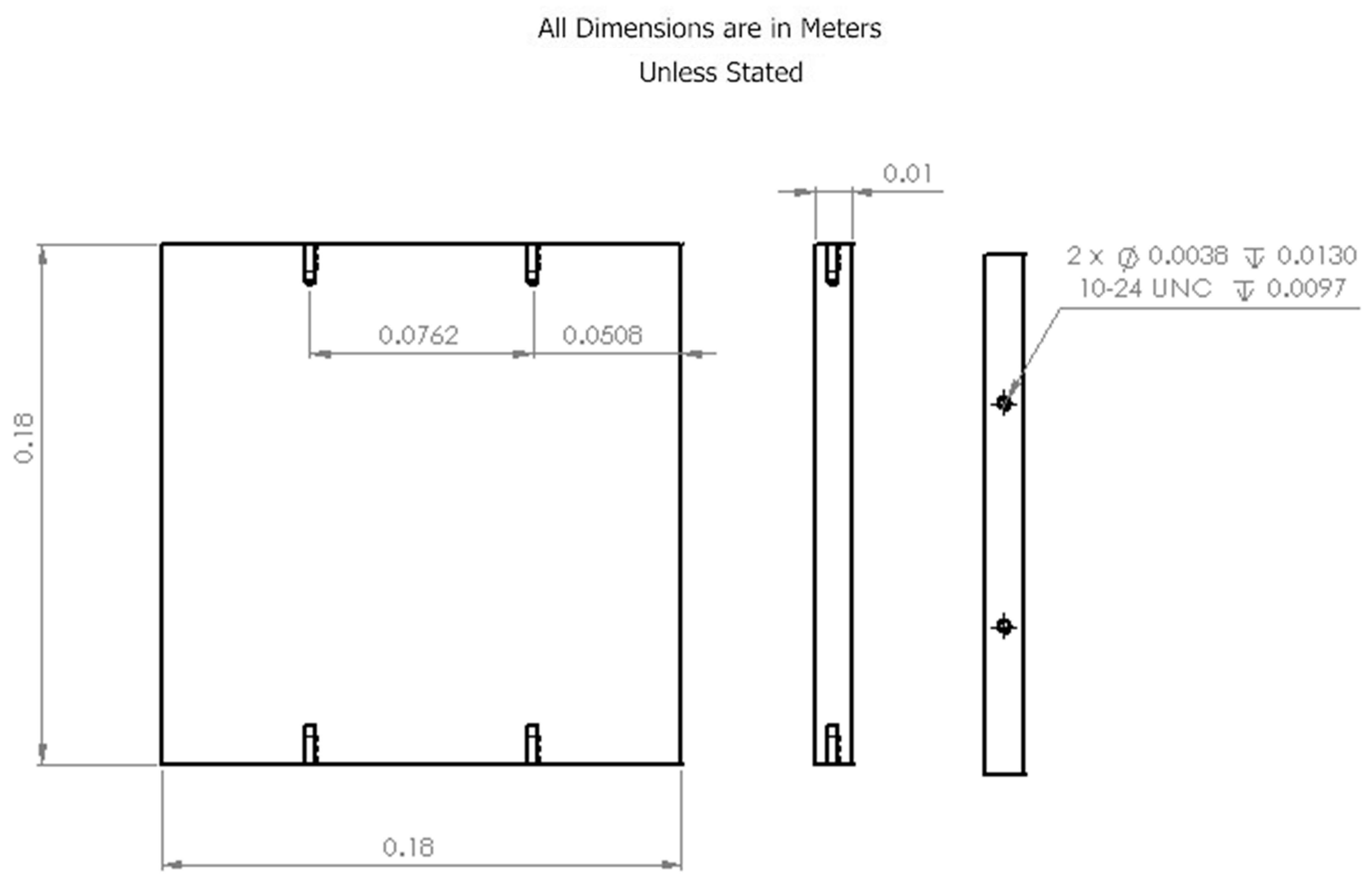

Figure C.3. Jet Impingement plenum drawing, side view

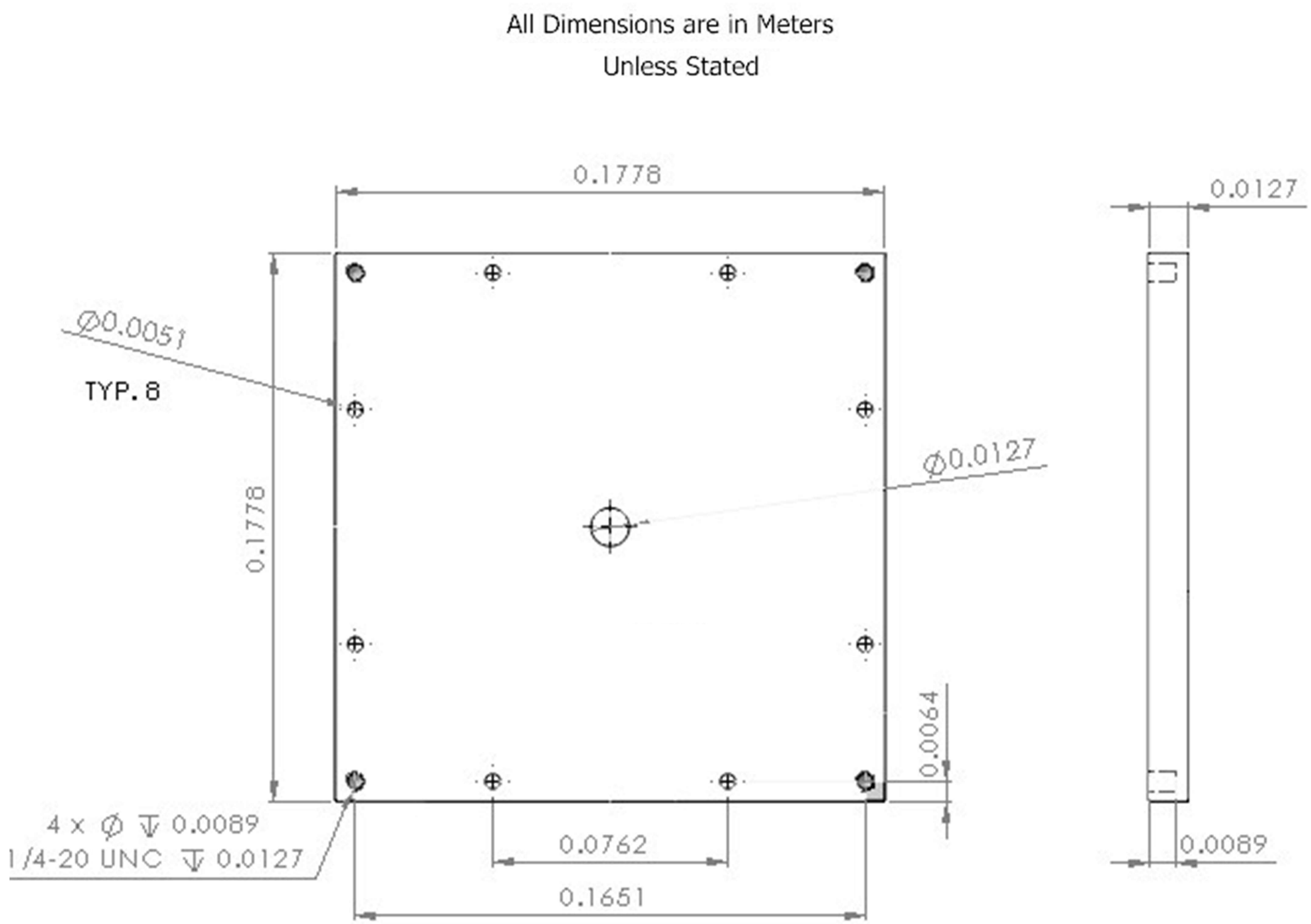

Figure C.4. Jet Impingement plenum drawing, jet plate

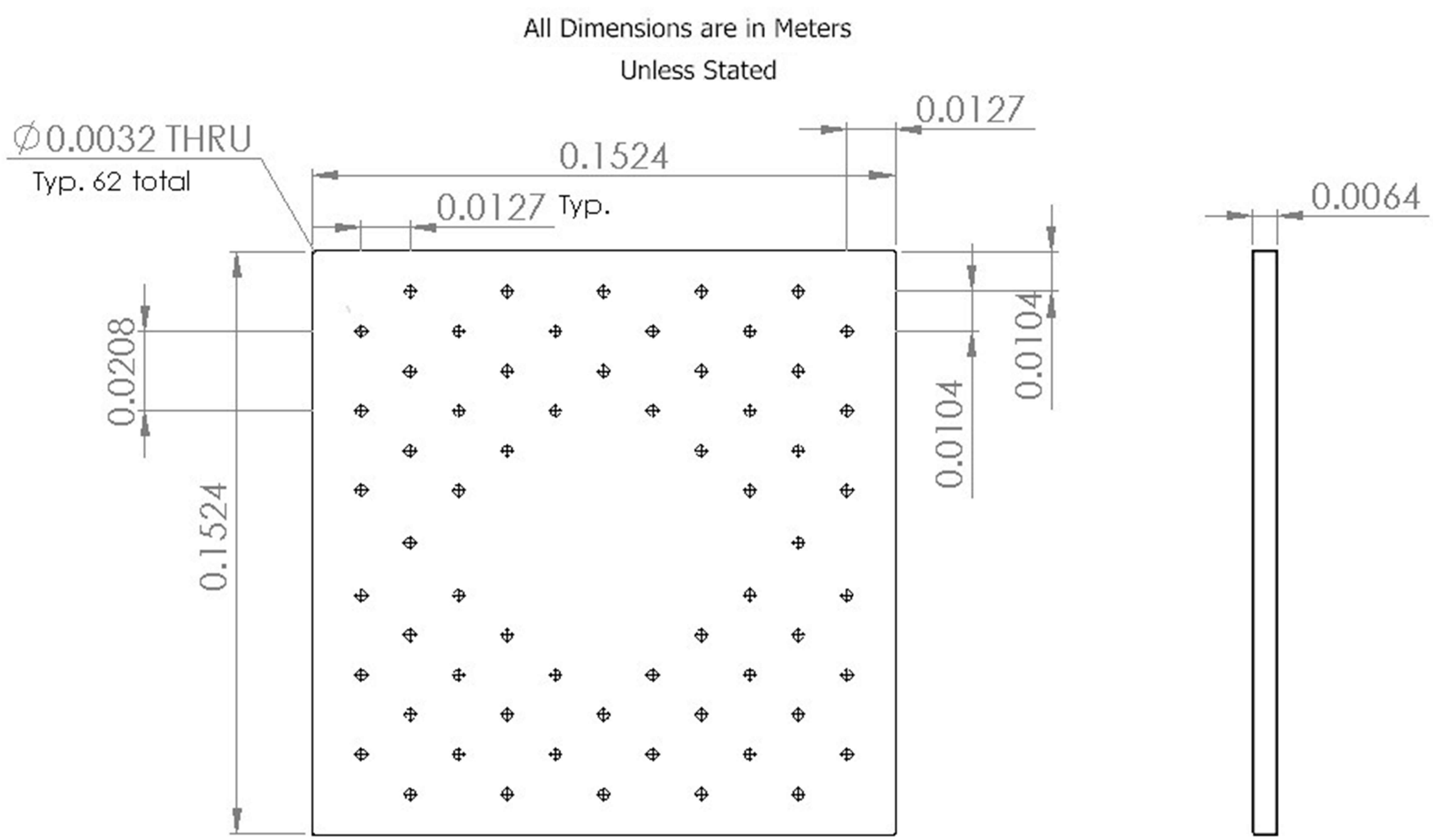

Figure C.5. Jet impingement plenum drawing, middle plate

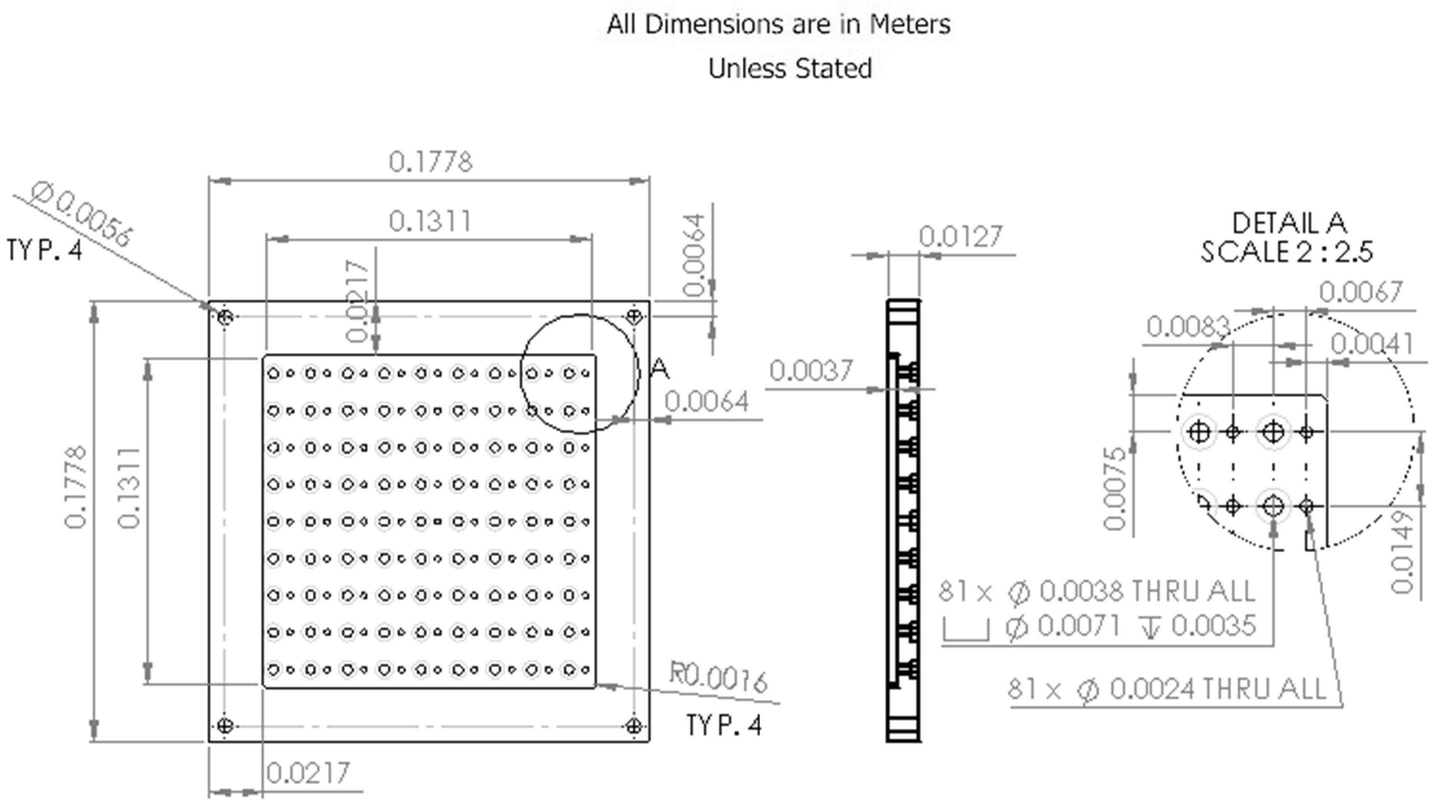

Figure C.6. Jet impingement target plate drawing

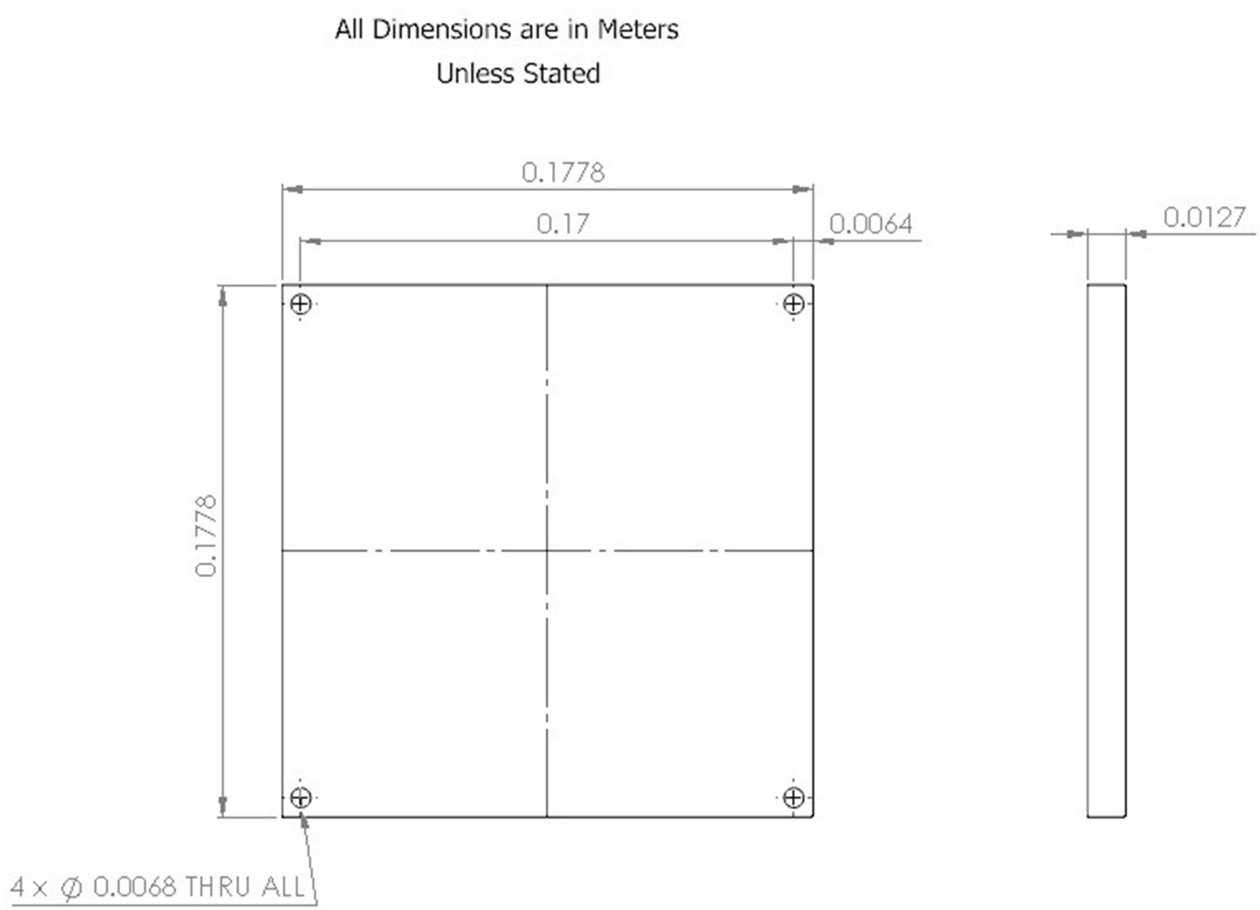

Figure C.7. Jet impingement target plate support drawing

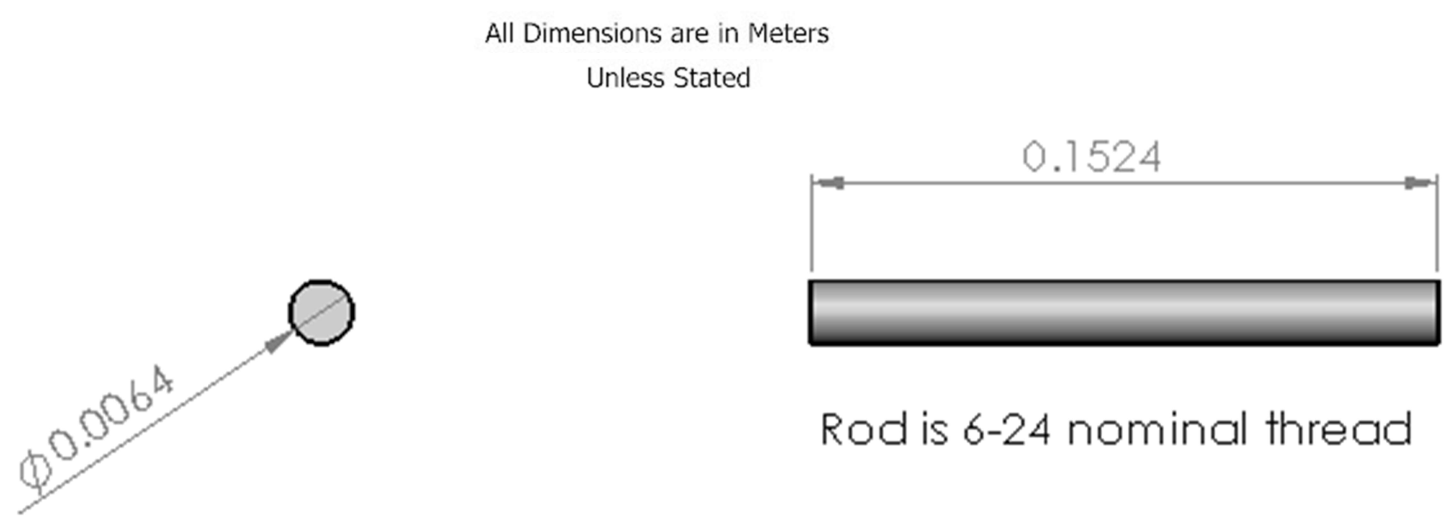

Figure C.8. Threaded rod drawing

APPENDIX D

LabVIEW Code and Graphical Window

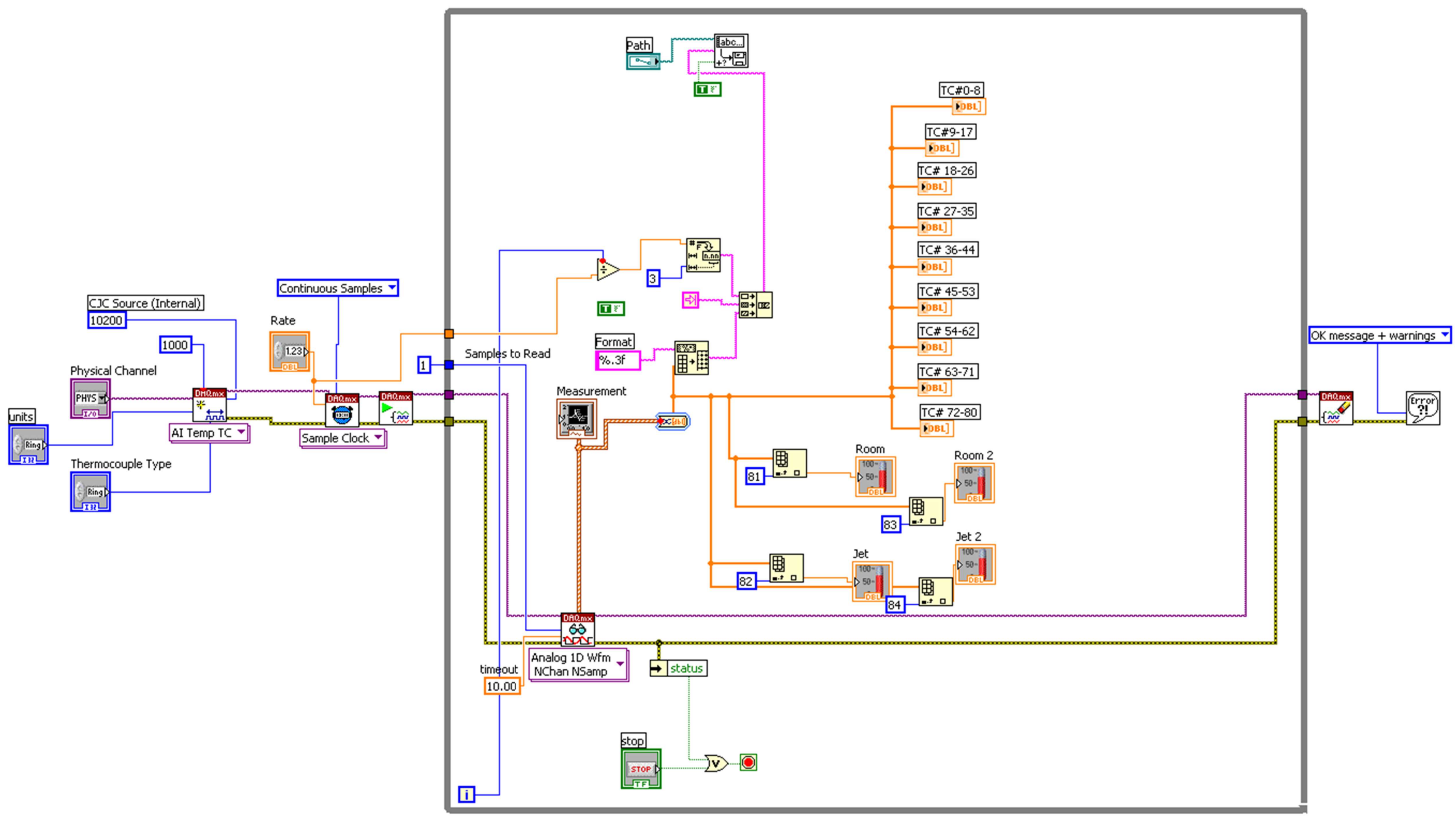

Figure D.2. Jet impingement target plate LabVIEW code

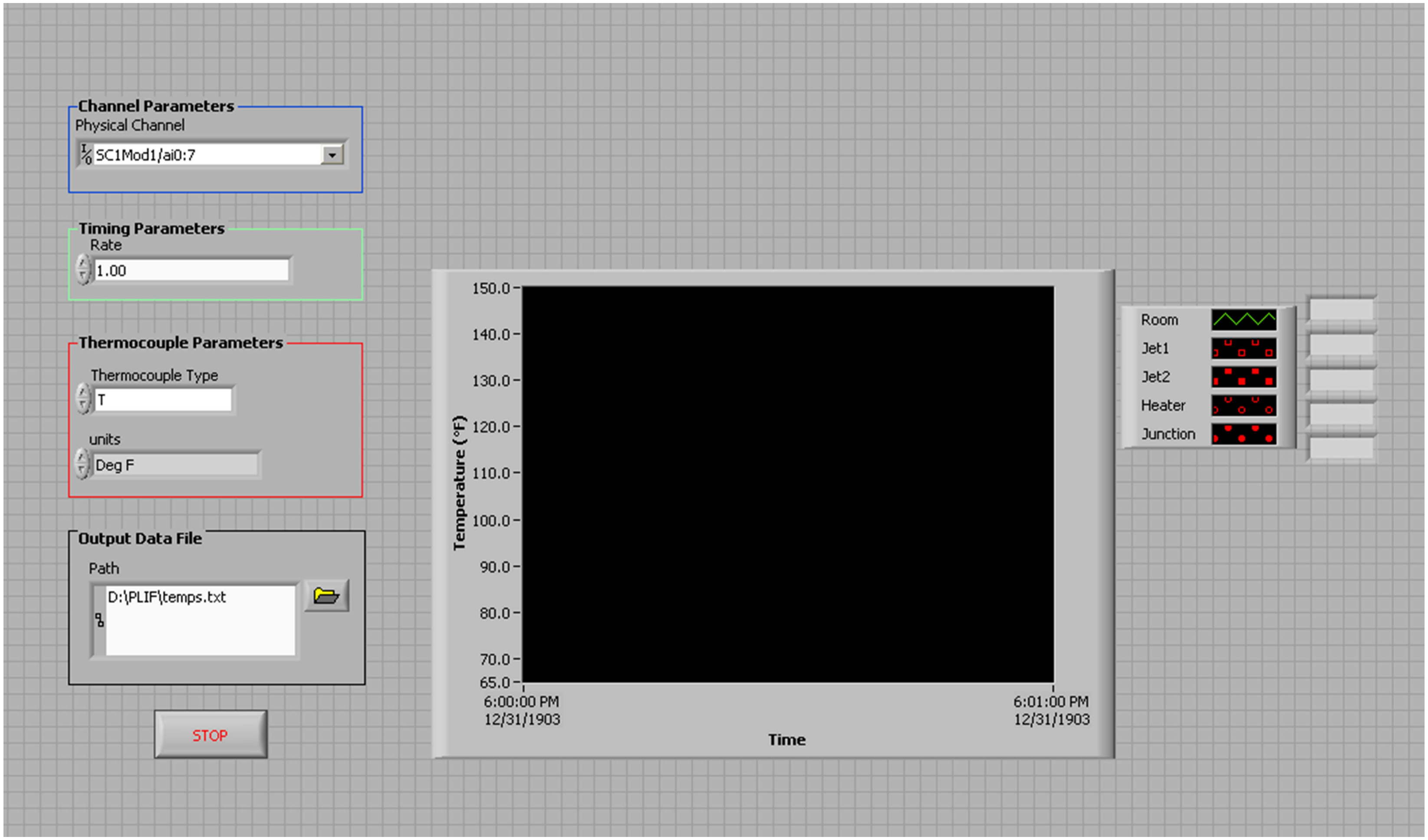

Figure D.3. Free jet LabVIEW graphical window

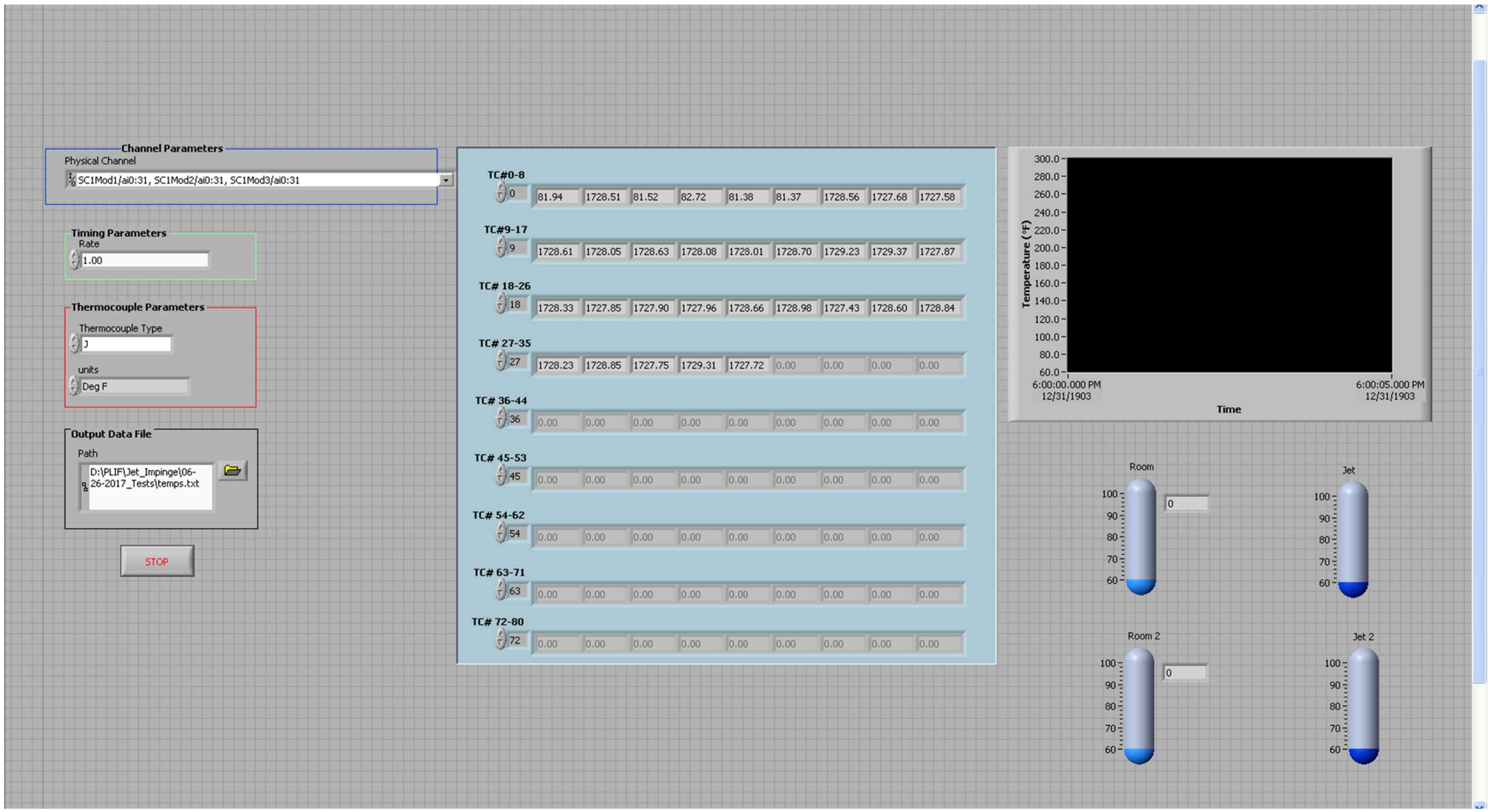

Figure D.4. Jet impingement target plate LabVIEW graphical window

REFERENCES

[1] White, F. and Corfield, I., 2006. *Viscous Fluid Flow*. McGraw-Hill Higher Education, Boston.

[2] Driest, E. V., 1956. "On Turbulent Flow Near a Wall". J. Aeronaut. Sci, 23(11), pp. 1007– 1011.

[3] Wilcox, D., 1998. *Turbulence Modeling for CFD*. DCW Industries La Canada, CA.

[4] Wilson, D. and Korakianitis, T., 2014. *The Design of High-Efficiency Turbomachinery and Gas Turbines*. MIT Press, Boston.

[5] Han, J., Dutta, S. and Ekkad, S., 2012. *Gas Turbine Heat Transfer and Cooling Technology*. CRC Press.

[6] Klaus, H., 1997. *Jet Engines: Fundamentals of Theory, Design and Operation*.

[7] Saravanamuttoo, H., Rogers, G. and Cohen, H., 2001. *Gas Turbine Theory*. Pearson Education.

[8] Mattingly, J., 1996. *Elements of Gas Turbine Propulsion*. McGraw-Hill Science, Engineering and Mathematics.

[9] Bergman, T. and Incropera, F., 2011. *Fundamentals of Heat and Mass Transfer*. John Wiley & Sons.

[10] Zuckerman, N. and Lior, N., 2006. "Jet Impingement Heat Transfer: Physics, Correlation, and Numerical Modeling". *Advances in Heat Transfer,* 39, pp. 565–631.

[11] Han, B. and Goldstein, R., 2001. "Jet-Impingement Heat Transfer in Gas Turbine Systems". *Annals of the New York Academy of Sciences,* 934(1), pp. 147–161.

[12] Schlichting, H., Gersten, K. and Krause, E., 1955. *Boundary-Layer Theory*. Springer.

[13] Clauser, F., 1956. "The Turbulent Boundary Layer". *Advances in Applied Mechanics,* 4, pp. 1–51.

[14] Hah, C., 1986. "A Numerical Modeling of Endwall and Tip-Clearance Flow of an Isolated Compressor Rotor". *Journal of Engineering for Gas Turbines and Power,* 108(1), pp. 15–21.

[15] Knost, D. and Thole, K., 2003. "Computational Predictions of Endwall Film-Cooling for a First Stage Vane". *ASME Turbo Expo 2003, collocated with the 2003 International Joint Power Generation Conference, Anonymous American Society of Mechanical Engineers*, pp. 163–173.

[16] Chen, H. and Patel, V., 1988. "Near-Wall Turbulence Models for Complex Flows Including Separation". *AIAA Journal,* 26(6), pp. 641–648.

[17] Lei, J. and Will, H. A., 1998. "Thin-Film Thermocouples and Strain-Gauge Technologies for Engine Applications". *Sensors and Actuators A: Physical,* 65(3), pp. 187–193.

[18] Cooper, T., Field, R. and Meyer, J., 1975. "Liquid Crystal Thermography and its Application to the Study of Convective Heat Transfer". *Journal of Heat Transfer,* 97(3), pp. 442–450.

[19] Lui, T., 2005. *Pressure-and Temperature-Sensitive Paints*. Wiley Online Library.

[20] Kohse-Hinghaus, K., 1994. "Laser Techniques for the Quantitative Detection of Reactive Intermediates in Combustion Systems". *Progress in Energy and Combustion Science,* 20(3), pp 203–279.

[21] Hanson, R. K., Hanson, J. M. and Paul, P. H., 1990. "Planar Laser-Fluorescence Imaging of Combustion Gases". *Applied Physics B: Lasers and Optics,* 50(6), pp.441–454.

[22] Schulz, C., and Sick, V., 2005. "Tracer-LIF Diagnostic: Quantitative Measurement of Fuel Concentration, Temperature and Fuel/Air Ratio in Practical Combustion Systems". *Progress in Energy and Combustion Science,* 31(1), pp 75–121.

[23] McIlory, A. and Kohse-Hinghaus, K., 2002. *Applied Combustion Diagnostics*.

[24] Long, M. B., Webber, B. F. and Chang, R. K., 1979. "Instantaneous two-dimensional Concentration Measurements in a Jet Flow by Mie Scattering". *Applied Physics Letters,* 34(1), pp. 22–24.

[25] Kychakoff, G., Hanson, R. D. and Hanson, R. K., 1982. "Quantitative Visualization of Combustion Species in a Plane". *Applied Optics,* 21(18), pp. 3225–3227.

[26] Dyer, M. J. and Crosley, D. R., 1982. "Two-Dimensional Imaging of OH Laser-Induced Fluorescence in a Flame". *Optics Letters,* 7(8), pp. 382–384.

[27] Allen, M. and Hanson, R., 1988. "Digital imaging of species concentration fields in spray flames". *Symposium (International) on Combustion, Anonymous Elsevier,* 21, pp. 1755–1762.

[28] McDaniel, J. C., Hiller, B. and Hanson, R. K., 1983. "Simultaneous Multiple-Point Velocity Measurements using Laser-Induced Iodine Fluorescence". *Optics Letters,* 8(1), pp. 51–53.

[29] Seitzman, J. M., Kychakoff, G. and Hanson, R. K., 1985. "Instantaneous Temperature Field Measurements using Planar Laser-Induced Fluorescence". *Optics Letters,* 10(9), pp 439– 441.

[30] Thurber, M. C., 1999. *Acetone Laser-Induced Fluorescence for Temperature and Multiparameter Imaging in Gaseous Flows*.

[31] Thurber, M. and Hanson, R., 2001. "Simultaneous Imaging of Temperature and Mole Fraction using Acetone Planar Laser-Induced Fluorescence". *Experiments in Fluids,* 30(1), pp. 93–101.

[32] Thurber, M. C., Grisch, F. and Hanson, R. K., 1997. "Temperature Imaging with Single-and Dual-Wavelength Acetone Planar Laser-Induced Fluorescence". *Optics Letters,* 22(4), pp 251– 253.

[33] Thurber, M., Kirby, B. and Hanson, R., 1998. "Instantaneous imaging of temperature and mixture fraction with dual-wavelength acetone PLIF". *36th AIAA Aerospace Sciences Meeting and Exhibit,*22(3), p. 397.

[34] Kakuho, A., Nagamine, M. and Amenomori, Y., 2006. "In-Cylinder Temperature Distribution Measurement and its Application to HCCI Combustion". *SAE Technical Paper,* 115(3), pp 548– 569.

[35] Koban, W., Koch, J. D. and Hanson, R. K., 2004. "Absorption and Fluorescence of Toluene Vapor at Elevated Temperatures". *Physical Chemistry Chemical Physics,* 6(11), pp. 2940–2945.

[36] Lozano, A., Yip, B. and Hanson, R., 1992. "Acetone: A Tracer for Concentration Measurements in Gaseous Flows by Planar Laser-Induced Fluorescence". *Experiments in Fluids,* 13(6), pp. 369–376.

[37] Hanson, R. K., 1988. "Combustion diagnostics: planar imaging techniques," Symposium (Inter-national) on Combustion". *Anonymous Elsevier,* 21(6), pp. 1677–1680.

[38] Yoo, J. H., Hanoson, R. and Cappelli, M. A., 2011. *Strategies for planar laser-induced fluorescence thermometry in shock tube flows*. Stanford University.

[39] Koch, J., 2005. *Fuel tracer photophysics for quantitative planar laser-induced fluorescence*. Stanford University California, USA.

[40] Neij, H., Johansson, B. and Aldn, M., 1994. “Development and Demonstration of 2D-LIF for Studies of Mixture Preparation in SI Engines”. *Combustion and Flame,* 99(2), pp. 449–457.

[41] LaVision, D., 2007. *8.1 Software, Product Manual, 1003001*. LaVision.

[42] Thurber, M., and Hanson, R. K., 1999, "Pressure and Composition Dependences of Acetone Laser-Induced Fluorescence with Excitation at 248, 266, and 308 Nm". *Applied Physics B: Lasers and Optics*, 69(3) pp. 229-240.

[43] Wermuth, N. and Sick, V., 2005. “Pressure and Composition Dependences of Acetone Laser-Induced Fluorescence with Excitation at 248, 266, and 308 Nm.”. *Applied Physics B: Lasers and Optics,* 12(6), pp. 729–740.

[44] Burton, C. S. and Jr., W. A. N., 1968. “Electronic Energy Relaxation in Toluene Vapor”. *The Journal of Chemical Physics,* 49(4), pp. 1705–1714.

[45] Lffler, M., Beyrau, F. and Leipertz, A., 2010. “Acetone Laser-Induced Fluorescence Behavior for the Simultaneous Quantification of Temperature and Residual Gas Distribution in Fired Spark-Ignition Engines”. *Applied Optics,* 49(1), pp. 37–49.

[46] Miller, V. A., Gamba, M. and Mungal, M. G., 2013. “Single-and Dual-Band Collection Toluene PLIF Thermometry in Supersonic Flows”. *Experiments in Fluids,* 54(6), p. 1539.

[47] Kearney, S. and Reyes, F., 2003. “Quantitative Temperature Imaging in Gas-Phase Turbulent Thermal Convection by Laser-Induced Fluorescence of Acetone”. *Experiments in Fluids,* 34(1), pp. 87–97.

[48] O’Byrne, S., Danehy, P. and Houwing, A., 2003. “PLIF temperature and velocity distributions in laminar hypersonic flat-plate flow”. *Instrumentation in Aerospace Simulation Facilities,* 20(1), pp. 136–147.

[49] Coleman, H. W., and Steele, W. G., 2009, *Data Analysis, Regression, and Reporting of Results*, Experimentation, Validation, and Uncertainty Analysis for Engineers, Third Edition, pp. 217-250.

[50] Bejan, A., 2013. *Convection heat transfer*. John Wiley & Sons.

[51] List, E., 1982. “Turbulent Jets and Plumes”. *Annual Review of Fluid Mechanics,* 14(1), pp. 189–212.

[52] Fellouah, H., Ball, C. and Pollard, A., 2009. “Reynolds Number Effects within the Development Region of a Turbulent Round Free Jet”. *International Journal of* pp. 3943–3954.

[53] Popiel, C. O. and Trass, O., 1991. "Visualization of a Free and Impinging Round Jet". *Experimental Thermal and Fluid Science,* 4(3), pp. 253–264.

[54] Kwon, S. J. and Seo, I. W., 2005. "Reynolds Number Effects on the Behavior of a Non-Buoyant Round Jet". *Experiments in Fluids,* 38(6), pp. 801–812.

[55] Dimotakis, P. E., Miake-Lye, R. C. and Papantoniou, D. A., 1983. "Structure and Dynamics of Round Turbulent Jets". *The Physics of Fluids,* 26(11), pp. 3185–3192.

[56] Brown, G. L. and Roshko, A., 1974. "On Density Effects and Large Structure in Turbulent Mixing Layers". *Journal of Fluid Mechanics,* 64(4), pp. 775–816.

[57] Qinn, W. and Militzer, J., 1988. "Experimental and Numerical Study of a Turbulent Free Square Jet". *The Physics of Fluids,* 31(5), pp. 1017–1025.

[58] Bogdanoff, D., 1983. "Compressibility Effects in Turbulent Shear Layers". *AIAA Journal,* 21(6), pp. 926–927.

[59] Reichardt, H., 1944. "Impulsund Wrmeaustausch in Freier Turbulenz". *ZAMM-Journal of Applied Mathematics and Mechanics/Zeitschrift Fr Angewandte Mathematik Und Mechanik,* 24(6), pp. 268–272.

[60] Yunus, A. C. and Cimbala, J. M., 2006. *Fluid Mechanics Fundamentals and Applications International Edition*. McGraw Hill Publication.

[61] San, J. and Lai, M., 2001. "Optimum Jet-to-Jet Spacing of Heat Transfer for Staggered Arrays of Impinging Air Jets". *International Journal of Heat and Mass Transfer,* 44(21), pp. 3997–4007.

[62] Ashforth-Frost, S. and Jambunathan, K., 1996. "Effect of Nozzle Geometry and Semi-Confinement on the Potential Core of a Turbulent Axisymmetric Free Jet". *International Communications inHeat and Mass Transfer,* 23(2), pp. 155–162.

[63] Martin, H., 1977. "Advances in Heat Transfer". *Elsevier,* 15(7), pp. 1–60.

[64] Jumbunathan, K., Lai, E. and Moss, M., 1992. "A Review of Heat Transfer Data for Single Circular Jet Impingement". *International Journal of Heat and Fluid Flow,* 13(2), pp. 106–115.

[65] Polat, S., Huang, B. and Mujumdar, A. S., 1989. "Numerical Flow and Heat Transfer Under Impinging Jets: A Review". *Annual Review of Heat Transfer,* 2(2), pp. 92–110.

[66] Goldstein, R., Behbahani, A. and Heppelmann, K. K., 1986. "Streamwise Distribution of the Recovery Factor and the Local Heat Transfer Coefficient to an Impinging Circular Air Jet". *International Journal of Heat and Mass Transfer,* 29(8), pp. 1227–1235.

[67] Lee, S., Lee, J. and Lee, D., 1993. "Heat Transfer from a Plate to a Fully Developed Axisymmetric Impinging Jet". *ASME-PUBLICATIONS-HTD,* 11(11), p. 263.

[68] Alden, M., 1999. "Laser Spectroscopic Techniques for Combustion Diagnostics". *Combustion Science and Technology,* 149(6), pp. 1–18.

[69] Donaldson, C. D., Snedeker, R. S. and Margolis, D. P., 1971. "A Study of Free Jet Impingement. Part 2. Free Jet Turbulent Structure and Impingement Heat Transfer". *Journal of Fluid Mechanics,* 45(3), pp. 477–512.

[70] Goldstein, R. and Behbahani, A., 1982. "Impingement of a Circular Jet with and without Cross Flow". *International Journal of Heat and Mass Transfer,* 25(9), pp. 1377–1382.

[71] Mohanty, A. and Tawfek, A., 1993. "Heat Transfer due to a Round Jet Impinging Normal to a Flat Surface". *International Journal of Heat and Mass Transfer,* 36(6), pp. 1639–1647.

[72] Baughn, J. and Shimizu, S., 1989. "Heat Transfer Measurements from a Surface with Uniform Heat Flux and an Impinging Jet". *Journal of Heat Transfer (Transactions of the ASME (American Society of Mechanical Engineers), Series C);(United States),* 111(4), pp. 139–147.

[73] Huang, L. and El-Genk, M. S., 1994. "Heat Transfer of an Impinging Jet on a Flat Surface". *International Journal of Heat and Mass Transfer,* 37(13), pp. 1915–1923.

[74] Hoogendoorn, C., 1977. "The Effect of Turbulence on Heat Transfer at a Stagnation Point". *National Journal of Heat and Mass Transfer,* 20(12), pp. 1333–1338.

[75] Lytle, D. and Webb, B., 1994. "Air Jet Impingement Heat Transfer at Low Nozzle-Plate Spacings". *International Journal of Heat and Mass Transfer,* 37(12), pp. 1687–1697.

[76] Goldstein, R. and Timmers, J., 1982. "Visualization of Heat Transfer from Arrays of Impinging Jets". *International Journal of Heat and Mass Transfer,* 25(12), pp. 1857–1868.

[77] Goldstein, R., Chyu, M. and Hain, R., 1985. "Measurement of Local Mass Transfer on a Surface in the Region of the Base of a Protruding Cylinder with a Computer-Controlled Data Acquisition System". *International Journal of Heat and Mass Transfer,* 28(5), pp. 977–985.

[78] Lau, S., Han, L. and Kim, Y., 1994. "Turbulent Heat Transfer and Friction in Pin Fin Channels with Lateral Flow Ejection". *Journal of Heat Transfer,* 111(1), pp. 51–58.

[79] Lakowicz, J. R., 1999. *Principles of Fluorescence Spectroscopy*. Springer, pp. 25-61.